Septins, Cytokinesis, and Multicellular Development in the Closest Living Relatives of Animals

By

Michael David Carver

A dissertation submitted in partial satisfaction of the

requirements for the degree of

Doctor of Philosophy

in

Molecular and Cell Biology

in the

Graduate Division

of the

University of California, Berkeley

Committee in charge:

Professor Nicole King, Chair
Professor David Bilder
Professor Rebecca Heald
Professor Iswar Hariharan

Spring 2026

Abstract

Septins, Cytokinesis, and Multicellular Development in the Closest Living Relatives of Animals

by

Michael David Carver

Doctor of Philosophy in Molecular and Cell Biology

University of California, Berkeley

Professor Nicole King, Chair

Animal multicellularity requires cells to divide while remaining physically and developmentally integrated with their neighbors. Although this relationship is central to modern animal biology, how cell division contributed to the establishment of animal multicellularity is difficult to reconstruct because this transition occurred over 650 million years ago. This dissertation investigates the intersection of cell division and multicellularity in choanoflagellates, the closest living relatives of animals, and identifies septins as regulators of cell division and multicellular organization in the choanoflagellate *Salpingoeca rosetta*.

Chapter 1 reviews the relationship between cell division and multicellular organization. I first discuss how cell division shapes animal tissues and how tissue environments constrain cytokinesis. I then consider how changes to cytokinesis and extracellular matrix regulation may have contributed to the emergence of clonal multicellularity. Finally, I introduce choanoflagellates, and *S. rosetta* in particular, as useful models for studying cell division and multicellular development in the context of animal origins.

In Chapter 2, I investigate septin function in *S. rosetta*. Septins are cytoskeletal proteins that regulate cytokinesis in fungi and animals, but their functions in choanoflagellates were previously unknown. Using CRISPR/Cas9-mediated gene disruption, I found that multiple *S. rosetta* septins regulate cell size and rosette colony development. Further analysis of one septin, *Sros_septA,* shows that septin disruption causes late-stage cytokinesis failure and produces large multinucleated cells, phenotypes that become more pronounced following rosette induction. Endogenously tagged *Sros*_SeptA dynamically redistributes from the basal pole in interphase cells to the cleavage furrow and nascent intercellular bridge during division. Together, these findings suggest that septins regulate cytokinesis in *S. rosetta* and that the multicellular context influences septin function. Septins may therefore represent one mechanism that helped cytokinesis meet the physical and developmental demands of emerging multicellular organization during animal evolution.

In Appendix 1, I present additional data on the localization of septins and actin in *S. rosetta* and discuss future directions for studying septin function at the interface of cell division and multicellularity in this model. In Appendix 2, I present preliminary work exploring the cellular and genetic basis of the phenotype in Solo, a mutant of *S. rosetta* defective in both chain and rosette colony development. Finally, in Appendix 3, I discuss preliminary work aimed at understanding the function of cadherins in choanoflagellates, genes whose adhesion and signaling functions in animals are critical for multicellular development.

Table of Contents

Acknowledgements

First and foremost, thank you to my advisor Nicole, who has helped guide me as a scientist and as a professional through all these years. When I look back on my earliest work and compare it to where I am now, it is night and day. Nicole taught me to have the highest standards in producing and communicating science. This, along with her patience and commitment to my training, helped me develop tremendously as a scientist and a person. Thank you, Nicole, for helping to steer me through sometimes turbulent waters. I would also like to thank the rest of my thesis committee: Rebecca Heald, Iswar Hariharan, and David Bilder, for their advice and guidance throughout my graduate career. To David in particular, who chaired my qualification committee, taught cell biology alongside me, and always offered support and sound advice when I needed it, thank you.

So much of how you grow during graduate school comes from your lab mates and the friends you make along the way. Alain Garcia de Las Bayonas, you have been my most constant partner in the lab since I first rotated, and I wouldn't be the scientist I am now without you. From you, I learned how to approach the biological world with wonder. Maxwell Coyle, you are a dependable friend and mentor, and your spirit made the King lab bright. From you, I learned to conduct science creatively and critically, and to approach life with an open heart and steady mind. Ryan Hulett, you arrived during my final year, when our lab had become small, and you quickly became a friend and anchor. You have shown me how to be unwavering in my support and kindness toward those around me. Thanks also to the many more people who made the King lab a home: Stefany Gonzales, Becca Arruda, Chrisa Staikou, Josean Reyes-Rivera, Jacob Steenwyk, Flora Rutaganira, and many more. I have also benefited from the work and advice of former King lab members Laura Wetzel, David Booth, and Ben Larson, without whom my Chapter 2 project would not have been possible. And to my friends, Kevin Rose, Meaghan Marohn, and Shayan Hosseinzadeh, thank you. Ours was truly the COVID cohort, and the bonds that we formed and retained throughout graduate school are something I will always cherish.

I am also deeply grateful for my time in the MBL Physiology course. Thanks first to Nicole for encouraging me to attend, and to my amazing course instructors Amy Gladfelter and Cliff Brangwynne. Thanks also to Audrey Williams, my mentor and part-time physiology swim buddy, for her mentorship at MBL and later during my post-course research in Amy's lab. To my two best friends in the Physiology course, Urša Uršič and Adam Lamson, thank you for making MBL such a joyful experience. Urša, you are truly one of a kind. You are such a good friend, and our time in San Diego at ASCB and with Adam roaming around Slovenia was unforgettable. Adam, you are genuine, dependable, and spectacular. You also hold the wonderful record of being the person with whom I have only ever shared once-in-a-lifetime experiences, from MBL to Slovenia to our time with our friends in the desert last summer. Thank you both.

So much of graduate school is what you do outside of your science to keep yourself grounded. In that spirit, I am grateful for the eastern Sierra Nevada mountains, where I feel truly at home and at ease, and to the outdoor Spieker Pool and the bike roads in the Berkeley hills for allowing me to unwind from the long lab days. Writing a dissertation is a long and laborious process. I kept myself grounded with four unexpected friends I met along the way, the bald eagles Jackie and Shadow and their eaglets Sandy and Luna from Big Bear, whose twenty-four-hour camera feed

accompanied the majority of my writing sessions as a reminder that the world is large, and that I am not at the center of it.

Lastly, I am blessed with an incredibly loving family that has supported me throughout my life, including graduate school. To my grandma Carver and my grandma Pepper, whom I love very much, you were always the first to ask about my goals in graduate school and to support them. Though you are no longer with us, I will carry you with me at graduation and beyond, and I hope I have made you proud. To my aunt Risa, who has persevered through so much in the last few years and still always made time for me when I needed to talk, thank you for everything. You have taught me to be tough, to keep my head up, and to keep going no matter what. To my amazing mom and dad: I could not ask for more supportive parents. Both of you have helped me during hard times, each in your own irreplaceable way. Also, to my brothers Jared and Bryce, my sister Liana, my grandpa Carver, my aunt Dorothy, my stepmom Andrea, my best friend Jacob, and to the rest of my family, I thank you all so much for your support and understanding as I've journeyed through this crazy chapter in my life. I love you all. A final thanks to my youngest brother Bryce, who suggested a dolphin, his favorite animal, for the animal lineage in the Figure 1.1 phylogeny. The choice of animal representative is arbitrary and yet always feels strangely significant, and I'm glad to have a bit of Bryce represented in this part of my first dissertation figure.

Chapter 1

Cell division and the emergence of multicellular organization

Introduction

Cell division and clonal multicellular organization are closely linked processes. In animal tissues, cell division drives development and is likewise shaped by spatial, adhesive, and mechanical constraints. Understanding the relationship between cell division and multicellularity requires considering not only the molecular mechanisms involved, but also the contexts in which those mechanisms operate. How the regulation of cell division became integrated with clonal multicellular development is difficult to study, as many of these transitions occurred deep in evolutionary time (Knoll, 2011; Brunet and King, 2017). Instead, these steps can be studied using experimentally tractable systems in which unicellular and multicellular contexts can be directly compared. Work in these systems has indicated roles for both cell division and extracellular matrix (ECM) regulation in the origins of clonal multicellularity (Levin *et al.*, 2014; Hanschen *et al.*, 2016; Bozdag *et al.*, 2023). In the context of animal origins, choanoflagellates provide a useful model as the closest living relatives of animals (Figure 1.1; Booth and King, 2022). The choanoflagellate *Salpingoeca rosetta* is particularly well suited for studying these questions: it can switch between unicellular and multicellular forms (chains and rosettes), and its rosettes are physically organized through both intercellular bridges and ECM (Dayel *et al.*, 2011), features that allow comparison of cell division across cellular contexts.

In this chapter, I examine how cell division contributes to multicellular organization and how multicellular environments constrain and reshape division. I then consider how this relationship may have emerged during the evolution of clonal multicellularity and discuss why choanoflagellates provide a useful system for studying this interface in the context of animal evolution. Throughout, I highlight septins as candidate regulators of this interface: proteins that act during cytokinesis and may help cells divide and develop within multicellular contexts.

Part 1. Cell division in animal multicellular organization

1.1 Eukaryotic cell division: conservation and divergence

Cell division fundamentally shapes biological form. Following foundational observations by Hooke and van Leeuwenhoek in the seventeenth century, cells were identified as the fundamental units of life (Hooke, 1665; Van Leeuwenhoek, 1695). However, cell division remained poorly understood until the late nineteenth century, when researchers studying both plant and animal cells described mitosis, the process of nuclear division, and cytokinesis, the process of cellular division, as discrete processes (Paweletz, 2001; Baluška *et al.*, 2012). This work also suggested that basic principles of cell division, including the establishment of a division plane and partitioning of the cytoplasm, existed across biological diversity. Together, these advances established that cells arise from pre-existing cells and laid the conceptual groundwork for understanding how cell division underlies multicellular organization, an idea later articulated more explicitly by E. B. Wilson (Wilson, 1925).

Modern studies have since shown that eukaryotic cell division is governed by both conserved and lineage-specific molecular mechanisms. Core aspects of cell-cycle progression and mitosis, including cyclin- and cyclin-dependent kinase (CDK)-based regulation (Hartwell *et al.*, 1974; Evans *et al.*, 1983; Murray and Kirschner, 1989; Nurse, 1990), and microtubule-based

chromosome segregation (Walczak *et al.*, 2010), are broadly conserved across eukaryotes (Harashima *et al.*, 2013). In contrast, the execution of cytokinesis varies across lineages (Guertin *et al.*, 2002; Onishi *et al.*, 2020; Ozugergin and Piekny, 2022). For example, land plants complete cytokinesis by building a cell plate through targeted vesicle trafficking and fusion, whereas animals and most fungi undergo cytokinesis through cleavage furrow ingression (Guertin *et al.*, 2002; Green *et al.*, 2012).

In animal cells, cytokinesis proceeds through a coordinated sequence of division-plane specification, contractile ring assembly, cleavage furrow ingression, and membrane abscission (Figure 1.2A; Guertin *et al.*, 2002; Green *et al.*, 2012; Hümpfer *et al.*, 2025). Division-plane positioning is set by the mitotic spindle, which defines an equatorial zone where the centralspindlin complex promotes localized activation of the small GTPase RhoA (White and Glotzer, 2012). Active RhoA, in turn, drives assembly of the actomyosin contractile ring by stimulating formin-mediated actin polymerization and myosin II activation, while also restricting contractility to the cell equator (Green *et al.*, 2012; Carim *et al.*, 2020). The scaffolding protein anillin links these signals by interacting with actin, myosin II, and RhoA to create a mechanically cohesive structure (Piekny and Glotzer, 2008). Septins, which also bind to anillin, contribute to the spatial organization and mechanical stability of the cleavage furrow by forming filamentous structures that interface with the plasma membrane and actomyosin network (Figure 1.2A). As ingression proceeds, the contractile ring transitions into a narrow intercellular bridge containing a dense midbody. Final separation is achieved through membrane abscission. In this process, upstream ESCRT factors help recruit the abscission machinery to the midbody, after which ESCRT-III polymers assemble at sites flanking the midbody and drive membrane constriction, while the AAA ATPase Vps4 remodels these assemblies as abscission proceeds (Figure 1.2A; Mierzwa and Gerlich, 2014).

Throughout the history of eukaryotic cell division research, much of our understanding has been derived from a limited set of model systems, including *S. cerevisiae*, *Xenopus* egg extracts, and cultured animal cell lines. While these models have been instrumental in elucidating the mechanisms of cell division, many represent simplified or derived contexts that lack the spatial or mechanical cues of native multicellular environments (Ragkousi and Gibson, 2014). Important insights into cell division during development have also come from *in vivo* models such as *Drosophila* and *C. elegans*, although these systems represent specific developmental contexts and do not capture the full range of multicellular environments in which cell division occurs (Betschinger and Knoblich, 2004). Other well-characterized cell division models, such as *Chlamydomonas reinhardtii* (Onishi *et al.*, 2020), are more distantly related to animals and therefore less directly informative for animal cell biology (Figure 1.1). Therefore, although much of the genetic and mechanical regulation of cytokinesis is now well characterized, how these mechanisms operate in a diversity of complex multicellular environments remains comparatively less explored. In particular, how division is coordinated with cell adhesion and tissue organization is an active area of research that I will discuss in sections 1.3 and 1.4 (Osswald and Morais-de-Sá, 2019). Notably, both spindle architecture and cytokinesis mechanics have been found to vary by cell type and tissue context. For example, spindle positioning is dynamic throughout embryonic divisions (Knoblich, 2008), and junctional connections within tissues create diverse challenges for cell division within epithelial tissues (Higashi *et al.*, 2016). This suggests that cell division has dynamically adapted during the elaboration of multicellular form.

In the next section, I take a moment to introduce and describe the functions of septins as regulators of cell division and multicellular development. I then examine how cell division contributes to, and is constrained by, multicellular organization in animal tissues in sections 1.3 and 1.4, respectively.

1.2 Introduction to septins

Septins are a conserved family of GTP-binding cytoskeletal proteins best known for regulating cytokinesis in fungi and animals (Mostowy and Cossart, 2012). They will be discussed throughout this chapter and dissertation because their functions in cytokinesis, cortical organization, and multicellular development make them strong candidates for understanding how cell division is coordinated with multicellular organization. Septins are conserved across eukaryotic diversity, with the exception of land plants, Amoebozoa, and Excavata (Figure 1.1; Delic *et al.*, 2024). Functional characterization of septins has largely been restricted to animals and fungi, but several studies outside of these two lineages exist and find that septins localize to the division plane in the green algae *Nannochloris bacillaris* (Yamazaki *et al.*, 2013) and to the mitochondrial fission site in the ciliate *Tetrahymena thermophila* (Włoga *et al.*, 2008). Furthermore, a recent study found that the single septin in *Chlamydomonas reinhardtii* coordinates protein import and division in the chloroplast (Delic *et al.*, 2026). Additional studies outside of fungi and animals promise to add to our understanding of ancestral septin functions in eukaryotes.

In fungi and animals, septins assemble into hetero-oligomers that further polymerize into filaments and higher-order structures that bind sites of membrane curvature, acting to scaffold factors during dynamic membrane processes (Mostowy and Cossart, 2012; Bridges and Gladfelter, 2015; Szuba *et al.*, 2021). During cytokinesis, septins are recruited to the cleavage furrow in coordination with anillin and the actomyosin ring, where they help organize the cortex and stabilize the ingressed furrow (Figure 1.2A; Carim *et al.*, 2020). At later stages, septins persist at the intercellular bridge and midbody, where they contribute to bridge architecture and regulate the timing and positioning of abscission (Mierzwa and Gerlich, 2014). Outside of their direct roles during cytokinesis, septins also function in cell polarity, cell motility, and cilia biogenesis, suggesting a broad repertoire of roles during animal organization and development (Spiliotis *et al.*, 2008; Mostowy and Cossart, 2012; Palander *et al.*, 2017; Gabbert *et al.*, 2023).

In yeast, septins are required for cell division. They mark the division site and coordinate cell separation, and their loss causes severe cytokinetic and morphological defects (Hartwell *et al.*, 1974; Bridges and Gladfelter, 2015). The requirement for septins in animal cytokinesis, in contrast, appears to be context-dependent, and determining their roles is often complicated by redundancy among septin paralogs, which are particularly numerous in vertebrates due to repeated gene duplication (Kinoshita, 2003). However, SEPT7—the sole member of its subgroup and a core component of septin hetero-oligomers—is not redundant in most animal systems, and its loss in flies and mice results in developmental lethality, consistent with a requirement for septin function at the organismal level (Neufeld and Rubin, 1994; Menon *et al.*, 2014). Furthermore, loss of SEPT7 in mammals provides an example of cell-type-specific roles of septins, in which their function is necessary for cytokinesis in fibroblasts but dispensable in hematopoietic cells (Menon *et al.*, 2014). In contrast, *C. elegans* adults can develop even when

both septins are lost, although with morphological defects (Nguyen *et al.*, 2000). Together, these observations suggest that while septins are not essential for cytokinesis in all animal cells, they play context-dependent roles during tissue organization and development. This variable requirement may have made septins a flexible point of evolutionary change in animal cell division.

1.3 Cell division shapes animal tissues

Asymmetric cell division plays a fundamental role in shaping tissues by producing daughter cells with different sizes and developmental fates (Knoblich, 2008). In many early embryos and stem cell lineages, polarity cues are established prior to division and direct both asymmetric spindle positioning and the unequal partitioning of cell fate determinants (Bolkent, 2024). For example, in the *C. elegans* zygote, Par proteins generate an anterior-posterior cortical force imbalance that shifts the spindle toward one side of the cell, producing daughter cells that differ in size (Grill *et al.*, 2001). At the same time, other polarity factors control the unequal inheritance of cell fate determinants during asymmetric division, thereby helping specify daughter cell fate in the embryo (Rose and Gönczy, 2014). Stem cell lineages in mammalian systems and other models often use similar division mechanisms to balance self-renewal and differentiation, with cell polarity and spindle orientation helping control the segregation of cell fate determinants (Knoblich, 2008; Bolkent, 2024). Thus, control of cell division symmetry through polarity and cytoskeletal networks helps establish the spatial and developmental heterogeneity that underlies tissue morphogenesis.

As development proceeds, cell division continues to drive morphogenesis, shaping multicellular organization through effects on tissue stratification, epithelial packing, junctional remodeling, and polarity maintenance. Beyond embryogenesis and stem cell generation, spindle orientation remains a key regulator of tissue development, influencing both asymmetric division and daughter cell positioning within tissues. For example, in the mammalian epidermis, spindle orientation determines whether divisions in the basal layer occur parallel to the basement membrane, expanding the basal layer, or perpendicular to the basement membrane, instead stratifying the tissue by placing daughter cells into suprabasal positions (Figure 1.2B; Lechler and Fuchs, 2005). By changing daughter-cell position, oriented divisions also place cells into different local environments, altering their exposure to adhesion, signaling, and mechanical cues. These differences can influence cell fate (Williams *et al.*, 2011). Spindle orientation therefore links cell division to tissue patterning by controlling daughter-cell position and local environment.

Cell division also shapes tissue packing and organization. Within epithelia, each division alters neighbor relationships among surrounding cells. Over many rounds of proliferation, these local changes contribute to larger patterns of tissue organization (Farhadifar *et al.*, 2007; Ragkousi and Gibson, 2014). For example, ordered arrangements such as hexagonal packing can emerge from the combined effects of cell division, junctional remodeling, and mechanical energy minimization (Gibson *et al.*, 2006; Ragkousi and Gibson, 2014). Recent studies in the sea star blastula extend this idea, showing that repeated cell divisions not only increase epithelial cell density but are also associated with complex three-dimensional cell packing geometries proposed to minimize tissue surface energy (Gómez-Gálvez *et al.*, 2018; Barone *et al.*, 2024). As

proliferation increases local density, the overcrowding that results can also generate mechanical strain and trigger homeostatic responses such as cell extrusion to relieve excess cell accumulation (Eisenhoffer *et al.*, 2012). Thus, cell division reshapes epithelial organization by changing neighbor relationships, driving local rearrangements such as neighbor exchange, and generating density-dependent mechanical constraints that tissues must resolve. On a broader scale, these division patterns contribute to tissue-scale morphogenesis, including elongation, bending, and anisotropic growth (Gillies and Cabernard, 2011).

Division in epithelial tissues requires cells to remodel their junctions and polarity while remaining integrated with their neighbors. During cytokinesis, epithelial cells stay mechanically coupled to surrounding cells, requiring coordinated remodeling of cell-cell junctions. Work in *Drosophila* and *Xenopus* epithelia has shown that this remodeling helps define the geometry of daughter-cell interfaces while preserving tissue barrier function (Herszterg *et al.*, 2014; Higashi *et al.*, 2016). Division also requires the temporary remodeling and re-establishment of epithelial polarity, as mitosis and cytokinesis involve changes in cell geometry, position within the tissue layer, and cortical organization. Apical polarity regulators such as the Par complex are redistributed during mitosis and later re-established, while mitotic structures such as the midbody can provide spatial cues that help restore epithelial organization in daughter cells (Osswald and Morais-de-Sá, 2019). In some systems, septins may help coordinate these division-associated remodeling events. In *Drosophila* epidermal tissue, septins support actomyosin ring contractility as adherens junctions are locally disengaged and remodeled during cytokinesis (Founounou *et al.*, 2013). Septins have also been shown to regulate epithelial polarization through roles in microtubule organization and vesicle trafficking (Spiliotis *et al.*, 2008; Bowen *et al.*, 2011). Together, these findings suggest that epithelial cell division requires coordinated remodeling of junctions, polarity, and the cytokinetic machinery so that daughter cells remain properly integrated into the tissue.

Together, these examples show that cell division actively shapes animal tissues by linking the production of new cells to changes in tissue organization. The next section considers the converse question: how does multicellular organization reshape the demands placed on cell division?

1.4 Tissues constrain and regulate cell division

Cell division in tissues occurs within a structured and mechanically coupled environment (Figure 1.2C). As a result, cytokinesis must be adapted to the spatial, mechanical, and adhesive constraints imposed by tissues. One constraint arises from tissue geometry. Cells in epithelia are embedded within a defined architecture, and their divisions are often oriented in a way that preserves this organization (Ragkousi and Gibson, 2014). Cell-cell junctions provide positional information that helps orient the mitotic spindle within the plane of the epithelium (Nakajima *et al.*, 2013). This process depends on polarity proteins and spindle-positioning machinery, including the NuMA–dynein complex, which are themselves influenced by tissue-level signals such as Notch signaling and mechanosensitive adhesion (Williams *et al.*, 2011; Williams and Fuchs, 2013; Lechler and Mapelli, 2021). These cues also influence whether divisions occur within the plane of the epithelium or perpendicular to it, as discussed in Section 1.3 (Figure 1.2B). In addition, local cell shape and packing can bias cleavage-plane orientation, further

aligning division with tissue geometry (Gibson *et al.*, 2011). Together, these constraints require cells to integrate intrinsic polarity with external cues to position the division plane. Spindle and cleavage-plane orientation are therefore not cell-autonomous, but instead respond to the organization and signaling environment of the surrounding tissue.

Division in animal tissues is also subject to mechanical constraint. These constraints arise from various sources: the physical confinement of tissue architecture, cell–cell adhesion, and interactions with the extracellular matrix. Together, they define the physical environment in which cytokinesis must occur.

Cells in tissues undergo pronounced shape changes as they enter mitosis, beginning in early prophase when they reduce substrate adhesion and round up into a characteristic spherical form (Figure 1.2C; Dix *et al.*, 2018). This rounding is necessary for successful cell division and provides space for the mitotic spindle (Cadart *et al.*, 2014). To undergo cell rounding, however, studies in several animal models have shown that cells must generate force against their surroundings, a process that necessitates increases in cell surface tension, intracellular pressure, and cortical stiffness (Taubenberger *et al.*, 2020). When this process is limited by physical confinement, cells exhibit defects in spindle formation and chromosome segregation, indicating that force generation during rounding is required for successful division (Lancaster *et al.*, 2013). Cell rounding in animal tissues therefore provides a mechanical solution to the problem of dividing within a crowded environment.

Cell–cell and cell-ECM adhesion also constrain division. During division, epithelial cells remain connected through adherens junctions, which must be locally remodeled to allow cytokinesis to proceed (Figure 1.2C). Junctions are transiently disengaged and reformed as the furrow ingresses, enabling daughter-cell separation without disrupting tissue cohesion (Founounou et al., 2013; Guillot and Lecuit, 2013). Recent work in *Xenopus* epithelia has additionally shown that neighboring cells can mechanically restrain furrow ingression through local actomyosin contractility and junctional reinforcement (Landino *et al.*, 2025). Disrupting this coupling changes furrow speed and compromises epithelial packing and barrier integrity, highlighting the importance of neighbor-cell mechanics during cytokinesis. Division must therefore coordinate contractility with controlled remodeling of intercellular contact. Cells also maintain ECM adhesion during division through integrin-based attachments that are reorganized during mitotic rounding and re-established following cytokinesis (Figure 1.2C; Taneja *et al.*, 2016; Dix *et al.*, 2018). Furthermore, the mechanical properties of the ECM, such as stiffness, can influence late stages of cytokinesis, especially during abscission (Sambandamoorthy et al., 2015; Rabie et al., 2021). These observations indicate that division generally, and late-stage cytokinesis in particular, are sensitive to the physical properties of the extracellular environment.

Together, these constraints suggest that division in tissues requires adaptations of the molecular machinery that executes cytokinesis. Septins are one candidate component of this adaptation. In *Drosophila* epithelia, septins are required for completion of cytokinesis during divisions that occur within the plane of the tissue, but not for divisions oriented orthogonally, indicating that septin function depends on tissue context (Founounou *et al.*, 2013). Septins also regulate adherens junction remodeling and stabilize attachment of the plasma membrane to the midbody, processes that must be dynamically regulated during division in epithelia to preserve tissue

integrity (Kechad *et al.*, 2012; Founounou *et al.*, 2013; Guillot and Lecuit, 2013; Herszterg *et al.*, 2014; Higashi *et al.*, 2016). Although these studies have largely been limited to *Drosophila*, septins also stabilize the intercellular bridge in mammalian cells, consistent with a broader role in supporting cytokinesis in mechanically demanding cellular contexts (Renshaw *et al.*, 2014). Together, these findings support a role for septins during division under the constraints imposed by multicellular organization.

Cytokinesis in tissues must solve a distinct set of problems compared to division in isolated cells. Division is therefore not a fixed process, but one that has adapted to the context of multicellular life. Studying cell division in additional animal models and more physiologically relevant contexts will continue to clarify how division operates in modern tissues. However, the complex, obligate multicellular development of living animals makes it difficult to infer how these constraints first arose. As a result, it remains unclear how cytokinetic machinery adapted to meet the physical demands of multicellularity during evolution. In the next section, I ask: what were the earliest steps toward clonal multicellularity, and to what extent did division itself contribute?

Part 2. Cell division and the emergence of clonal multicellularity

2.1 Clonal and aggregative multicellularity

Multicellularity can be established either through aggregation or through clonal cell division (Figure 1.1). Aggregative multicellularity arises when non-sister cells adhere to form multicellular structures, whereas clonal multicellularity arises through repeated rounds of cell division in which daughter cells remain connected. Several examples of aggregative multicellularity suggest that modification of cell-cell and cell-ECM adhesion mechanisms is a common route to aggregation. Fruiting body formation in the social amoeba *Dictyostelium discoideum* remains one of the best-known examples of aggregative multicellularity, in which starvation triggers solitary cells to aggregate through regulated cell migration and cell-cell adhesion into a multicellular structure that subsequently develops into a fruiting body of ECM-embedded cells (Du et al., 2015). Aggregative development is also seen in flocculating *S. cerevisiae*, which forms multicellular clusters through flocculins, cell-surface proteins that mediate adhesion between cells (Lo and Dranginis, 1996; Soares, 2011). Although aggregation and clonal development were once treated as distinct strategies, recent work has shown that the choanoflagellate *Choanoeca flexa* can switch between aggregative and clonal multicellular states in response to environmental cues (Ros-Rocher *et al.*, 2026). In both states, multicellular development depends on attachments between neighboring microvillar collars, but these contacts form after division in clonal colonies and between previously separate cells in aggregative colonies (Brunet *et al.*, 2019; Ros-Rocher *et al.*, 2026).

One key distinction between clonal and aggregative multicellularity is that aggregation can bring together genetically distinct cells and is therefore susceptible to conflict among group members, whereas clonal multicellularity maintains genetic relatedness among cells (Buss, 1987). This high relatedness is thought to stabilize cooperation by limiting opportunities for exploitation by "cheater" cells (Gilbert *et al.*, 2007). This has been demonstrated in comparisons between aggregative and clonal yeast. Although aggregative yeast were more fit than clonal yeast when grown alone in a fluctuating environment, they were vulnerable to social exploitation during

direct competition: clonally developing snowflake yeast were incorporated into aggregative colonies at a higher frequency than the aggregative strains themselves (Pentz *et al.*, 2020). Additionally, the shared genetic background of clonal populations is thought to facilitate the evolution of coordinated behaviors such as differentiation and division of labor (Brunet and King, 2017).

Notably, all known examples of complex multicellularity, including plants, animals, fungi, red algae, green algae, and brown algae, arise through clonal development (Figure 1.1; Knoll, 2011), suggesting that clonal development was important for the evolution of complex multicellular structures. However, although evolutionary theory has emphasized clonality in these transitions, it has often treated cell division primarily as a means of proliferation rather than as a regulated process that can shape multicellular form. During clonal development, persistent connections among cells can be maintained through incomplete cytokinesis, which produces intercellular bridges between daughter cells, or through cell-cell and cell-extracellular matrix adhesion (Abedin and King, 2010; Brunet and King, 2017). These mechanisms differ in molecular basis, but each links the outcome of cell division to the development of multicellular structure. How regulation of cell division contributed to the establishment of clonal multicellularity remains unclear, in part because many of these transitions occurred deep in evolutionary time (Knoll, 2011). I next discuss experimentally tractable models for studying the establishment of clonal multicellularity, beginning with minimal requirements for clonal group formation (section 2.2), then focusing on mechanisms regulating cytokinesis (section 2.3) and cell adhesion (section 2.4).

2.2 Candidate interfaces between cell division and early multicellular development

Insights into the earliest steps establishing clonal multicellularity can be found through studying (1) models that transition between unicellular and multicellular states, (2) models where closely related species display differences in multicellular organization, or (3) models in which multicellularity has been experimentally evolved. These models have demonstrated that, throughout eukaryotic diversity, relatively small modifications to processes interconnected with cell division can generate persistent physical connections between cells and produce organized multicellular forms.

Several examples illustrate how changes in division-related processes can directly generate multicellular structure. Volvocine algae exhibit a range of multicellular complexity and have been used to study the evolution of multicellularity (Hoops *et al.*, 2006). Within this group, modification of conserved regulators of the cell cycle and division can alter cell number and organization. For example, expression of the retinoblastoma cell cycle regulator from the multicellular *Gonium* species in the single-celled *Chlamydomonas* was sufficient to induce colony development (Hanschen *et al.*, 2016). Meanwhile, in the more complex *Volvox* genus, genes that control the division plane (e.g., *glsA*) enable asymmetric divisions that contribute to germ-somatic differentiation (Miller and Kirk, 1999). Experimentally evolved multicellular "snowflake" yeast, another system used to investigate multicellular evolution, can arise through loss-of-function mutations in *ACE2*, an indirect regulator of daughter-cell separation (Ratcliff *et al.*, 2015). Direct changes to the regulation of cytokinesis can also promote multicellular development. Within volvocine algae, the known cytokinesis regulator *dynamin* is differentially localized in multicellular vs unicellular species, which is hypothesized to help regulate cell

orientation to facilitate colony development (Arakaki *et al.*, 2017). Together, these examples show that relatively small changes to cell-cycle progression, division patterning, or cytokinesis can promote multicellular organization.

In parallel, changes in extracellular matrix production and adhesion can generate or elaborate upon multicellular organization. In the choanoflagellate *S. rosetta*, the C-type lectin *rosetteless* localizes to the shared ECM within rosette colonies and is required for their development (Levin *et al.*, 2014). Examples are also seen in experimental evolution studies using the green algae *Chlorella vulgaris* and *Chlamydomonas*, where persistent multicellular attachment can arise through daughter-cell retention within the mother cell wall and, in some cases, through adhesion mediated by secreted gelatinous ECM material (Boraas *et al.*, 1998; Herron *et al.*, 2019). These observations show that ECM regulation can shape multicellular organization by stabilizing cell–cell connections and influencing the physical context in which daughter cells remain attached after division.

Notably, extant complex multicellular lineages use diverse cell-cell adhesion mechanisms to maintain both stable and developmentally flexible interactions (Abedin and King, 2010). In animals, these interactions often depend on membrane-bound adhesion receptors such as classical cadherins (Halbleib and Nelson, 2006; Nichols *et al.*, 2012), whereas in plants, fungi, and many algal lineages adhesion is more strongly associated with cell walls, extracellular matrices, or other lineage-specific adhesin mechanisms (Abedin and King, 2010). By contrast, in the models discussed above, which form small colonies of undifferentiated or minimally differentiated cell types, experimentally demonstrated routes to multicellularity rely primarily on incomplete cytokinesis or ECM-based adhesion rather than on membrane-bound cell-cell adhesion proteins. Therefore, while receptor-mediated adhesion can support more elaborate multicellular organization, it may not have been the primary route by which early clonal multicellular forms were established.

Together, these observations suggest that clonal multicellular organization can emerge through relatively few modifications to processes closely linked to cell division. These processes can be broadly grouped into two functional categories: regulation of cytokinesis and regulation of the extracellular matrix. Cytokinesis regulation can generate persistent connections between daughter cells. Among cytokinesis-linked routes, persistent intercellular bridges are especially compelling because they provide a direct physical link between cell division and multicellular organization. As a distinct but complementary route, ECM regulation can stabilize multicellular structure and alter the physical context in which division occurs. In the following sections, I examine these two modes of multicellular development in more detail.

2.3 Cytokinesis regulation as a route to multicellularity

Relatively few changes to cell division can result in the loss of cell separation (Brunet and King, 2017). One such change occurs through the formation of persistent intercellular bridges. Intercellular bridges are cytoplasmic connections that occur between daughter cells when cell division completes without abscission, providing a particularly clear example of how cytokinesis regulation can generate connections between cells. Additionally, intercellular bridges are widespread across clonally multicellular eukaryotes, including all complex multicellular

lineages, suggesting that intercellular bridge formation has been a recurrent innovation (Figure 1.3A; Knoll, 2011; Chaigne and Brunet, 2022).

Despite the common outcome of retained cytoplasmic connections following division, the underlying routes to intercellular bridge formation differ across lineages. In animals, fungi, and red algae, intercellular bridges generally arise when constriction during cytokinesis proceeds but ultimately remains incomplete, leaving a persistent continuity between daughter cells (Figure 1.3A; Suzuki *et al.*, 1995; Berepiki *et al.*, 2010; Haglund *et al.*, 2011). In land plants and brown algae, intercellular bridges instead form during cell plate formation at sites where wall deposition is locally interrupted, forming plasmodesmata (Jürgens, 2005; Terauchi *et al.*, 2015). Thus, intercellular bridges can emerge through distinct cytokinetic mechanisms, but in each case, they preserve direct physical continuity between sister cells.

Species that form small multicellular colonies provide additional examples of intercellular bridge formation in eukaryotes. In volvocine algae, daughter cells in multicellular species often remain connected by intercellular bridges (Hoops *et al.*, 2006). In colonial forms with undifferentiated cells, such as *Gonium* species, intercellular bridges can persist throughout the life of the colony, whereas in species with cell-type differentiation they are most prominent early in development and may later be supplemented or replaced by extracellular matrix-mediated cohesion (Figure 1.3B; Hoops *et al.*, 2006). Another example comes from choanoflagellates, where several species, including *S. rosetta*, *Desmarella moniliformis* Kent, and *Codosiga botrytis*, all form colonies connected by intercellular bridges which share structural features hypothesized to be homologous (Figure 1.3A and 1.3B; Hibberd, 1975; Karpov and Coupe, 1998; Dayel *et al.*, 2011; Chaigne and Brunet, 2022). These observations suggest that persistent intercellular bridges can provide an early route to clonal multicellular organization, although the evolutionary history and mechanistic basis of intercellular bridge formation outside animals and fungi remain poorly resolved.

The mechanisms underlying intercellular bridge formation have been studied most extensively in animals. There, intercellular bridge formation is a regulated form of incomplete abscission. In animal germline tissues, where intercellular bridges are almost universally present, they are developmentally stabilized to produce interconnected cell groups called germ cysts, and often retain persistent microtubules and midbody-derived material (Pepling *et al.*, 1999; Greenbaum *et al.*, 2011; Hu *et al.*, 2012a). In the *Drosophila* germline, ring canals form through incomplete cytokinesis mediated by control of myosin II activity (Ong *et al.*, 2010; Haglund *et al.*, 2011). In mammals, germline intercellular bridge stabilization can instead occur through sequestration of the scaffold protein CEP55, which blocks recruitment of ESCRT machinery to the abscission site (Iwamori *et al.*, 2010). Shorter-term intercellular bridge stabilization in animals also depends on restrained ESCRT function and related checkpoint mechanisms, including regulation by the mitotic kinase Aurora B (Carlton *et al.*, 2012; Mierzwa and Gerlich, 2014). Nascent intercellular bridges can be further stabilized by structural components that can include F-actin, anillin, septins, filamin, and myosin II (Estey *et al.*, 2010; Amini *et al.*, 2014; Chaigne and Brunet, 2022). For example, mammalian SEPT2 is necessary to scaffold myosin II at nascent intercellular bridges, leading to collapse of the nascent intercellular bridge when this interaction is lost (Joo *et al.*, 2007). Additionally, mammalian SEPT9 has specifically been shown to regulate intercellular bridge abscission; loss of SEPT9 in HeLa cells leads to persistent bridge

connections, suggesting a role for SEPT9 in abscission delay (Estey *et al.*, 2010). Together, these findings show that animal intercellular bridges are not simply failed endpoints of cytokinesis, but regulated developmental modifications of the normal abscission program.

Intercellular bridges can contribute to multicellular development in several ways. In addition to maintaining physical continuity between cells, they may support communication between connected cells and help coordinate development (Chaigne and Brunet, 2022). Some of these functions have now been shown directly. In the male mouse germline, intercellular bridges allow cytoplasmic exchange between connected germ cells and are required for normal meiotic progression, transposon repression, and protection of genome integrity during spermatogenesis (Figure 1.3A; Sorkin *et al.*, 2025). In *Hydra vulgaris*, both germline and somatic intercellular bridges share conserved structural and molecular features, and cells connected by ring canals show coordinated cell-cycle behavior (Figure 1.3A; Price *et al.*, 2025). These findings suggest that intercellular bridges are not only structurally conserved across animals, but have evolved, in part, to support coordinated cell behavior.

The broad distribution of intercellular bridges across eukaryotes, along with the relatively few modifications required for the formation, raises the possibility that bridge formation has been repeatedly used as a route to multicellularity. At the same time, the molecular basis and functional roles of intercellular bridges remain poorly understood outside the best-studied animal systems (Chaigne and Brunet, 2022). This gap helps motivate the study of colony development in groups such as choanoflagellates, where cytokinesis and multicellular organization can be examined together in a close relative of animals.

2.4 Extracellular matrix regulation as a route to multicellularity

Attachment through a shared extracellular matrix is a common feature of many complex multicellular eukaryotes (Figure 1.3C; Kloareg *et al.*, 2021). Species with less developmentally elaborate multicellular forms also use ECM to organize colony structure (Figure 1.3D; Dayel *et al.*, 2011; Du *et al.*, 2015; Herron, 2016). ECM is therefore a candidate both for early steps towards multicellularity and during subsequent elaboration of multicellular structure. From the perspective of cell division, the appearance of a shared ECM may also have changed the physical environment in which cytokinesis occurred (Sambandamoorthy *et al.*, 2015; Larson *et al.*, 2020). In this section, I consider how ECM supports the evolution of multicellular organization and then ask how ECM-based attachment may reshape the mechanics of cell division.

Extracellular matrix is used as an organizing material in a range of species that form small multicellular structures. In volvocine algae, single-celled species are surrounded by a hydroxyproline-rich glycoprotein wall, while in colonial forms this material is expanded to become a shared ECM (Kirk *et al.*, 1986; Nishii and Miller, 2010). In lineages such as *Pleodorina*, which form colonies of undifferentiated cells, shared ECM is established between cells during morphogenesis and helps organize colony formation (Figure 1.3D), whereas in more developmentally complex lineages such as *Volvox*, the ECM is much more elaborate and occupies most of the colony volume (Kirk *et al.*, 1986; Nishii and Miller, 2010). The choanoflagellate *S. rosetta* provides another clear example of the formation of small colonial forms through ECM attachment. In *S. rosetta*, rosette colonies are anchored by a basal ECM that

is secreted as cells divide, linking each daughter cell pair and contributing directly to the integrity and organization of the developing colony (Figure 1.3C; Dayel *et al.*, 2011; Levin *et al.*, 2014; Larson *et al.*, 2020). Consistent with this function, rosette development depends on genes required for ECM production and modification, mechanisms which will be discussed in more detail in section 3.3 (Levin *et al.*, 2014; Wetzel *et al.*, 2018; Combredet *et al.*, 2025). Interestingly, another close animal relative, *Capsaspora owczarzaki*, which instead develops through aggregation, encodes an integrin-based adhesion toolkit (i.e., genes whose homologs mediate cell-ECM attachment in animals) (Sebé-Pedrós *et al.*, 2010), much of which is upregulated during multicellular development (Sebé-Pedrós *et al.*, 2013). In addition, *Capsaspora* uses integrin-mediated adhesion during substrate attachment through filopodia, although its roles in multicellular development remain unclear (Parra-Acero *et al.*, 2020). These examples suggest that extracellular matrix regulation may have contributed to the early establishment of multicellular structure.

Complex multicellular species provide examples of more elaborate ECM use. In animals, for example, ECM provides structural support and helps to coordinate cell behavior (Yurchenco, 2011). The basal lamina, one of the defining features of animal epithelia, is a specialized, collagen-rich ECM that serves as both a physical scaffold and a signaling platform (Figure 1.2C and 1.3C; Yurchenco, 2011). Cells connect to the basal lamina through integrins, membrane-bound receptors that underlie the formation of focal adhesions and hemidesmosomes (Yurchenco, 2011). In addition to its well-characterized roles in structural support, animal ECM can also actively shape morphogenesis through its remodeling, organization, and force-generating properties (Díaz-de-la-Loza and Stramer, 2024). Land plants likewise depend on an extracellular structural matrix in the form of the cell wall, which is composed primarily of cellulose, hemicellulose, and pectin, and plays a central role in plant development (Somerville *et al.*, 2004; Delmer *et al.*, 2024). Fungi similarly build multicellular structure through elaborating on a chitin- and glucan-rich cell wall with other adhesive extracellular materials, the composition of which is heterogeneous across species and comparatively less understood (Nagy *et al.*, 2020; Gow, 2025). Across these lineages, extracellular structures are central to the organization and maintenance of large, complex multicellular forms.

The introduction and elaboration of ECM during the evolution of multicellularity altered the physical environment in which cytokinesis occurs, with dividing cells now encountering new spatial, adhesive, and mechanical constraints. Work in cultured mammalian cells supports this idea. In fibroblasts, matrix stiffness can directly affect whether cytokinesis completes successfully; soft substrates induced late-stage cytokinesis failure, consistent with defects in bridge stabilization or abscission (Sambandamoorthy *et al.*, 2015). Another example comes from mammary epithelial cells undergoing epithelial-to-mesenchymal transition, where stiff microenvironments promote abscission failure through integrin-dependent signaling that alters expression of midbody-associated cytokinetic proteins (Rabie *et al.*, 2021). In addition, ECM binding and integrin activation regulate SEPT7 at focal adhesions in fibroblasts, supporting the idea that ECM cues can be translated into septin-dependent mechanosensing pathways (Sturgess et al., 2024). The interplay between cell division and ECM attachment can also be studied in *S. rosetta*, where rosette cells continually secrete and attach to ECM as they proliferate. Laser ablation studies show that ECM constrains proliferating cells during rosette development,

suggesting that rosette cells encounter a mechanically constraining environment not experienced by single-celled *S. rosetta* forms (Larson *et al.*, 2020).

ECM therefore does not only scaffold and enable a range of multicellular development, but can also recontextualize how cell division occurs within that structure. In this way, ECM attachment represents a second major route, alongside incomplete cytokinesis, by which cell division and multicellular organization may have become linked during early animal evolution. Choanoflagellates provide a useful system for studying this connection, because they form experimentally tractable multicellular colonies through serial cell division while also using ECM to organize colonial development.

Part 3. Choanoflagellates as a model for studying cell division in the animal stem lineage

3.1 Choanoflagellates and the animal stem lineage

Choanoflagellates are the closest living relatives of animals, making them a key comparative group for studying animal origins (Figure 1.1; Carr *et al.*, 2008; King *et al.*, 2008; Ruiz-Trillo *et al.*, 2008). Beyond their phylogenetic placement, choanoflagellates share cellular features that make them especially relevant to thinking about animal evolution (Dayel *et al.*, 2011; Brunet and King, 2017). Choanoflagellates are aquatic microbial eukaryotes that bear a diagnostic collar complex comprising an apical flagellum surrounded by a ring of actin-rich microvilli (Figure 1.4A; Karpov and Leadbeater, 1998; Leadbeater, 2015; Booth *et al.*, 2018). This cell architecture closely resembles sponge choanocytes and is also broadly comparable to the apicobasal polarity found in animal epithelial cells (Leadbeater, 2015; Buckley and Johnston, 2022). They also lack the rigid cell wall found in most fungi, making them a useful system for studying cortical mechanics, cytokinesis, and multicellular interactions in a context more directly relevant to animal origins (Leadbeater, 2015; Gow, 2025).

Genomic studies have further shown that choanoflagellates encode many genes critical for animal multicellularity that were once thought to be restricted to animals, including cadherins, C-type lectins, and diverse tyrosine kinases (King *et al.*, 2008; Fairclough *et al.*, 2013). This repertoire of adhesion, signaling, and extracellular matrix-related genes allows choanoflagellates to be used as experimentally tractable systems for studying how genes relevant to multicellularity functioned before animal diversification (Nichols *et al.*, 2012; Levin *et al.*, 2014; Booth and King, 2022).

Choanoflagellates are particularly relevant to the questions posed throughout this introduction because clonal development occurs repeatedly within the group. Multiple species, including *S. rosetta*, *Barroeca monosierra*, *Desmarella moniliformis* Kent, *Codosiga botrytis*, and *C. flexa* have the ability to form multicellular colonies following serial rounds of cell division (Hibberd, 1975; Karpov and Coupe, 1998; Fairclough *et al.*, 2010; Hake *et al.*, 2024; Ros-Rocher *et al.*, 2026). This recurring feature of clonal multicellular development throughout choanoflagellates makes this group a particularly useful system for studying how cell division and multicellular organization interact.

Additionally, choanoflagellates are developmentally flexible. This is exemplified by *S. rosetta*, which has a complex life history, including single-celled and multicellular forms, swimming and attached states, and a sexual life cycle (Dayel *et al.*, 2011; Levin and King, 2013; Levin *et al.*, 2014; Woznica *et al.*, 2017). Many of these transitions, including the unicellular-multicellular switch, are regulated by bacterial and algal cues (Fairclough *et al.*, 2010; Perotti *et al.*, 2025), allowing for experimental control over development. Together, these cellular, genomic, and experimental features make choanoflagellates a powerful comparative system for investigating how cell division and multicellularity may have been linked during the evolution of animals.

3.2 Cell division in choanoflagellates

Ultrastructural studies across choanoflagellates have revealed broad conservation of several mitotic events (Leadbeater, 2015). Before mitosis, the flagellum is withdrawn, basal bodies separate to help organize the spindle at the poles, and new flagella are rapidly re-established following anaphase (Figure 1.4B; Leadbeater, 1994; Karpov and Leadbeater, 1997). In choanoflagellate cell types without restrictive coverings, including swimming *S. rosetta* cells, the nuclear spindle is positioned perpendicular to the long axis of the cell, and cytokinesis proceeds along the longitudinal cell axis (Figure 1.4B; Karpov and Leadbeater, 1997; Leadbeater, 2015). This orientation is also seen in cells within multicellular rosette colonies of *S. rosetta*, where the resulting division plane positions the spindle parallel to the colony surface and may help maintain spherical colony geometry during rosette development (Anderson *et al.*, 2016). Notably, in thecate *S. rosetta* cells, which are nestled within an organic covering, and in other choanoflagellate species and cell types with more restrictive coverings, including loricate choanoflagellates that reside within a silica structure, spindle and division-plane positioning are more variable (Leadbeater, 1994, 2015).

Another notable feature of choanoflagellate cytokinesis is that in several species, daughter cells remain physically connected after division. Rosette colonies of *S. rosetta, Desmarella moniliformis* Kent, and *Codosiga botrytis* are each connected by persistent intercellular bridges with a similar two-plate pattern of dense-staining structures at the bridge center (Figure 1.3A; Hibberd, 1975; Karpov and Coupe, 1998; Dayel *et al.*, 2011; Fairclough *et al.*, 2013). Choanoflagellate cell division therefore occurs within a polarized architecture in which basal bodies help position the spindle and, in some cases, division also produces persistent physical connections between colonial cell types. These features make choanoflagellates a relevant comparative system for studying how cell division may have operated during early animal evolution.

3.3 *S. rosetta* is a useful model for studying cell division and multicellular development

Among choanoflagellates, *S. rosetta* is a particularly useful model for studying cell division and multicellular development. One key strength of *S. rosetta* is that it transitions between unicellular and multicellular states in a way that can be experimentally controlled (Alegado *et al.*, 2012; Perotti *et al.*, 2025): a single *S. rosetta* culture can be separated into uninduced and rosette-induced conditions before any experiment, allowing the effects of genetic perturbation to be compared directly between these states (Figure 1.4C). Another strength of *S. rosetta* is that it is genetically tractable, with both forward and reverse genetic approaches available, including

mutant screens, CRISPR-based genome editing, and transfection of fluorescent constructs for live-cell analysis (Levin and King, 2013; Levin *et al.*, 2014; Booth *et al.*, 2018; Booth and King, 2020; Combredet *et al.*, 2025).

S. rosetta has a rich life history, including solitary "slow swimmer" cells, linear "chain" colonies, spherical rosette colonies, substrate-attached thecate cells, and a sexual life cycle (Dayel *et al.*, 2011; Levin and King, 2013; Levin *et al.*, 2014; Woznica *et al.*, 2017). The two *S. rosetta* colony types, chains and rosettes, both form through serial rounds of cell division and are connected by intercellular bridges resulting from incomplete cytokinesis (Figure 1.4C; Dayel *et al.*, 2011), although the structural and molecular similarity between these two types of bridges is unknown. Rosettes are additionally anchored by a basal ECM that is secreted shortly following induction by either bacterial sulfonolipids (Alegado *et al.*, 2012) or algal polysaccharides (Figure 1.4C; Perotti *et al.*, 2025). As early as the two-cell stage of rosette development, daughter cells share an ECM scaffold (Figure 1.3C; Larson *et al.*, 2020). Rosette development progresses from a 2D stage (2 – 4 cells) to a 3D stage (5+ cells), ultimately forming a spherical colony where cells are connected to an interior ECM and where basal filopodia protrude into the ECM space, perhaps helping to further anchor the cells (Dayel *et al.*, 2011; Larson *et al.*, 2020). Cells within rosettes are polarized, with their basal poles facing inward and their apical collar complexes facing outward, and the resulting colonies are mechanically robust relative to chain colonies (Wetzel *et al.*, 2018; Larson *et al.*, 2020). Rosette development is therefore not simply a failure of cell separation, but a morphogenetic process that couples cytokinesis, polarity, and extracellular organization (Larson *et al.*, 2020).

Genetic and molecular studies have revealed that rosette development depends on genes required for ECM production and modification, including the C-type lectin *rosetteless*, which localizes to the basal ECM during colony development (Figure 1.3C), and the predicted glycosyltransferases *jumble* and *couscous* (Figure 1.4D and 1.4D'; Levin *et al.*, 2014; Wetzel *et al.*, 2018). Hippo signaling has also recently been found to regulate colony size, likely through effects on ECM regulation (Figure 1.4D'; Combredet *et al.*, 2025). Additional classes of rosette-defective mutants have been identified through phenotypic screens, although the genetic bases of their phenotypes remain unknown. One mutant of particular interest is Solo, which is unable to form either chain colonies or rosettes, suggesting a defect in a process common to both colony types, potentially cytokinesis or intercellular bridge regulation (Figure 1.4D"; Levin *et al.*, 2014). Other categories of potential rosette regulators, including factors involved in sensing and responding to rosette-induction cues, factors involved in cell-ECM attachment at the basal pole, and other direct components of the basal ECM, have not yet been identified. However, comparison of slow-swimmer/chain cultures and rosette cultures reveals almost no differences in gene expression, suggesting that much of the differentiation may occur through post-transcriptional regulation (Fairclough *et al.*, 2013). Together, these features make *S. rosetta* a powerful system for studying how cell division, polarity, and extracellular organization interact during multicellular development.

3.4 Septins as candidate regulators of cytokinesis in multicellular contexts

Septins are strong candidates for understanding how cytokinesis is coordinated with multicellular organization. As highlighted throughout this chapter, the functions of septins in cell division

depend on the multicellular context and also extend to other areas of multicellular organization. In animals, septins help organize the cleavage furrow, regulate intercellular bridge stability and abscission, and contribute to epithelial polarity, junction remodeling, and division within tissues (Estey *et al.*, 2010; Bowen *et al.*, 2011; Founounou *et al.*, 2013; Mierzwa and Gerlich, 2014; Higashi *et al.*, 2016; Carim *et al.*, 2020; Sturgess *et al.*, 2024). These roles place septins at a point of direct overlap between cytokinesis and multicellular organization.

Prior work in choanoflagellates suggested that septins may serve functions similar to those in animals. An earlier transcriptomic analysis suggested that septin transcripts were enriched in colonial cell types (Fairclough *et al.*, 2013); however, as described in Chapter 2, re-analysis using a more recent dataset did not confirm this enrichment (Leon *et al.*, 2025). Transient expression studies further showed that *Sros*_SeptA and *Sros*_Sept6 localize basally in single cells and chains, and that this localization is disrupted by deletion of the coiled-coil domain, suggesting that choanoflagellate septins contribute to polarized cortical organization and that this distribution depends on higher-order septin assembly (Booth *et al.*, 2018). Septins have also been observed to co-localize with actin during myosin-regulated blebbing during the flagellate-to-amoeboid transition, further supporting a role in dynamic cortical remodeling (Brunet *et al.*, 2021). Septins are therefore plausible mediators of the coordination between cytokinesis and multicellular development in *S. rosetta*. In Chapter 2, I demonstrate that septins regulate cytokinesis in *S. rosetta* and that this requirement is heightened in the colonial context. This provides an experimental system for investigating how the regulation of cell division became integrated with multicellular development during the early evolution of animals.

Chapter 1 Figures

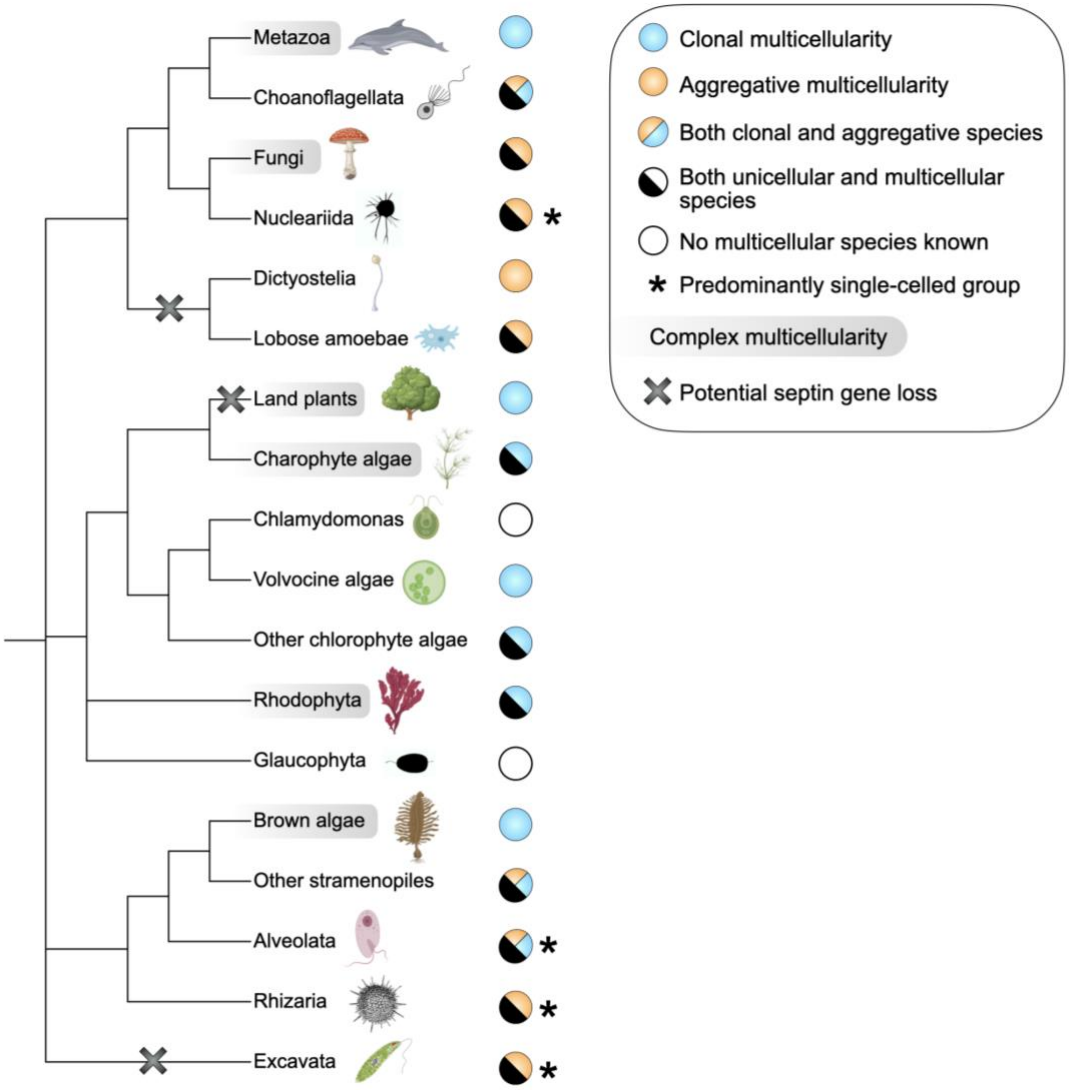

Figure 1.1. Distribution of multicellular form and septin conservation throughout eukaryotes. Both clonal and aggregative multicellularity are widespread throughout eukaryotes; however, every instance of complex multicellularity results from clonal development. Septins are also widespread in eukaryotes, although septin gene loss is hypothesized to have occurred in Amoebozoa, land plants, and Excavata (Delic *et al.*, 2024). A simplified eukaryotic tree is shown to highlight the relevant relationships among the lineages discussed in Chapter 1. Phylogenetic relationships were based on (Burki *et al.*, 2020), and the multicellular characteristics of each group were determined from (Sebé-Pedrós *et al.*, 2017; Ros-Rocher *et al.*, 2026). Representative lineage illustrations were assembled using the BioRender.com library, except for Nucleariida and Glaucophyta (phylopic.org) and choanoflagellates (custom-drawn).

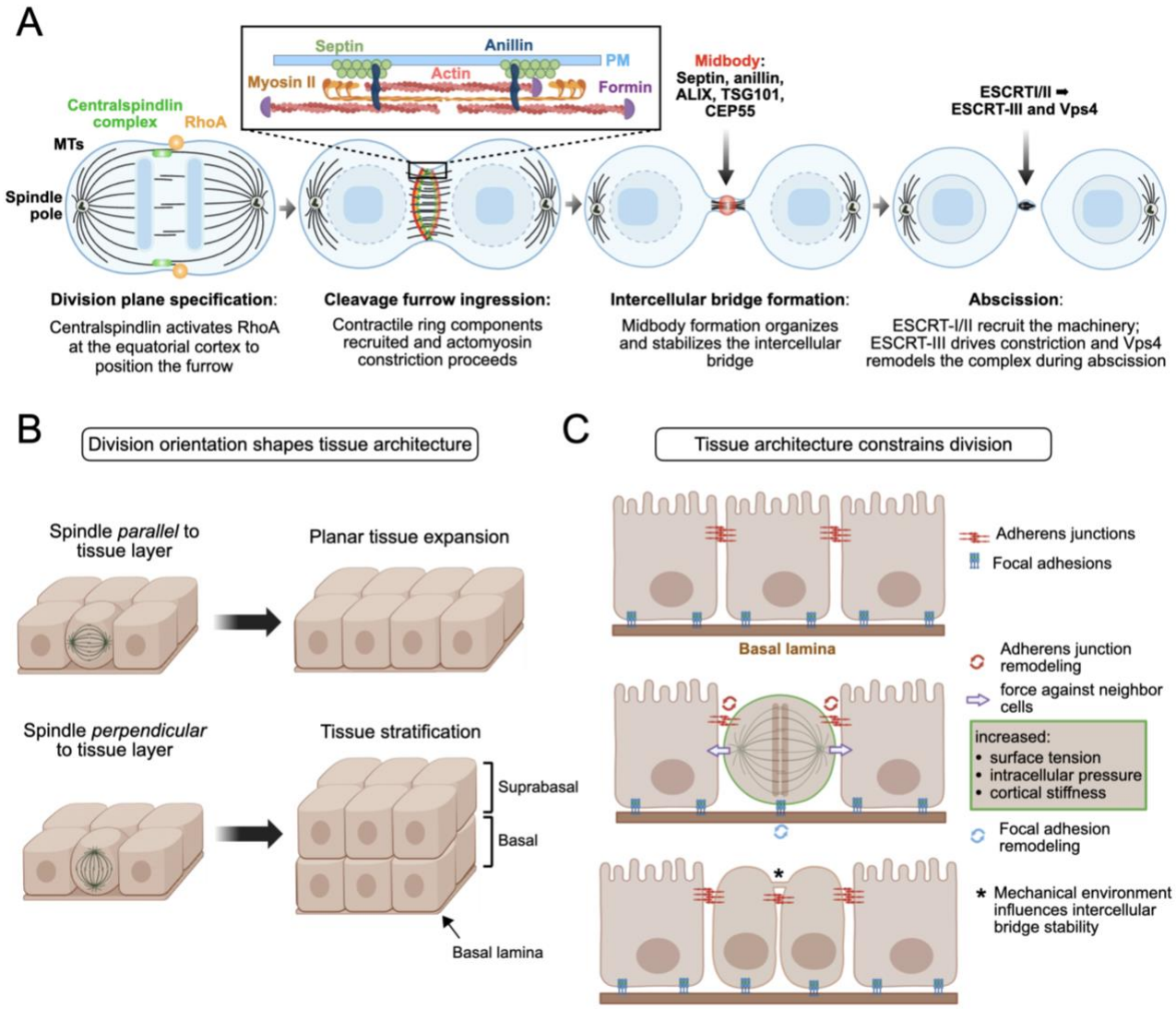

Figure 1.2. Cytokinesis in animal cells and tissues. (A) Schematic overview of cytokinesis in animal cells. Division-plane specification begins with spindle-derived cues that position the equatorial cortex, followed by contractile-ring assembly and cleavage furrow ingression. As ingression completes, the furrow transitions into a narrow intercellular bridge containing a midbody, and final abscission follows (Green *et al.*, 2012). (B) Cell division orientation shapes tissue architecture. Divisions parallel to the plane of an epithelium expand the planar tissue layer, whereas divisions perpendicular to that plane can reposition daughter cells and contribute to tissue stratification (Kulukian and Fuchs, 2013). (C) Tissue architecture affects cell division. Epithelial cells divide while maintaining attachment to neighbors and the extracellular matrix, requiring local remodeling of adherens junctions and focal adhesions during mitotic rounding and cytokinesis (Guillot and Lecuit, 2013; Cadart *et al.*, 2014; Taneja *et al.*, 2016). Increased surface tension, intracellular pressure, and cortical stiffness help the mitotic cell round within the tissue, and the mechanical context within tissues influences intercellular bridge stability (Lafaurie-Janvore *et al.*, 2013; Kamranvar *et al.*, 2016; Taubenberger *et al.*, 2020). Images for panels A-C were created, in part, with BioRender.com.

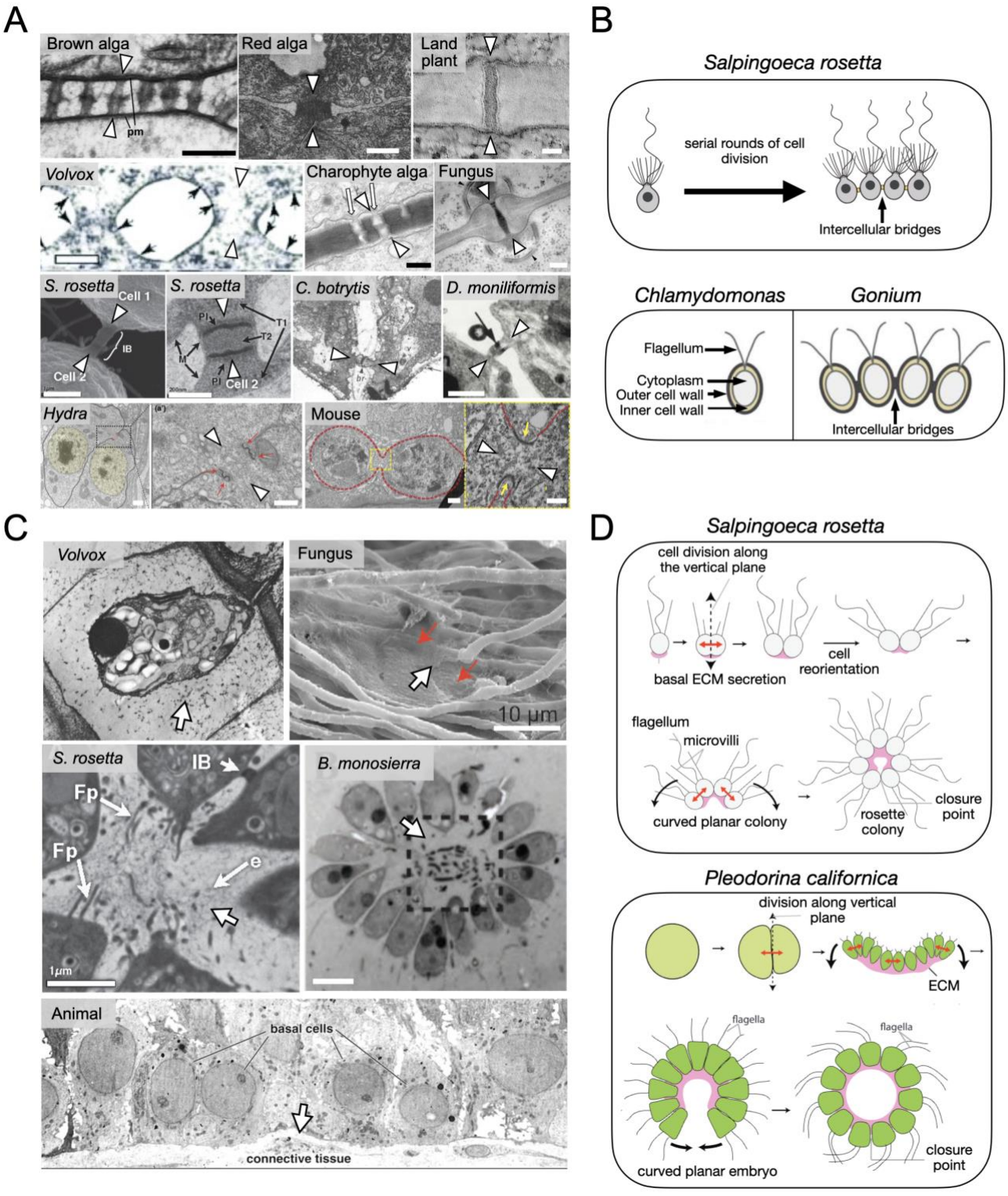
A
Brown alga
pm
Red alga
Land plant
Volvox
Charophyte alga
Fungus
S. rosetta
Cell 1
IB
Cell 2
S. rosetta
PI
T1
T2
M
PI
Cell 2
C. botrytis
br
D. moniliformis
Hydra
Mouse
B
Salpingoeca rosetta
serial rounds of cell division
Intercellular bridges
Chlamydomonas
Gonium
Flagellum
Cytoplasm
Outer cell wall
Inner cell wall
Intercellular bridges
C
Volvox
Fungus
10 µm
S. rosetta
IB
Fp
Fp
e
1µm
B. monosierra
Animal
basal cells
connective tissue
D
Salpingoeca rosetta
cell division along the vertical plane
basal ECM secretion
cell reorientation
flagellum
microvilli
curved planar colony
rosette colony
closure point
Pleodorina californica
division along vertical plane
ECM
flagella
flagella
curved planar embryo
closure point

Figure 1.3. Intercellular bridges and extracellular matrix across eukaryotes. (A) Intercellular bridges across eukaryotes. White arrowheads mark either side of the intercellular bridge examples. Order proceeds from top left to bottom right, read left to right. (1) Brown alga: plasmodesmata between *Dictyota dichotoma* epidermal cells, electron micrograph; pm, plasma membrane. Scale bar, 200 nm (Terauchi *et al.*, 2015). (2) Red alga: pit connections between two *Pseudogloiophloea confusa* cells, electron micrograph. Scale bar, 0.5 μm (Ramus, 1969). (3) Land plant: plasmodesmata connecting root tip cells in *Arabidopsis*, electron tomography image. Scale bar, 40 nm (Nicolas *et al.*, 2017). (4) Volvox: *Volvox carteri* embryos, TEM micrograph; black arrowheads indicate obliquely sectioned membrane striations, visible as short dark stripes. Scale bar, 200 nm (Hoops *et al.*, 2006). (5) Charophyte alga: plasmodesmata in the thallus of *Chara corallina*, TEM micrograph; white arrows point towards two plasmodesmata. Scale bar, 300 nm (Domozych and Domozych, 2014). (6) Fungus: *Schizophyllum commune* septum structure, electron micrograph; black arrowheads indicate parenthesomes, cap-like membrane structures flanking the pore. Scale bar, 0.2 μm (Bauer *et al.*, 2006). (7) *S. rosetta*: intercellular bridge in the choanoflagellate *Salpingoeca rosetta*, TEM micrograph (left) and scanning electron micrograph (right); T, texture of cytoplasm; M, cell membrane; PI, bridge plate. Scale bars, 200 nm (left), 1 μm (right) (Dayel *et al.*, 2011). (8) *C. botrytis*: intercellular bridge in the choanoflagellate *Codosiga botrytis*, shadow-cast electron micrograph; br, intercellular bridge. Magnification, ×10,000 (Hibberd, 1975). (9) *D. moniliformis*: intercellular bridge in the choanoflagellate *Desmarella moniliformis*, electron micrograph of an ultrathin section; black arrow indicates dark staining region of the intercellular bridge. Scale bar, 1 μm (Karpov and Coupe, 1998). (10) *Hydra*: *Hydra vulgaris* ring canals in interstitial stem cell pairs, TEM micrograph; black outline indicates daughter cell boundaries (left); red arrowheads indicate connections of the bridge to the plasma membrane of both cells (right). Scale bars, 1 μm (left), 500 nm (right) (Price *et al.*, 2025). (11) Mouse: *Mus musculus* testis, electron micrograph; dashed red outlines indicate daughter cell boundaries; yellow arrowheads indicate the intercellular bridge membrane (right). Scale bars, 2 μm (left), 500 nm (right) (Sorkin *et al.*, 2025). Panel design and selected content were adapted from (Chaigne and Brunet, 2022). (B) Examples of undifferentiated clonal development through intercellular bridge formation in choanoflagellates (top) and volvocine algae (bottom). Top: In *S. rosetta,* serial rounds of cell division generate colonies in which sister cells remain linked by intercellular bridges, illustrating a transition between unicellular and multicellular states within a species (Dayel and King, 2014). Bottom: *Gonium*, a close relative of the unicellular *Chlamydomona*s, forms colonies in which daughter cells remain connected by intercellular bridges, illustrating a transition in multicellular organization between closely related species (Hoops *et al.*, 2006). Image adapted from (Abedin and King, 2010). (C) Extracellular matrix (ECM) across eukaryotes. White arrows mark ECM regions. Order proceeds from top left to bottom right, read left to right. (1) *Volvox*: *Volvox globator* somatic tissue, electron micrograph of DAB-stained thin-section tissue, magnification ×10,000 (Kirk *et al.*, 1986). (2) Fungus: *Aspergillus fumigatus* biofilm, SEM micrograph; red arrows indicate ECM material connecting hyphae. Scale bar, 10 μm (Reichhardt *et al.*, 2015). (3) *S. rosetta*: rosette colony midsection in the choanoflagellate *Salpingoeca rosetta*, thin-section TEM micrograph; Fp, filopodia; IB, intercellular bridge; e, extracellular matrix. Scale bar, 1 μm (Dayel *et al.*, 2011). (4) *B. monosierra*: rosette colony midsection in the choanoflagellate *Barroeca monosierra*, thin-section TEM micrograph; dashed black box partially outlines ECM material at the center of the colony, along with bacteria (small dense staining patches). Scale bar, 5 μm (Hake *et al.*, 2024). (5) Animal: mammalian pseudostratified epithelium, basal portion,

TEM micrograph. Magnification, ×4,000 (Ross and Pawlina, 2006). (D) Examples of undifferentiated clonal development through ECM regulation in *S. rosetta* (top) and the volvocine alga *Pleodorina californica* (bottom). Top: In *S. rosetta*, rosettes develop around a shared basal extracellular matrix (C) while retaining intercellular bridges (A). Bottom: In some volvocine algae, including *P. californica*, embryos likewise develop within an expanded extracellular compartment and retain intercellular bridge connections during early morphogenesis. Image adapted from (Brunet and King, 2017).

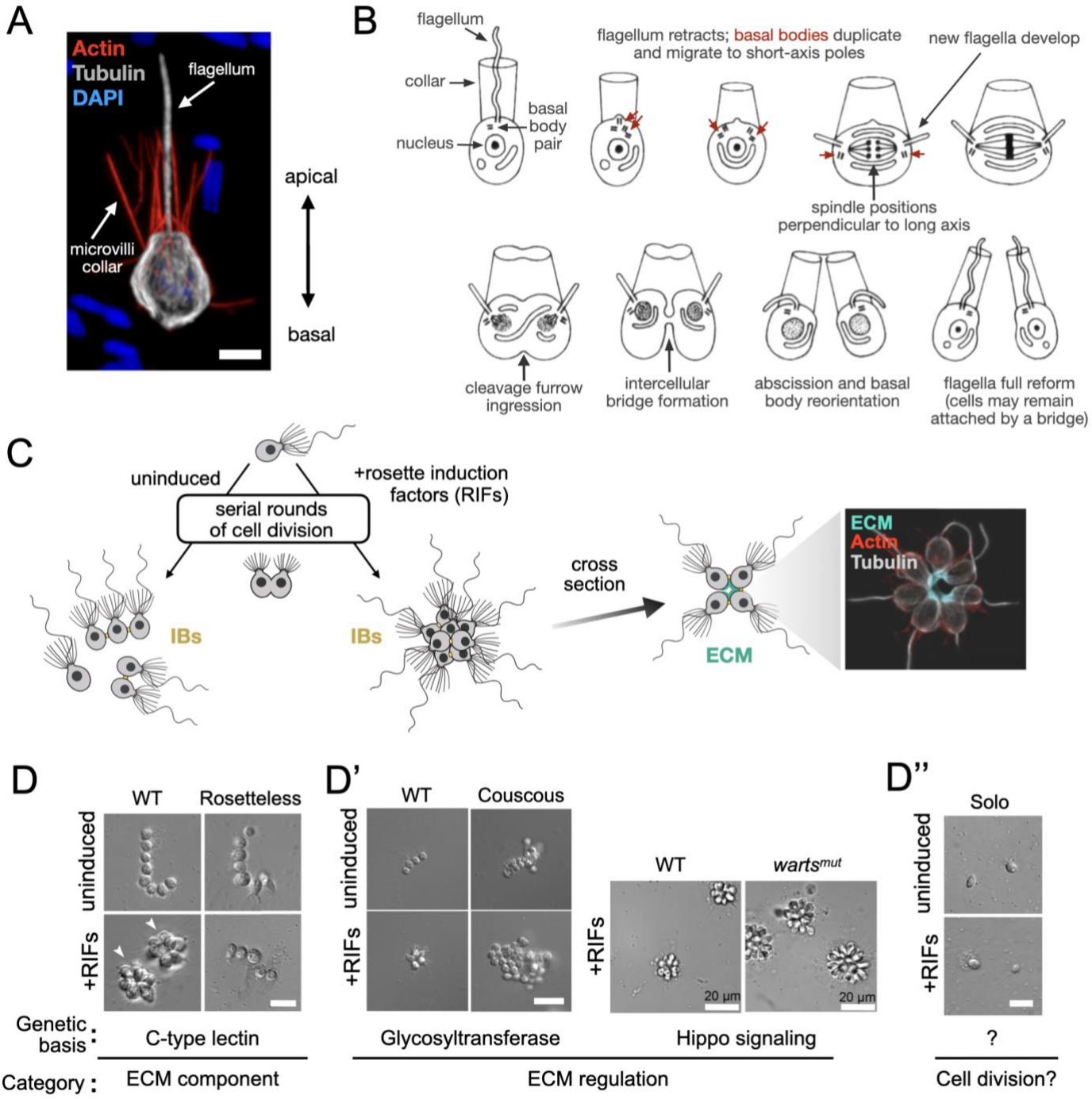
A
Actin
Tubulin
DAPI
flagellum
microvilli collar
apical
basal
B
flagellum
collar
basal body pair
nucleus
flagellum retracts; basal bodies duplicate and migrate to short-axis poles
new flagella develop
spindle positions perpendicular to long axis
cleavage furrow ingression
intercellular bridge formation
abscission and basal body reorientation
flagella full reform (cells may remain attached by a bridge)
C
uninduced
+rosette induction factors (RIFs)
serial rounds of cell division
IBs
IBs
cross section
ECM
ECM
Actin
Tubulin
D
WT
Rosetteless
uninduced
+RIFs
Genetic basis:
C-type lectin
Category:
ECM component
D'
WT
Couscous
uninduced
+RIFs
Glycosyltransferase
WT
warts^mut
+RIFs
20 µm
20 µm
Hippo signaling
ECM regulation
D''
Solo
uninduced
+RIFs
?
Cell division?

Figure 1.4. *S. rosetta* as a model to study the evolution of cell division and multicellular development in the animal stem lineage. (A) Choanoflagellates have apicobasal polarity, with an apical collar complex comprised of a single flagellum (grey; tubulin stain) surrounded by a ring of actin-rich microvilli (red, phalloidin stain). The choanoflagellate *Salpingoeca rosetta* is shown. Image adapted from (Booth and King, 2020). Scale bar, 2 μm. (B) Choanoflagellate cell division proceeds through flagellar retraction, basal body duplication and movement to orient the mitotic spindle perpendicular to the long axis of the cell (red arrows), longitudinal cytokinesis, and production of either separated daughter cells or daughter cells that remain bridge-connected after division. Shown is a schematic of nuclear and cell division in craspedid choanoflagellates (such as *S. rosetta*) adapted from (Karpov and Leadbeater, 1997). (C) Left: The multicellular state in *S. rosetta* can be experimentally controlled. Under standard conditions, *S. rosetta* produces a mixture of single cells and chain colonies formed through serial rounds of cell division and connected by intercellular bridges (dark yellow, IBs), while exposure to rosette-inducing cues promotes formation of spherical, shear-resistant colonies called rosettes, connected by intercellular bridges and an interior ECM that daughter cells secrete and attach to at their basal pole as they divide (ECM not visible in this illustration, see cross section to the right) (Dayel *et al.*, 2011). Right: Rosettes are connected by a basal ECM (teal) (Levin *et al.*, 2014). Actin (red) and tubulin (white) organization in rosettes is also shown. (D-D'') Several genes have been shown to regulate rosette development. (D) The causative mutation in the mutant Rosetteless is in a C-type lectin called *rosetteless*, the protein product of which stains the basal ECM and is necessary for rosette development (Levin *et al.*, 2014). White arrowheads indicate rosettes. Scale bar, 10 μm. (D') The causative mutation in the mutant Couscous is a predicted glycosyltransferase that affects ECM glycosylation patterns and is necessary for proper rosette development (Wetzel *et al.*, 2018), while direct interruption of the Hippo signaling pathway causes larger colonies to form, likely due to increased ECM secretion (Combredet *et al.*, 2025). Scale bars, 20 μm. (D'') Solo is unable to form either chain or rosette colonies (Levin *et al.*, 2014), although the causative mutation is unknown.

Chapter 2

Septins regulate cytokinesis and multicellular development in the closest living relatives of animals

The results presented here were published as part of the following paper:

Carver, M, and King, N (2026). Septins regulate cytokinesis and multicellular development in the closest living relatives of animals. *bioRxiv*, 2026.04.05.716596 (also in review at *Molecular Biology of the Cell*)

Files S1-S5 and Videos S1-S5 are available in the bioRxiv preprint online version.

Abstract

Septins are cytoskeletal proteins that regulate cytokinesis in fungi and animals, yet their functions in choanoflagellates — the closest living relatives of animals — have remained unknown. *Salpingoeca rosetta,* a choanoflagellate that switches between unicellular and multicellular forms, encodes four septins closely related to animal and fungal septins. CRISPR/Cas9-mediated disruption of *S. rosetta* septins revealed that a subset regulate cell size in cultures containing single cells and linear chain colonies, with two mutants exhibiting an elevated frequency of oversized cells and one exhibiting smaller cells. Upon rosette induction, which produces spherical, shear-resistant colonies whose cells attach to a shared extracellular matrix, three of the four septins were found to regulate rosette development, while two also regulated rosette structural integrity. Characterization of *Sros_septA*, which showed the strongest phenotype, revealed a role in cytokinesis: mutant cells exhibited late-stage cytokinesis failure, resulting in enlarged, multinucleated cells. Cytokinesis failure rate increased in uninduced *Sros_septA* mutant cells and was further elevated upon rosette induction, suggesting that the multicellular context places heightened demands on the septin cytoskeleton. Endogenously tagged *Sros*_SeptA dynamically redistributed from the basal pole in interphase cells to the cleavage furrow and nascent intercellular bridge during cell division. These findings identify septins as regulators of cytokinesis and multicellular development in *S. rosetta* and offer a framework for exploring how cell division regulation contributed to the emergence of animal multicellularity.

Introduction

Septins, cytoskeletal proteins that regulate cytokinesis in fungi and animals (Hartwell *et al.*, 1974; Neufeld and Rubin, 1994), have been hypothesized to contribute to multicellular development in choanoflagellates, the closest living relatives of animals (Fairclough *et al.*, 2013). Although septins are found across eukaryotic diversity (Momany *et al.*, 2001; Kinoshita, 2003; Shuman and Momany, 2022; Delic *et al.*, 2024), they have been studied primarily in bilaterian animals and yeast. There, septins assemble into hetero-oligomeric filaments and higher-order structures that scaffold diverse factors at sites of dynamic membrane curvature (McMurray *et al.*, 2011). For example, septins localize to the cleavage furrow and regulate furrow ingression, intercellular bridge formation, and abscission (Kinoshita *et al.*, 2002; Surka *et al.*, 2002; Estey *et al.*, 2010; Founounou *et al.*, 2013; Karasmanis *et al.*, 2019; Hümpfer *et al.*, 2025).

Due to their phylogenetic position, choanoflagellates promise to provide insights into the ancestry of animal septins (King *et al.*, 2003, 2008; Fairclough *et al.*, 2013; Richter *et al.*, 2018). Choanoflagellates are aquatic microbial eukaryotes with a collar complex comprising an apical flagellum surrounded by microvilli (Dayel and King, 2014; Leadbeater, 2015). Under standard growth conditions, the model choanoflagellate *Salpingoeca rosetta* forms a mixture of single-celled "slow swimmers" and "chain" colonies in which cells are connected through fine intercellular bridges (Dayel *et al.*, 2011). In response to environmental cues, including bacterial sulfonolipids (Alegado *et al.*, 2012; Woznica *et al.*, 2016) and algal polysaccharides (Perotti *et al.*, 2025), *S. rosetta* instead develops into spherical "rosette" colonies in which the component cells are strongly attached through a combination of intercellular bridges, filopodia, and a shared extracellular matrix (ECM) (Dayel *et al.*, 2011; Levin *et al.*, 2014; Larson *et al.*, 2020). Experimental control of *S. rosetta* multicellularity is one of its strengths as a model for animal origins (Booth and King, 2022).

An earlier study found that *S. rosetta* encodes four septins (renamed *Sros_septA*, *Sros_sept6*, *Sros_septB*, and *Sros_sept9* in this study; Figure 2.1A), and reported that their expression was upregulated in multicellular forms (Fairclough *et al.*, 2013), although analyses included here differ on this point. Subsequent work using transient expression of two fluorescently tagged *S. rosetta* septins found that they localized to the basal pole of single cells and cells in rosettes (Booth *et al.*, 2018). However, septin function in choanoflagellates remained unclear.

Here, we set out to understand septin function in *S. rosetta*. We find that *Sros_septA*, *Sros_sept6*, and *Sros*_sept9 regulate cell size in opposing directions (*Sros_septA* and *Sros_sept6* losses increase cell size; *Sros_sept9* loss decreases it) and all three are required for proper rosette assembly, while *Sros_septA* and *Sros_sept6* additionally regulate rosette integrity. Further characterization of *Sros_septA* revealed a role in cytokinesis, with associated cell size and division defects that become more pronounced during rosette development. Consistent with its role as a regulator of cytokinesis, *Sros*_SeptA localization is dynamic throughout the cell cycle, localizing to the basal pole in interphase cells and to the cleavage furrow and nascent intercellular bridge during cytokinesis. Together, these findings suggest a role for septins at the interface of cytokinesis regulation and the evolution of animal multicellularity.

Results

S. rosetta septins are closely related to animal and fungal septins and are predicted to assemble into hexamers

Choanoflagellate genomes and transcriptomes published after the 2013 study of *S. rosetta* septins (del Campo and Ruiz-Trillo, 2013; Richter *et al.*, 2018; Brunet *et al.*, 2019; López-Escardó *et al.*, 2019; Hake *et al.*, 2024) prompted us to construct an updated phylogeny of septins using protein sequences from diverse choanoflagellates and other eukaryotes, including early-branching animals and fungi. Consistent with Fairclough *et al.* (2013), *Sros*_Sept9 was recovered as sister to animal SEPT9 sequences (Figure 2.1B and 2.S1A), and *Sros*_Sept6 fell within an unresolved polytomy that included the animal SEPT6 clade, septins from other close animal relatives, and the *Caenorhabditis elegans* septin *UNC-61*. The two remaining *S. rosetta* septins – previously called Septin2 and Septin7 – nested within the broader animal SEPT2/SEPT7 radiation (Kinoshita, 2003) but could not be resolved relative to one another or the animal SEPT7 group, forming a three-way polytomy. To avoid implying specific orthology that is not supported by our current phylogenetic analysis, we renamed *S. rosetta* Septin2 to *Sros*_SeptA and Septin7 to *Sros*_SeptB. Furthermore, each of the four *S. rosetta* septins cluster within clades that include septins from across choanoflagellate diversity, indicating broad conservation of these septin families (Figure 2.1C).

To investigate whether *S. rosetta* septins can assemble into hexameric structures similar to those found in animals and fungi (Sirajuddin *et al.*, 2007; Bertin *et al.*, 2008), we predicted their interactions using AlphaFold-3 (Abramson *et al.*, 2024). *Sros*_SeptA, *Sros*_Sept6, and *Sros*_SeptB were predicted to form a hexamer similar to the reported hexamers from humans (Figure 2.1D and 2.S1B; Mendonça *et al.*, 2021) and other opisthokonts. The AlphaFold-3 analysis placed *Sros*_SeptA in the position typically occupied by animal SEPT7, while *Sros*_SeptB was placed in the position typically occupied by animal SEPT2. These data are consistent with conservation in *S. rosetta* of the hexameric septin assembly found in animals and yeast. Currently, there is no published structure of the SEPT9-containing septin octamer, although the subunit arrangement has been inferred experimentally (Kim *et al.*, 2011). Furthermore, inclusion of SEPT9 in AlphaFold-3 predictions of human septin interactions did not recapitulate this inferred octameric architecture. Therefore, comparisons of hexameric structures were used for our analyses.

Multiple septins regulate cell size and rosette development

The first analyses of *S. rosetta* septins suggested that septin gene transcription was elevated in colonial cells (rosettes and chains; Figure 2.2A) relative to solitary cells (Fairclough *et al.*, 2013). Because of subsequent improvements to cell state regulation protocols for *S. rosetta*, we reanalyzed septin transcription using a recently published RNA-seq dataset (Leon *et al.*, 2025). In this dataset, four populations of cells were compared: (1) slow swimmers and chains, which naturally co-occur under standard growth conditions, (2) rosettes, (3) cultures enriched for single-celled fast swimmers, and (4) thecates, a single-celled sedentary cell state. Transcription of all four septins was reduced in thecate cells relative to slow swimmers and chains, and *Sros_septB* was additionally downregulated in fast swimmers (Figure 2.S2A). However,

transcription of *Sros_septA*, *Sros_sept6*, and *Sros_sept9* in slow swimmers and chains was comparable to that in both rosette cultures and fast swimmer cultures. Together, these data indicate that overall septin expression is not specifically upregulated in colonial cell types.

To investigate septin function in *S. rosetta*, we introduced a premature stop codon near the 5' end of each septin gene (Figures 2.1A and 2.S2B) using CRISPR/Cas9-mediated genome editing. The resulting mutants – *Sros_septA*$^{1\text{-}50}$, *Sros_septA*$^{1\text{-}116}$, *Sros_septB*$^{1\text{-}17}$, *Sros_sept6*$^{1\text{-}39}$, and *Sros_sept9*$^{1\text{-}63}$ – were named based on the number of N-terminal amino acids remaining after each truncation. Because *Sros_septA*$^{1\text{-}50}$ consistently exhibited more severe phenotypes than *Sros_septA*$^{1\text{-}116}$ across all assays, *Sros_septA*$^{1\text{-}50}$ is shown as the representative *septA* allele in Figures 2.2–4; *Sros_septA*$^{1\text{-}116}$ images and quantification are provided in Figure 2.S2D and included in most summary graphs. *Sros_septA*$^{1\text{-}50}$ and *Sros_sept6*$^{1\text{-}39}$ each exhibited a slight proliferation defect during log phase (Figure 2.S2C), while other septin mutants (including the other *Sros_septA* allele, *Sros_septA*$^{1\text{-}116}$) matched the proliferation dynamics of wild-type cells.

We next checked whether septin loss altered the morphology of *S. rosetta* slow swimmers and chains (Figure 2.2A). Cultures of all five septin mutants contained mixtures of single cells and chains that resembled those of wild-type cultures (Figure 2.2B-F, Figure 2.S2D). However, *Sros_septA*$^{1\text{-}50}$, *Sros_septA*$^{1\text{-}116}$, and *Sros_sept6*$^{1\text{-}39}$ had a small increase in the frequency of oversized cells relative to wild-type (Figure 2.2C; Figure 2.S2D and 2.S2F), which increased mean cell size by 1.25-fold, 1.19-fold, and 1.13-fold in *Sros_septA*$^{1\text{-}50}$, *Sros_septA*$^{1\text{-}116}$, and *Sros_sept6*$^{1\text{-}39}$, respectively (Figure 2.2G and Table S2). In contrast, mean cell size decreased by 0.90-fold in *Sros_sept9*$^{1\text{-}63}$ and was not significantly different in *Sros_septB*$^{1\text{-}17}$.

Rosette development in *S. rosetta* can be induced by treatment with sulfonolipids called Rosette Inducing Factors that are released in outer membrane vesicles (RIF-OMVs) from the bacterium *Algoriphagus machipongonensis* (Fairclough *et al.*, 2010; Woznica *et al.*, 2016). After treatment with RIF-OMVs, *Sros_septA*$^{1\text{-}50}$, *Sros_septA*$^{1\text{-}116}$, *Sros_sept6*$^{1\text{-}39}$, and *Sros_sept9*$^{1\text{-}63}$ cultures exhibited morphological defects (Figure 2.2C', D', and F', and Figure 2.S2D), with some rosettes having heterogeneous cell sizes and disrupted organization relative to wild-type, as well as an increased number of non-rosette single cells. As a proxy measure of rosette assembly, we quantified the mean areas of individuals (single cells, doublets, triplets, or rosettes) after RIF-OMV induction and found that the mean individual area was significantly reduced across all morphological classes in *Sros_septA*$^{1\text{-}50}$, *Sros_septA*$^{1\text{-}116}$, *Sros_sept6*$^{1\text{-}39}$, and *Sros_sept9*$^{1\text{-}63}$ cultures, indicating a reduction in the sizes of rosettes (Figure 2.2H and 2.S2G; Table S3). In contrast, RIF-OMV-treated *Sros_septB*$^{1\text{-}17}$ showed no significant size reduction and formed rosettes that resembled wild-type (Figure 2.2H and 2.2E'; Table S3).

Wild-type rosettes exhibit robust structural integrity and resistance to shear (Levin *et al.*, 2014). To assess whether septins affect rosette integrity, we vortexed wild-type and mutant cultures after rosette induction and quantified the projected area of the resulting individuals (Wetzel *et al.*, 2018; Xu *et al.*, 2022). In wild-type cultures, cells in rosettes remained attached; vortexing caused no significant reduction in mean projected individual area (Figure 2.2B'' and H; Table S4). Similarly, the mean projected area of individuals in *Sros_septB*$^{1\text{-}17}$ and *Sros_sept9*$^{1\text{-}63}$ cultures induced with RIF-OMVs did not significantly change after shear (Figure 2.2E'', 2.2F'' and 2.2H; Table S4). In contrast, *Sros_septA*$^{1\text{-}50}$, *Sros_septA*$^{1\text{-}116}$, and *Sros_sept6*$^{1\text{-}39}$ cultures

experienced significant disassembly (Figure 2.2C'' and D''; Figure 2.S2G). Because ECM production is important for proper rosette development, we hypothesized that septin mutants with compromised rosette integrity might exhibit ECM defects. However, staining of *Sros_septA*$^{1\text{-}50}$ rosettes with two markers of ECM, the lectin Jacalin (Figure 2.S3A) and an antibody to the ECM protein Rosetteless (Figure 2.S3A') (Levin *et al.*, 2014; Wetzel *et al.*, 2018), revealed that ECM levels were qualitatively similar to those in wild-type rosettes. This suggests that the loss of rosette integrity does not stem from an obvious loss of ECM secretion, although these data do not rule out subtler defects in ECM composition and organization.

Rosette induction in Sros_septA mutants results in increased cell size and cytokinesis defects

To better understand the connection between septin function and rosette development, we focused the remainder of our analyses on the *Sros_septA* mutants, which exhibited the strongest defects in cell size regulation and rosette development. We first asked whether cell size differed in *Sros_septA* mutants before and after rosette induction. Because the projected area of each cell cannot be easily measured in rosettes, we instead used cell segmentation to quantify cell volume (Figure 2.3A and 2.S3B). In wild-type cultures, untreated (i.e. slow swimmer and chain) and RIF-OMV-treated (i.e. rosette) conditions did not significantly differ in mean cell volume (Figure 2.3B; Table S5). In contrast, RIF-OMV treatment of *Sros_septA*$^{1\text{-}50}$ led to a 3.5-fold increase in mean cell volume over untreated *Sros_septA*$^{1\text{-}50}$ cells, while *Sros_septA*$^{1\text{-}116}$ cell volume increased by more than 1.5-fold (Table S5). Whether this volume increase is selective for cells incorporated into rosettes, or also occurs in the isolated single cells present in RIF-OMV-treated cultures, was not directly assessed in this experiment. This increase indicates a heightened importance of *Sros_septA* for regulating cell volume during rosette development.

Increased cell size in *S. cerevisiae* and *D. melanogaster* septin mutants is often a consequence of cytokinesis defects (Hartwell *et al.*, 1973; Neufeld and Rubin, 1994). Therefore, we next examined cytokinesis in *Sros_septA*$^{1\text{-}50}$ mutants. In wild-type *S. rosetta* cells, mitosis occurs along the apical–basal axis, with daughter cells either completing abscission or remaining attached by a narrow intercellular bridge, although the relative frequency of these outcomes has not been characterized (Figure 2.S3C and 2.S3D, Video S1; (Dayel *et al.*, 2011; Fairclough *et al.*, 2013)). In *Sros_septA*$^{1\text{-}50}$, cells that had undergone cleavage furrow ingression and appeared to have separated into daughter cells frequently fused back together, indicating a defect in a late stage of cytokinesis (Figure 2.3C, Video S2). In all observed failure events, furrow ingression proceeded to this apparent separation step, consistent with a specific requirement for *Sros*_SeptA during late cytokinesis rather than during earlier stages of furrow ingression. We also noted that in some *Sros_septA*$^{1\text{–}50}$ divisions, the cleavage plane appeared misaligned with the apical–basal cell axis, raising the possibility of a spindle positioning defect; whether this contributes to cytokinesis failure will require further investigation (Videos S2, S3). To investigate the fate of the nucleus during failed cytokinesis events in *Sros_septA*$^{1\text{-}50}$, we generated *Sros_septA*$^{1\text{-}50}$ cells that expressed histone H2B fused to mCherry (*Sros_septA*$^{1\text{-}50}$; *h2b-mCherry*) as a marker of nuclei. In these cells, the nuclei divided normally as the cell attempted cytokinesis and remained distinct following cytokinesis failure, resulting in large, multinucleated cells (Figure 2.S3E, Video S3).

Consistent with the *Sros_septA*$^{1\text{-}50}$ cell volume phenotype, the rate of cytokinesis failure in *Sros_septA*$^{1\text{-}50}$ was elevated in uninduced conditions and increased further – more than doubling – upon rosette induction during the first ten hours following treatment. In contrast, cytokinesis failure rates in wild-type cells were low and not significantly affected by rosette induction (Figure 2.3D; Table S6). Together, these data suggest that *Sros_septA* is more important for completion of cytokinesis in rosette cells than in uninduced cells.

Dynamic localization of Sros_SeptA during cytokinesis

To visualize *Sros*_SeptA *in vivo*, we adapted a recently published CRISPR-based gene editing strategy (Combredet *et al.*, 2025) to allow endogenous tagging of *S. rosetta* proteins with fluorescent proteins (Materials and Methods). Using this approach, we tagged the C-terminus of *Sros*_SeptA with mStayGold, a photobleach-resistant monomeric fluorescent protein (Ivorra-Molla *et al.*, 2024; Figure 2.4A). The monomeric form was used to minimize potential aggregation or multimerization artifacts. In addition, we tagged *Sros*_SeptA with an ALFA tag, a short epitope that can be detected using a fluorescently labeled nanobody (Götzke *et al.*, 2019). Both *Sros*_SeptA-mStayGold (SeptA-mSG) and *Sros*_SeptA-ALFA were detected primarily at the basal poles of non-dividing single cells, cells in chains, and cells in rosettes, with diffuse signal observed throughout the remainder of the cytoplasm (Figure 2.4B; Figure 2.S4A and B). These observations were consistent with prior observations of transiently-expressed *Sros*_SeptA-mWasabi (Booth *et al.*, 2018).

To assess whether the mStayGold tag affected *Sros*_SeptA function, we examined cell size and rosette integrity in *Sros_septA-mSG* and *Sros_septA-ALFA* cells. Neither strain exhibited the cell size defect observed in *Sros_septA*$^{1\text{-}50}$ cells following induction with RIF-OMVs (Figure 2.S4D and S4E). However, rosette integrity in *Sros_septA-mSG* and *Sros_septA-ALFA* cells was compromised relative to wild-type cells (Figure 2.S4F), indicating that the rosette development phenotype is separable from the cell size defect in tagged *Sros_septA* strains.

Because *Sros_septA-mSG* cells did not exhibit a mutant cell size phenotype, we used this strain to analyze *Sros*_SeptA dynamics during cell division. *Sros*_SeptA-mSG in dividing cells accumulated in a ring at the cleavage furrow during furrow ingression and, in contrast to interphase cells, did not appear to be enriched at the basal pole (Figure 2.4C; Figure 2.S4H; Video S4 and S5). As cytokinesis progressed, the *Sros*_SeptA-mSG ring constricted until it was largely restricted to the nascent intercellular bridge connecting the daughter cells, a pattern also detected by immunofluorescence in *Sros_septA-ALFA* cells (Figure 2.S4C). We observed no clear differences in septin localization or septin ring constriction when comparing single cells and rosettes. Together, these observations suggest that *Sros*_SeptA localization is dynamic across the cell cycle in single cells and rosettes (Figure 2.4D).

Discussion

Despite extensive research on septin function in fungi and bilaterian animals (Spiliotis and McMurray, 2020), septin function in non-bilaterians and close relatives of animals has been largely unexplored (Fairclough *et al.*, 2013; Booth *et al.*, 2018). Additionally, the role that cell division regulators might have played in the emergence of multicellularity in animals remains an

open question (Arakaki *et al.*, 2017; Brunet and King, 2017; Chaigne and Brunet, 2022). By examining septin function in *S. rosetta*, a choanoflagellate in which multicellular development can be experimentally controlled, this study helps address both gaps. Here, we identify a role for the septin cytoskeleton in regulating cell size and cytokinesis and show that this requirement is heightened during rosette development (Figure 2.4E). Specifically, disruption of *Sros_septA* in rosette-induced cells results in increased cell size and an elevated rate of cytokinesis failure relative to uninduced cells, suggesting that the multicellular context influences septin function in *S. rosetta*.

One possible explanation is that ECM attachment — beginning at the first division and persisting throughout rosette morphogenesis (Larson *et al.*, 2020) — introduces mechanical constraints that place additional demands on the septin cytoskeleton during cytokinesis, for example by tethering dividing cells to a shared ECM that resists the membrane remodeling required for cell division. This raises the possibility that ECM elaboration, by physically constraining dividing cells within a shared matrix, imposed new demands on cytokinetic completion, linking the evolution of cell adhesion to the evolution of cell division regulation. Alternatively, the phenotype may reflect biochemical responses to the inducing signal itself, rather than the mechanical constraints imposed by rosette architecture. A third possibility is that septins are differentially regulated in rosettes compared with uninduced cells. However, although *Sros*_SeptA dynamically redistributes throughout the cell cycle, we do not find any obvious differences in *Sros*_SeptA localization or transcription levels between single cells and rosettes.

We also find that *Sros_septA*, *Sros_sept6*, and *Sros_sept9* regulate rosette assembly in *S. rosetta* while *Sros_septA* and *Sros_sept6* also regulate rosette integrity, raising the possibility that septins directly regulate multicellular development (Figure 2.4E). While changes in cell size may secondarily affect rosette assembly or integrity, our finding that endogenously tagging *Sros_septA* disrupts rosette development without altering cell size suggests that septins may also act through cell size-independent mechanisms. For example, septins may help to scaffold factors at the basal pole to promote cell-ECM interaction or may influence the positioning or stability of intercellular bridges that physically connect cells within rosettes. The absence of a detectable phenotype in *Sros_septB*$^{1\text{-}17}$, and the dispensability of *Sros_sept9* for rosette integrity, may reflect incomplete loss-of-function alleles, functional redundancy, or roles for these septins that are distinct from those of SeptA and Sept6 — questions that future work can address. Together, these findings show that the septin cytoskeleton regulates cytokinesis and multicellular development in *S. rosetta*. More broadly, our results suggest that septins may help support cytokinesis under the physical and developmental demands of multicellular organization, offering a framework for exploring how cell division regulation intersected with the evolution of animal multicellularity.

Acknowledgments

We thank the following people for insights and contributions that helped advance this work: Maxwell Coyle, Juliette Mathieu, and Agathe Chaigne provided valuable feedback on drafts of the manuscript. Alain Garcia De Las Bayonas, Maxwell Coyle, Flora Rutaganira, Deepak Krishnamurthy, Samed Delic, Masayuki Onishi, Agathe Chaigne, and Ben Larson provided helpful feedback and suggestions for experiments. Samed Delic provided advice and helpful

discussion on septin phylogenetics. Jacob Steenwyk provided advice and script construction for phylogenetic analysis. David Booth and Laura Wetzel provided valuable insights into previous work on choanoflagellate septins and relevant rosette-defective *S. rosetta* mutants. Stefany Gonzales aided with molecular cloning and choanoflagellate culture. Kevin Rose provided insights and suggestions for septin structural modeling. Maria Nguyen and Flora Rutaganira provided RIF-OMV cultures used throughout this work as well as guidance and equipment/reagent use for CRISPR/Cas9-mediated endogenous C-terminal fluorescent tagging in *S. rosetta*. M.D.C. was supported by an NIH Molecular Basis of Cell Function T32 Training Grant (5T32GM007232). An Investigator Award from the Howard Hughes Medical Institute supports research in the King Lab. This work used the UC Berkeley DNA Sequencing Facility (Molecular and Cell Biology Department).

Author Contributions

Michael D. Carver, Conceived and designed the experiments, Performed the experiments, Analyzed the data, Prepared the digital images, and Drafted the article | Nicole King, Conceived the experiments, Contributed methodology, Acquired funding, Supervised the work, and Drafted the article.

Materials and Methods

BLAST searches for septin genes

To re-investigate the presence of septin genes across opisthokonts, we used human septin proteins representing the four major animal septin groups as BLASTP queries: SEPT2 (NP_004395.1), SEPT6 (NP_006138.1), SEPT7 (NP_001779.2), and SEPT9 (NP_006631.1). We searched for putative septins in 18 animals (eight bilaterians, four cnidarians, one placozoan, two ctenophores, and three poriferans), eight choanoflagellates, five additional holozoan relatives (filastereans, corallochytreans, and ichthyosporeans), two early-branching holomycotans, and seven fungi (File S1). Additionally, we included septins recently reported from nine non-opisthokont species (Delic *et al.*, 2024). Species were selected to (1) sample diverse choanoflagellates (Richter *et al.*, 2018), (2) increase representation of close animal relatives and early-diverging animals and fungi, and (3) include established model organisms (e.g. *D. melanogaster*, *S. cerevisiae*).

Searches were performed against the EukProt database (Richter *et al.*, 2022), a curated collection of predicted eukaryotic proteomes derived from genome and transcriptome assemblies, using BLASTP v2.13.0 with an E-value cutoff of 1×10^{-5}. For *Hydra vulgaris*, *Acropora digitifera*, and *Magnaporthe oryzae*, which are not hosted on EukProt, searches were performed using the NCBI nonredundant protein database (Sayers *et al.*, 2023). Candidate septins were defined as proteins containing the conserved septin GTP-binding domain (Pfam accession PF00735), identified using InterProScan (Jones *et al.*, 2014), which detects Pfam domains through Hidden Markov Model-based searches performed with HMMER. For bilaterian taxa, where septin family membership has been relatively well described (Kinoshita, 2003; Shuman and Momany, 2022), only the top septin hit from each of the four BLAST searches using human septin queries was included in the phylogeny for simplicity, with the exception of *D. melanogaster* (File S1). For non-bilaterian animals and other taxa, all recovered septin-domain proteins were included. Additionally, the top putative septin BLAST hit for all non-bilaterians was used as a query in a second BLAST search against the same proteome to identify additional paralogs. Iterative searches continued until no additional septin-domain proteins were recovered. Using this approach, a set of 201 putative septin sequences was recovered (File S1).

To further refine the dataset, sequences were filtered based on domain confidence, protein length, and domain architecture (File S1). All detected septin domain matches met the E-value cutoff of 1×10^{-5} (InterProScan), so we next turned to protein length. Septin proteins are typically ~30 – 65 kDa (Mostowy and Cossart, 2012), or approximately 300 – 600 amino acids, although N-terminal extensions exist in the SEPT9-family (Kim *et al.*, 2011). We therefore excluded candidate protein sequences below 200 amino acids and above 1000 amino acids, removing eight sequences. The remaining sequences were manually inspected to confirm the absence of domains inconsistent with canonical septins (e.g., DNA-binding or kinase domains). One fungal sequence containing a zinc finger DNA-binding domain was removed. The final dataset comprised 192 septin sequences (File S1) and was used for our phylogenetic analysis (Figure 2.S1A).

Phylogenetic trees

To infer maximum-likelihood phylogenies of septin genes (Figure 2.1C; Figure 2.S1A), we aligned protein sequences using MAFFT v7 with the L-INS-i algorithm set to default parameters,

trimmed with ClipKIT v1.3.0 (Steenwyk *et al.*, 2025) using the *smart-gap* mode, and analyzed using IQ-TREE v3.0.1 (Wong *et al.*, 2025). Ten independent maximum-likelihood searches were performed using IQ-TREE under the best-fitting substitution model (Q.PFAM+R8), each initiated from different random starting seeds. Branch support was estimated using ultrafast bootstrap approximation (UFBoot) with 1,000 replicates, and the tree with the highest log-likelihood score was selected for downstream analysis. Branches with bootstrap support below 80% were then collapsed prior to visualization. Trees were visualized using the Interactive Tree of Life (iTOL) web server (Letunic and Bork, 2021) and rooted using non-opisthokont septins as an outgroup (Delic *et al.*, 2024). Sequence labels in Figure 2.S1A correspond to the species name followed by the EukProt protein identifier, the RefSeq accession, or the identifiers for non-opisthokont septins used in Delic *et al.* (2024). The full amino acid sequences used in the phylogenetic analysis are provided in File S1. Sequence datasets, multiple sequence alignments, phylogenetic trees, and scripts used for phylogenetic analyses are available at Figshare (DOI: 10.6084/m9.figshare.31549345).

Septin structure predictions

To investigate potential interactions between *S. rosetta* septins, we used AlphaFold-3 (Abramson *et al.*, 2024) to model the oligomeric septin assembly shown in Figure 2.1D and Figure 2.S1B. As a point of comparison, we used the solved human septin hexamer cryo-EM structure (Mendonça *et al.*, 2021; PDB ID: 7M6J). This hexamer comprises SEPT2G (NM_004404; a truncated form lacking N- and C-terminal domains to prevent higher-order polymerization), SEPT6 (NM_145799), and SEPT7 (AAH93640.2). The structure excludes unresolved regions of each septin, notably at the N- and C-termini of SEPT6 and SEPT7 (detailed information available at PDB and in File S1). No high-resolution structure of the canonical human septin octamer has yet been published, although its subunit order has been experimentally inferred (Kim *et al.*, 2011), and inclusion of SEPT9 (NP_006631.1) in AlphaFold-3 predictions of the human octamer did not recapitulate this arrangement. Therefore, hexameric complexes were used for structural comparisons.

The *S. rosetta* septin hexamers in Figure 2.1D and Figure 2.S1B were predicted using AlphaFold-3 (Abramson *et al.*, 2024) with two copies each of *Sros*_SeptB (XP_004994452.1), *Sros*_Sept6 (XP_004992901.1), and *Sros*_SeptA (XP_004992637.1). The currently available RefSeq annotation for *Sros*_SeptB (XP_004994452.1) is truncated relative to the exon structure supported by RNA-seq read coverage from previous studies (Fairclough *et al.*, 2013; Leon *et al.*, 2025). We therefore derived a corrected gene structure using RNA-seq read coverage from Leon *et al.* (2025) for use throughout this study. The corrected CDS and protein sequences for *Sros_septB* are provided in File S2, and will be made available at GenBank under the accession number PZ120989 (pending final review). Because the PDB structure of the human septin hexamer omits unresolved residues at the N- and C-termini, we generated comparable *S. rosetta* protein sequences. To assign human–*S. rosetta* subunit pairs, we first modeled an untrimmed *S. rosetta* septin hexamer to define alignment pairs based on their relative positions within the hexamer (Figure 2.S1B). We then aligned each *S. rosetta* septin to its paired, trimmed human counterpart using NCBI BLASTP and removed residues corresponding to the unresolved N- and C-terminal regions (File S1). These trimmed sequences were subsequently used for structural prediction.

The cryo-electron microscopy structure of the human septin hexamer was solved with guanosine diphosphate (GDP) bound to SEPT2 and SEPT7 subunits and guanosine triphosphate (GTP) bound to SEPT6 subunits (Mendonça *et al.*, 2021). Accordingly, four GDP and two GTP molecules were included during AlphaFold-3 prediction of the *S. rosetta* hexamer. In the predicted model, GTP was associated with *Sros*_Sept6, whereas GDP was associated with *Sros*_SeptA and *Sros*_SeptB, consistent with subunit placement in the solved human structure.

Structures were visualized using UCSF ChimeraX v1.11.1 (Meng *et al.*, 2023) for Figure 2.1D and for confidence visualization of the predicted *S. rosetta* hexamer shown in Figure 2.S1B. Model confidence was assessed by Alphafold-3-generated predicted local distance difference test (pLDDT) scores and displayed as a continuous gradient (orange <50, yellow 50–70, cyan 70–90, blue >90), with 5-point transition zones on either side of cutoff values applied to smooth color boundaries. Global confidence metrics (pTM and ipTM) were obtained from AlphaFold-3.

S. rosetta cell type RNA sequencing and analysis

To analyze septin expression across the life history of *S. rosetta* (Figure 2.S2A), we used a recently published RNA-seq dataset (Leon *et al.*, 2025). This dataset utilized updated cell state regulation protocols to analyze transcription across four populations: (1) slow swimmers and chains, (2) rosettes, (3) fast swimmers, and (4) thecates. Briefly, RNA-seq was performed in triplicate for each condition, and reads were mapped to the *S. rosetta* transcriptome using kallisto (Bray *et al.*, 2016), with differential expression quantified using sleuth (Pimentel *et al.*, 2017). Using this dataset, we compared expression of the four septin genes in *S. rosetta* between populations of slow swimmers and chains relative to the other three analyzed cell states. Average TPM values are presented in Figure 2.S2A, and statistical comparisons are provided in the associated figure legend. Summary statistics are reported in Table S1. TPM values for individual replicates, fold-change, error metrics, and p- and q-values are given in File S3.

Preparation of Rosette Inducing Factors released in outer membrane vesicles

In experiments where rosette induction was required, we used Rosette Inducing Factors released in outer membrane vesicles (RIF-OMVs) from the bacterium *Algoriphagus machipongonensis* (Alegado *et al.*, 2013) (ATCC, BAA-2233). RIF-OMVs were provided as a gift from Florentine Rutaganira's lab (Stanford, CA) and were prepared as described in Woznica *et al.* (2016) with a few modifications. A single colony of *A. machipongonensis* was isolated from an agar plate made with Seawater Complete (SWC) prepared in artificial seawater (ASW) as described in Levin and King (2013). The colony was used to inoculate 5 mL SWC medium and the culture was grown at 30°C with shaking. After 48 h, the 5 mL culture was transferred to 1 L of 100% SWC in a 2.8 L Fernbach flask and the culture was grown for 72 h at 30°C with shaking. After separating conditioned media from *A. machipongonensis* cells by spinning at 4000 × g for 30 min in 50 mL Falcon tubes and filtering the supernatant twice through a 0.22 µm filter, RIF-OMVs were isolated by centrifugation of the supernatant for 3 h at 37,000 rpm and 4°C in a Beckman Ti45 rotor. The membrane pellet was resuspended in a buffer of 50 mM HEPES-KOH, pH 7.4 and the solution of RIF-OMVs was filtered through a sterile 0.22 µm polyethersulfone syringe filter, aliquoted into 100 µL aliquots, flash frozen and lyophilized. Lyophilized RIF-OMVs were stored at −80°C. To assess induction efficiency, RIF-OMVs were resuspended in 100 µL DMSO and tested on *SrEpac* cultures across a dilution series (1:500–1:10,000), with dilutions of 1:500 to 1:5000 inducing rosettes at >70%. For this study, RIF-OMVs were instead resuspended in 100

µL 10 mM HEPES-KOH, pH 7.5. A final dilution of 1:1000, selected from the previously defined effective range, consistently induced robust rosette formation and was used across all rosette-induction experiments. Carrier controls consisted of an equivalent volume of 10 mM HEPES-KOH, pH 7.5.

Choanoflagellate culturing

All experiments were performed using strains of *S. rosetta* co-cultured with *Echinicola pacifica* bacteria (strain designation: *SrEpac*) (Levin and King, 2013). Throughout this study, cells were grown in low nutrient media (LNM) (Booth and King, 2020). LNM consists of AK sea water (AKSW) complete (AKSWC; 5.0 g/L peptone, 3.0 g/L yeast extract, and 3.78 g/L glycerol dissolved in AK seawater) and AK cereal grass media (AKCGM3; 5 g/L cereal grass steeped in AKSW (Carolina Biological Supply Company, Cat. No. 132375)), both diluted to 1.5% by volume in AKSW and supplemented with nitrates, phosphates, trace elements, and vitamins as specified in Booth and King (2020). The AKSW formulation has been used to culture marine algae (Hallegraeff *et al.*, 2004) and dinoflagellates (Skelton *et al.*, 2009) and was adapted for culturing *S. rosetta* in Booth *et al.* (2018) because its lower calcium concentration (2.7 mM) was hypothesized to be more suitable for transfection protocols in comparison to the routinely used ASW made from Tropic Marin sea salts (Tropic Marin) (Levin and King, 2013). AKSW has since become one of the standard seawater options for *S. rosetta* husbandry.

A modified media formulation, comprised of AKSWC and AKCGM3 diluted each to 4% by volume in AKSW, termed high nutrient media (HNM), permits higher maximum *S. rosetta* cell densities during log-phase culture (Booth and King, 2020) and has been used in recent studies (Booth and King, 2020; Coyle *et al.*, 2023). We instead used LNM as it suppressed *E. pacifica* biofilm formation during routine passaging while supporting cell densities sufficient for experimental use.

Cultures were passaged every two days at a 1:500 dilution into fresh LNM and supplemented with 0.4% (v/v) of a 10 mg/mL *E. pacifica* suspension in ASW (hereafter referred to as "*E. pacifica* food pellet") to ensure a consistent supply of food bacteria. Cultures were maintained at 22°C and 60% humidity. For consistency, all experiments were performed using cells in the mid-log phase of growth, which in this media formulation occurs between 1×10^5 and 1×10^6 cells/mL.

S. rosetta cells grown to log-phase without RIF-OMVs produce cultures containing both single-celled slow swimmers and chain colonies of varying sizes (Figure 2.2A). When retention of chain colonies was not required, routine handling steps often disrupted chains, resulting in cultures composed primarily of single cells (Figure 2.3A; Figure 2.S3B). In contrast, growth in the presence of RIF-OMVs produced cultures containing cells at multiple stages of rosette development. Rosettes are arbitrarily defined as starting at the four-cell stage (Larson *et al.*, 2020), although they start as single cells and develop through one-, two-, and three-cell stages en route to becoming rosettes. Therefore, depending on the time since induction or the application of shear, cultures also contained different percentages of single cells, doublets, and triplets (Figure 2.S4G). Induction for at least 24 h resulted in robust rosette formation in wild-type cells, with colonies of approximately 8 – 12 cells predominating in the resulting cultures.

For long-term storage of wild-type and mutant *SrEpac* strains, cryopreservation was performed using 10% DMSO as described in King *et al.* (2009). Midway through this study, a glycerol-based cryopreservation method was reported and is now preferred (Chandra and Rutaganira, 2025); however, the DMSO protocol was used throughout our study for consistency across strains.

CRISPR guide RNA and repair template design

CRISPR guide RNA (gRNA) and repair templates were designed following previously established protocols (Booth and King, 2020). Candidate CRISPR RNA (crRNA) sequences for each of the four septin genes were identified using the EuPaGDT tool (http://grna.ctegd.uga.edu/) and the *S. rosetta* genome. Guide length was set to 15 nucleotides and an expanded PAM consensus sequence (HNNRRVGGH) was used. Coding sequences for genes of interest were obtained from the Ensembl Protists database (Yates *et al.*, 2022), which hosts the *S. rosetta* genome, with the exception of the corrected coding sequence for *Sros_septB* as described in "Septin structure prediction" (File S2). crRNA candidates were filtered for guides with one on-target hit (including making sure the guides do not span exon-exon boundaries), zero off-target hits (including against the genome of the co-cultured bacterium *E. pacifica*), lowest strength of the predicted secondary structure (assessed using the RNAfold web server: http://rna.tbi.univie.ac.at/cgi-bin/RNAWebSuite/RNAfold.cgi), and proximity to the 5' end of the coding sequence to maximize early gene disruption. crRNAs with the guide sequence of interest, as well as universal trans-activating CRISPR RNAs (tracrRNAs), were ordered from IDT (Integrated DNA Technologies) (File S4).

Repair templates were designed as single-stranded DNA oligonucleotides matching the sense strand of the crRNA and containing homology arms corresponding to 50 bp of genomic sequence flanking each side of the Cas9-induced double-stranded break at the CRISPR target site. For gene truncation experiments, the sequence 5'-TTTATTTAATTAAATAAA-3', a "termination cassette" encoding a stop codon in every frame, was included between the homology arms. To ALFA-tag (Götzke *et al.*, 2019) *Sros_septA,* a codon-optimized ALFA-tag sequence (5'-AGCCGCCTGGAGGAGGAGCTGCGCCGCCGCCTGACGGAG -3') was inserted between homology arms. A 5' AG and 3' G were included to restore the interrupted GAG (glutamic acid) codon at the cut site (pos. 1178 in the CDS sequence) (File S4). Along with the crRNA targeting our gene of interest, we co-edited our cells using previously published sequences for a crRNA and repair template designed to introduce a P56Q mutation in *rpl36a* (Booth and King, 2020), conferring cycloheximide resistance to enrich for genome-edited cells by selection. crRNA and repair oligo sequences are given in File S4.

Genome editing

Thirty-six hours prior to transfection, *S. rosetta* cells were inoculated into 120 mL of LNM at 8,000 cells/mL with 1 mL of *E. pacifica* food pellet added. This seeding density brought the culture to mid-log phase at the time of transfection. The inoculation period and bacterial food pellet addition were adjusted from previous protocols (Booth and King, 2020) to better match growth dynamics in LNM.

CRISPR/Cas9 nucleofection was performed according to the protocol outlined in Coyle *et al.* (2023), which adapted the original protocol reported in Booth and King (2020). Cultures were

co-transfected with Cas9 RNPs and repair oligonucleotides targeting (1) the gene of interest and (2) the *rpl36a* locus to confer cycloheximide resistance (see "CRISPR guide RNA and repair template design"). The nucleofection reactions were prepared as described in Coyle *et al.* (2023), mixed into Lonza SF buffer (Lonza, Cat. No. V4SC-2960), added to a 96-well nucleofection plate (Lonza, Cat. No. V4SC-2960), and pulsed with the program CM156 using a Lonza 4D-Nucleofector (Cat. No. AAF-1003B for the core unit and AAF-1003S for the 96-well unit). Pulsed cells were immediately recovered in recovery buffer (HEPES-KOH, pH 7.5; 0.9 M sorbitol; 8% [wt/vol] PEG 800) for 5 min, and then added to 2 mL LNM in a 6-well plate (Thermo Fisher Scientific, Cat. No. 140675) at 22°C and 60% humidity. After 30 min, 10 µL *E. pacifica* food pellet was added. Twenty-four hours later, 10 µl of 1 µg/mL cycloheximide (final concentration 5 ng/mL) was added to each well along with an additional 10 µl *E. pacifica* food pellet. Cycloheximide selection was carried out for four days. A negative control well of unedited cells (carried through the transfection experiment but without Cas9 RNPs or repair oligonucleotide) was used to confirm effective cycloheximide selection after the four-day selection period.

Following selection, cells were diluted to 100,000 cells/mL and clonally isolated using a WOLF® G2 Cell Sorter (WOLF; NanoCellect Biomedical) equipped with a WOLF Microfluidic Sorting Cartridge (Cat. No. SP0511). Cells were sorted into 96-well plates (Thermo Fisher Scientific, Cat. No. 167008) containing 200 µL LNM supplemented with 1 µL of *E. pacifica* food pellet per well. Sorting was performed using forward scatter as the trigger, with a threshold of 40,000 and detector voltage set to 150. These conditions consistently produced plates with cells in ~75% of the wells. For each independent population of edited cells, at least four 96-well plates were prepared. Sorted cells were allowed to proliferate for five days to reach workable cell density within wells.

To extract genomic DNA for genotyping analysis, 25 µl of culture from the same well position in up to four source plates (e.g., A1 from each plate) was pooled into the corresponding well of a new 96-well plate. Pooling was performed to reduce the number of sequencing reactions required for genotyping large numbers of cells. An equal volume of DNAzol direct (Molecular Research Center, Inc, Cat. No. DN131) was added to the pooled cultures to extract genomic DNA. This mixture was incubated at room temperature for 10 min and then stored at -20°C.

Genotyping PCRs were performed in 96-well plates (Brooks Life Sciences, Cat. No. 4ti-0770/c) using Q5 polymerase (NEB, Cat. No. M0491L) for 40 cycles. 2.5 µl of genomic DNA template was used in each 25 µl PCR reaction. PCR products were purified by magnetic bead cleanup and analyzed by Sanger sequencing (UC Berkeley DNA Sequencing Facility). Positive edits were detected in pooled genomic DNA samples by identifying overlapping sequencing reads beginning immediately downstream of the designed edit site. After a candidate positive pool was identified, the corresponding wells from the original 96-well plates were sequenced individually to identify the positive well, and the resulting strain was expanded for downstream experimentation and long-term storage.

Development of CRISPR/Cas9-mediated endogenous C-terminal fluorescent tagging in *S. rosetta*

To visualize *Sros*_SeptA in live cells, we adapted a recently published CRISPR/Cas9 gene truncation strategy (Combredet *et al.*, 2025) to enable endogenous fluorescent tagging in *S. rosetta*. Our approach enabled in-frame insertion of the coding sequence of mStayGold (Ivorra-Molla *et al.*, 2024), a bright and photobleach-resistant monomeric fluorophore, at the 3' end of the *Sros_septA* coding sequence to generate an endogenously tagged C-terminal fusion protein *Sros*_SeptA-mStayGold.

The Combredet *et al.* (2025) method uses a plasmid template (pEFL-pac-5' Act; Addgene ID pMS18; Cat. No. 225681) to PCR-amplify a repair template for use in CRISPR/Cas9 genome editing. In the published strategy, the repair template contains (1) a backbone-derived puromycin resistance cassette (pEFL-pac-5' Act), (2) a primer-derived termination cassette encoding a premature stop codon, and (3) primer-derived 5' and 3' homology arms corresponding to the genomic sequence flanking each side of the Cas9-induced double-stranded break at the CRISPR target site. Combredet *et al.* tested 50, 80, and 155 bp homology arms, all of which resulted in similar editing efficiency. Following CRISPR/Cas9-mediated double-strand break formation, the repair template is inserted at the target locus, resulting in gene truncation and enabling puromycin selection of edited cells.

We devised a similar strategy to tag *Sros*_SeptA at its C-terminus with a fluorescent protein. First, we identified the most 3'-adjacent CRISPR/Cas9 PAM site within the *Sros_septA* coding sequence. We then modified the pMS18 plasmid to encode: (1) the 59 bp region of the *Sros_septA* CDS downstream of the cut site ("*Sros_septA* 3' CDS recovery region"), (2) a glycine-serine flexible linker sequence (SGGSGGS) (Chen *et al.*, 2013), fused in frame, which had previously been used to link *Sros*_SeptA to an mWasabi fluorophore (Booth *et al.*, 2018), (3) an in-frame *mStayGold* coding sequence ending with a stop codon, and (4) the 3' UTR of *Sros_septA*, all positioned immediately upstream of the puromycin-resistance cassette. The *mStayGold* coding sequence, codon-optimized for *S. rosetta*, was generously provided by Jeffrey Colgren (Pawel Burkhardt lab, University of Bergen). The resulting plasmid is available at Addgene (Addgene ID NK812; Cat. No. 253995). We designed PCR primers to amplify the modified repair cassette (*Sros_septA* 3' CDS recovery region – 21 bp linker – *mStayGold* coding sequence – stop codon – puromycin resistance cassette) with 50 bp homology arms flanking the CRISPR/Cas9 target site in the *Sros_septA* coding sequence, generating a repair template size 2996 bp. Detailed information about the sequences described above is available in File S5.

To avoid possible recombination between two identical 50 bp sequences on the repair template – (1) the homology arm sequence of the 3' primer, designed to match the genomic region adjacent to the cut site, and (2) the 3' *Sros_septA* CDS recovery sequence encoded on the plasmid template – we introduced eight synonymous nucleotide substitutions into the plasmid-encoded CDS recovery region to reduce similarity between these sequences (File S5). All substitutions were placed at third codon positions such that the edited genomic allele encodes an unchanged *Sros*_SeptA amino acid sequence. The alternative codons were selected to match the original codon usage as closely as possible (File S5).

Following PCR amplification and cleanup of the 2996 bp repair template as outlined in Combredet *et al.* (2025), we recovered ~9 µg of repair template contained in 30 µL nuclease-free water. We then evaporated the 30 µL volume containing the repair template at 55°C on a heating block for 3 h until near dryness and resuspended the repair oligos directly in the final CRISPR reaction mixture (16 µL ice-cold "homebrew" nucleofection buffer (Nguyen *et al.*, 2026), 4 µL SpCas9 RNP, 1 µg pUC19 (Nature Technology, Cat. No. NTC-RP500) carrier plasmid, and 2 µL of primed *S. rosetta* cells. SpCas9 RNP and primed *S. rosetta* cells were prepared as in Booth and King (2020) with the modifications given in "Genome editing". The nucleofection reaction was then added to a 16-well Lonza nucleofection strip (Lonza, Cat. No. V4XP-3032) and pulsed with the program DG137 (Nguyen *et al.*, 2026) using a Lonza 4D-Nucleofector. Pulsed cells were immediately recovered in recovery buffer for 5 min and then added to 2 mL LNM in a 6-well plate. After 30 min, 10 µL *E. pacifica* food pellet was added. Twenty-four hours after nucleofection, 80 µg/mL puromycin was added to the culture and selection took place over five days. Healthy cells that recovered following puromycin selection were then screened for fluorescence on a Nikon Ti2 inverted microscope (Nikon Instruments) with a Yokogawa CSU-W1 spinning disk confocal unit and a Hamamatsu ORCA-Flash4.0 C14440-20UP CMOS camera (Hamamatsu Photonics) (hereafter, "Nikon Ti2 spinning disk confocal system"). Fluorescent cultures were then clonally isolated and genotyped by PCR and Sanger sequencing as described in "Genome editing" (primers listed in File S5).

Growth curves

Twenty-four hours before the start of the growth assay (Figure 2.S2C), cultures in log-phase were diluted to 10,000 cells/mL to standardize the growth conditions across starter cultures. On the day the growth curve plates were seeded, starter cultures were washed three times (2,400 × g for 5 min each) with ASW to remove bacteria on a Thermo Fisher Scientific ST16R swinging-bucket rotor centrifuge (hereafter, "swinging-bucket rotor centrifuge"), thereby standardizing nutrient conditions across cultures. Cells were then diluted to 5,000 cells/mL in LNM and supplemented with 267 µg/mL *E. pacifica* food pellet. 500 µL of culture was aliquoted into each well of a 24-well plate (Fisher Scientific, Cat. No. 09-761-146) and incubated at 22°C and 60% humidity. Plates were maintained in a covered plastic container with dampened paper towels and the lid loosely affixed to minimize evaporation while allowing gas exchange.

Every 12 h, starting at 0 h and continuing for 96 h, three wells per strain were fixed with 10 µL of 16% paraformaldehyde (Thermo Fisher Scientific, Cat. No. 50-980-487) and stored at 4°C. After all time points were collected, samples were vortexed, and 200 µL of each was added to a 96-well plate (Thermo Fisher Scientific, Cat. No. 167008). Samples were analyzed on an Attune CytPix Flow Cytometer equipped with an Attune CytKick Max Autosampler (Thermo Fisher Scientific) with the following settings: Mix Mode (aspirate and stir once per well); 150 µL acquisition volume at a flow rate of 200 µL/min; FSC detector voltage 150; SSC detector voltage 300; FSC threshold 20×10^3. Total cell counts were divided by the acquisition volume to calculate cell density (cells/mL).

Imaging slow swimmers, chains, and rosettes

To image *S. rosetta* wild-type and septin mutant cultures shown in Figure 2.2B–F", Figure 2.S2D, and Figure 2.S4D, cultures were grown for 36 h in six-well plates (Thermo Fisher Scientific, Cat. No. 140675) (3 mL per well) with or without RIF-OMVs. For RIF-OMV-induced

cultures subjected to shear, cultures were vortexed for 15 s at high-speed using a Vortex Genie 2 (Scientific Industries) in a 15 mL Falcon tube (Corning, Cat. No. 352196) before imaging.

For each strain and condition, 2 mL of culture was gently concentrated by low-speed centrifugation (600 × g for 5 min) using a swinging-bucket rotor centrifuge. To avoid disturbing the loose pellet, the supernatant was left in place and a 200 µL aliquot was gently aspirated directly from the pellet using a wide-bore 200 µL tip and transferred to a poly-D-lysine (Millipore Sigma, Cat. No. P6407) coated 8-well FluoroDish (World Precision Instruments, Cat. No. FD35-100). The gentle centrifugation and transfer preserved chain and rosette structures while concentrating cells for ease of imaging. Cells were allowed to settle for 10 min at 22°C before live imaging by differential interference contrast (DIC) microscopy on a Zeiss Axio Observer.Z1/7 Widefield microscope with a Hamamatsu Orca-Flash 4.0 LT CMOS Digital Camera (Hamamatsu Photonics) (hereafter, "Zeiss Axio Observer Widefield microscope") equipped with a Plan-Apochromat 20×/0.80 Ph 2 M27 objective with a 1.6× Optovar setting.

Imaging and quantifying cell area of slow swimmers and chain cells

To quantify the cell area of slow swimmers and chain cells (Figure 2.2G; Figure 2.S2E and 2.S2F), cultures were grown to mid-log phase and visually inspected prior to analysis to confirm that only slow swimmers and chains, and not smaller fast swimmer cells, were present. This was done to ensure cell size comparisons were consistent across strains. Cells were then vortexed at high speed for 5 s to separate doublets and chain colonies into single cells before analysis.

Cells were analyzed on an Attune CytPix Flow Cytometer, which captures brightfield images of recorded events in addition to standard flow cytometry data, using the following settings: 100 µL acquisition volume at a flow rate of 200 µL/min; FSC detector voltage 150; SSC detector voltage 300; FSC threshold 30×10^3; and 10,000 images captured total. The "Cells_Full_Resolution_v23" stock CytPix image processing model (available at Figshare, DOI: 10.6084/m9.figshare.31549345) was used to process images and determine the projected area of each cell. Only images containing a single cell were included in the final data set. When the model detected two or more cells in an image (fewer than 5% of images analyzed), those images were excluded (Figure 2.S2E).

Imaging and quantifying rosette assembly and integrity phenotypes

To quantify the projected area of individuals (single cells, doublets, triplets, and rosettes) in rosette-induced cultures with and without exposure to shear (Figure 2.2H), starter cultures in mid-log phase were split and used to seed duplicate 2 mL volumes in six-well plates. Cultures were then grown for 24 h in the presence of RIF-OMVs. To apply shear treatment, cultures were vortexed for 15 s at high speed in a 15 mL Falcon tube using a Vortex Genie 2. Vortexed cultures were allowed to rest for 10 min prior to subsequent preparation steps to minimize potential cell lysis. For each condition, 1 mL each of vortexed and unvortexed culture were gently transferred to a FluoroDish using a 1 mL pipette tip with the end trimmed off. Cells were allowed to settle for 10 min prior to staining.

LysoTracker Red DND-99 (Thermo Fisher Scientific, Cat. No. L7528) was added at a final dilution of 1:100 (overloaded to visualize the cell body) by removing 500 µL of culture from the FluoroDish and carefully adding 500 µL of a 1:50 LysoTracker solution diluted in ASW. Cells

were immediately imaged using DIC microscopy and epifluorescence on a Zeiss Axio Observer Widefield microscope equipped with a Plan-Apochromat 20×/0.80 Ph 2 M27 objective with a 1.6× Optovar setting. Epifluorescence images were acquired using a mCherry filter set. At least five fields of view were acquired per condition for each biological replicate. Fields of view were chosen through sequential non-overlapping stage translations; fields with insufficient cell density or poor staining were excluded.

Images were batch processed in FIJI (ImageJ) (Schindelin *et al.*, 2012) to ensure consistent analysis across samples. The epifluorescence channel of each image was converted to 8-bit and thresholded using the Otsu method (upper limit set to 150) to create a binary mask; the mask was inverted so that objects were black on a white background prior to particle analysis; segmented objects were analyzed with the "Analyze Particles" command to calculate the area of each individual; and a minimum size threshold of 10 pixels^2 was set to exclude small artifacts. Examples of DIC images, epifluorescence images, and masked images are given in Figure 2.S2G. The FIJI batch protocol is available at Figshare (DOI: 10.6084/m9.figshare.31549345).

Imaging and quantifying cell volume of slow swimmers, chains, and rosettes

To quantify the average cell volume of cells in rosettes in comparison with slow swimmer cells and cells in chains (Figure 2.3B), cultures were grown for 36 h in six-well plates (3 mL per well) with or without RIF-OMVs, respectively. 1 mL of each culture was added to a poly-D-lysine-coated FluoroDish and stained with LysoTracker Red DND-99 as in "Imaging and quantifying rosette assembly and integrity phenotypes." Cells were then immediately imaged using a Nikon Ti2 spinning disk confocal system equipped with an Apo TIRF 60×/1.49 NA oil immersion objective. Fluorescent images were acquired using 561 nm excitation with a mCherry emission filter. Three-dimensional imaging was performed with a 0.2 µm step size over ~90 optical sections (total depth ~18 µm). At least four fields of view were acquired per condition for each biological replicate. Fields of view were chosen through sequential non-overlapping stage translations; fields with insufficient cell density or poor staining were excluded.

Images were batch processed to quantify cell volume using a cell segmentation pipeline within Imaris x64 v10.2.0 (Jun 18, 2024 build 67164, Bitplane/Oxford Instruments) to ensure consistency across strains (example images before and after segmentation shown in Figure 2.S3B). To segment single cells and cells in rosettes, surfaces were generated from the raw, unprocessed three-dimensional images using the machine learning–based segmentation workflow option in Imaris by iterative manual annotation of foreground and background objects. To train the segmentation model, images of representative untreated and rosette-induced cells from each genotype (wild-type, *Sros_septA*$^{1\text{-}50}$, and *Sros_septA*$^{1\text{-}116}$) were combined into a composite training image. The final model was trained by annotating at least five cells from each genotype and treatment condition within this composite image. Surface generation was performed using the region growing segmentation method with an estimated object diameter of 1.5 µm and surface smoothing enabled (surface grain size = 0.216 µm). Following segmentation, objects were filtered to exclude surfaces with fewer than 10 voxels, volumes less than 20.0 µm³, and objects intersecting the image border in the XY plane (segmented example images given in Figure 2.3A). A batch protocol was created from these parameters and applied to images in all conditions, resulting in cell volume as an output. The training data and segmentation parameters used in Imaris are available at Figshare (DOI: 10.6084/m9.figshare.31549345).

Imaging and quantifying cytokinesis failure in slow swimmers and rosettes
For imaging (Figure 2.3C) and quantification (Figure 2.3D) of cytokinesis events, wild-type and *Sros_septA*$^{1\text{-}50}$ cells were diluted to 150,000 cells/mL and gently vortexed for 5 s on low speed on a Vortex Genie 2 to separate chains and doublets into single cells. 200 µL of each diluted culture with or without RIF-OMVs and supplemented with 2 µL *E. pacifica* food pellet was added to the center of a FluoroDish. Dishes were prepared by coating with poly-D-lysine, washing three times with ASW, and leaving the final wash in place for 30 min to generate a gently adhesive surface that minimized surface effects on cell division. To minimize evaporation while permitting oxygen exchange during time-lapse imaging, 1.5 mL of Anti-Evaporation Oil (Ibidi, Cat. No. 50051) was layered on top of the 200 µL culture, enough to cover the FluoroDish surface and with an oil level matching the height of the culture droplet. Cells were then allowed to settle for 10 min at 22 °C.

Cells were imaged using DIC time-lapse microscopy on a Zeiss Axio Observer Widefield microscope equipped with a Plan-Apochromat 20×/0.80 Ph2 M27 objective. For each experiment, a single field of view with a high density of cells was chosen. Images were collected at 30 s intervals for 10 h. A cytokinesis failure was defined as a cell division event followed by cell fusion at any point within 30 min after the initial event of cleavage furrow ingression could be detected. All division events across each time-lapse were recorded and included in quantification, except for divisions beginning within the last 30 min of the time-lapse as they could not be analyzed with the above parameters.

Imaging *Sros*_SeptA-mStayGold
To image *Sros*_SeptA-mStayGold slow swimmers, chains, and rosettes (Figure 2.4B), cultures were grown for 12 h in six-well plates (3 mL per well) with or without RIF-OMVs. This induction time was optimized to enrich for chains and rosettes at the four-cell stage for ease of imaging. 2 mL of each culture was first gently concentrated by low-speed centrifugation (600 × g for 5 min). To avoid disturbing the loose pellet, the supernatant was left in place and a 200 µL aliquot was gently aspirated directly from the pellet using a wide-bore 200 µL tip. The aspirated pellet was then transferred to a poly-D-lysine-coated 96-well plate to preserve chain and rosette structures. *Sros_septA-mStayGold* cultures were stained with Alexa Fluor 568-conjugated Jacalin (Vector Labs, Cat. No. L-1150; Thermo Fisher Scientific, Cat. No. A10238) at 1:200 and imaged immediately using a Nikon Ti2 spinning disk confocal system operating in a 2× super-resolution (SoRa) mode with a Plan Apo λ 100× oil immersion objective. Fluorescent images were collected using 488 nm excitation with a FITC emission filter (SeptA-mStayGold) and 561 nm excitation with a TRITC emission filter (Jacalin). Z-stacks were collected at 0.2 µm intervals and representative central optical sections are shown in Figure 2.4B.

For time-lapse imaging to visualize SeptA-mStayGold during cell division (Figure 2.4C and 2.S4H and Videos S4 and S5), *Sros_SeptA-mStayGold* cells were grown for 6 h in six-well plates (3 mL per well) with or without RIF-OMVs. This induction period was optimized to enrich for early rosette development for ease of time-lapse, three-dimensional imaging. Various lectins, including Jacalin and WGA, were tested to label dividing cells; however, lectins appeared to inhibit cell division and were therefore not used for time-lapse imaging. 2 mL of culture was

gently concentrated by low-speed centrifugation (600 × g for 5 min) with a swinging-bucket rotor centrifuge. A 200 µL aliquot was carefully collected from the resulting loose pellet using a wide-bore 200 µL pipette tip, transferred to a 96-well plate, and imaged using the same microscope system and excitation/filter set as above. Z-stacks were acquired at 0.2 µm intervals and time points were acquired at 30 s intervals. The three-dimensional time-lapse images were visualized and processed using Imaris x64 v10.2.0.

Immunostaining and imaging *Sros*_SeptA-ALFA

To visualize the cellular localization of SeptA-ALFA in interphase cells (Figure 2.S4B), 20 mL of culture was grown for 12 h with or without RIF-OMVs. Cells (13 mL) were collected by centrifugation (1000 × g for 5 min) in 15-mL Falcon tubes using a swinging-bucket rotor centrifuge and resuspended in LNM to a cell density of 5×10^6 cells/mL (~1 mL). Cells were fixed in suspension prior to plating: A 200 µL aliquot of each culture was pre-treated in an Eppendorf tube in 6% acetone in phosphate-buffered saline (PBS) at room temperature for 5 min followed by fixation in 4% PFA in PBS at room temperature for 10 min. Fixed cells were spun for 10 min at 800 × g with an Eppendorf 542R fixed-angle tabletop microcentrifuge and transferred to room temperature PEM (100 mM PIPES, pH 6.95; 2 mM EGTA; 1 mM $MgCl^2$). At this point, cells could be stored at 4 °C until immunostaining steps.

To prepare for immunostaining, cells in PEM were transferred to a poly-D-lysine–coated plate and centrifuged (600 × g for 5 min) with a swinging-bucket rotor centrifuge to adhere fixed cells. Cells were permeabilized with permeabilization buffer (1% [w/v] bovine serum albumin-fraction V; 0.3% [v/v] Triton X-100 in PEM) for 30 min. Cells were then incubated with 12.5 nM anti-ALFA nanobody conjugated to Alexa Fluor 657 (NanoTag Biotechnologies, Cat. No. N1502-AF647-L) and 25 ng/mL rat anti-Tubulin antibody conjugated to Alexa Fluor 488 (Abcam, Cat. No. Ab195883) for 1 h while rocking at 300 rpm on an Eppendorf MixMate (Eppendorf, Cat. No. 5353953449).

Chambers were then washed three times with PEM and imaged immediately using a Nikon Ti2 spinning disk confocal system equipped with a Plan Apo λ 100× oil immersion objective. Fluorescent images were collected using 488 nm excitation with a FITC emission filter (microtubules) and 647 nm excitation with a Cy5 emission filter (SeptA-ALFA). Z-stacks were acquired at 0.3 µm intervals. The three-dimensional fluorescent images were then visualized and processed using Imaris x64 v10.2.0.

To visualize SeptA-ALFA-positive intercellular bridges (Figure 2.S4C), 20 mL of uninduced culture was grown to early log-phase, which we found contained the highest amount of chain colonies. 13 mL of culture was gently added to a 15 mL Falcon tube and concentrated by low-speed centrifugation (600 × g for 5 min) with a swinging-bucket rotor centrifuge. To avoid disturbing the loose pellet, 10 mL of supernatant was removed and a 200 µL aliquot was then gently aspirated directly from the pellet using a wide-bore 200 µL tip. The aspirated pellet was then transferred to a poly-D-lysine-coated 96-well plate to preserve chain and intercellular bridge structures. One minute before fixation, 1 µg/mL FM-4-64FX dye (Thermo Fisher, Cat. No. F34653) was added to the cultures to label membranes. Cells were then fixed directly in the chamber using 6% acetone, 4% PFA, and 1:300 phalloidin conjugated to Alexa Fluor 488 (Life Technologies, Cat. No. A12379) in PBS at room temperature for 15 min in the dark. Acetone,

PFA, and phalloidin were added simultaneously as we noticed this combination, along with gentle culture handling, preserved a higher number of intercellular bridges in chain colonies compared with previously established fixation protocols (Booth *et al.*, 2018), potentially due to phalloidin stabilizing intercellular bridge structures, which often contained F-actin. Following fixation, wells were washed twice with PEM and then incubated in permeabilization buffer as above on a shaker at 300 rpm for 30 min. Cultures were then incubated with 12.5 nM anti-ALFA nanobody conjugated to Alexa Fluor 657 on a shaker at 300 rpm for 1 h. Cultures were washed three times with PEM and imaged immediately as above with the following changes: Z-stacks were acquired at 0.2 µm intervals, 488 nm excitation with a FITC emission filter was used to visualize phalloidin-labeled F-actin, and 488 nm excitation with a Cy5 emission filter was used to visualize FM4-64-labeled membrane. Maximum-intensity projections were generated from a total Z-depth of 1 µm.

Imaging the extracellular matrix of rosettes

To visualize Jacalin-positive ECM in wild-type and *Sros_septA*$^{1\text{-}50}$ (Figure 2.S3A), cultures were grown for 12 h in six-well plates (3 mL per well) with or without RIF-OMVs. 200 µL of culture was then added to poly-D-lysine–coated 96-well plates to allow cells to adhere, and fluorescein-conjugated Jacalin was added at a final dilution of 1:200 by removing 100 µL culture and adding 100 µL 1:100 fluorescein-conjugated Jacalin premixed in LNM. Cells were immediately imaged by DIC and epifluorescence microscopy using a Zeiss Axio Observer Widefield microscope equipped with a LD C-Apochromat 40×/1.1 W Korr UV VIS IR water-immersion objective with a 2.6× Optovar setting. Epifluorescence images were acquired using a GFP filter set. Z-stacks were collected at 1 µm step sizes. Maximum-intensity projections were generated from a total Z-depth of 5 µm for the fluorescence channel, and the corresponding central DIC plane was used for merged images.

To visualize Rosetteless-positive ECM in wild-type and *Sros_septA*$^{1\text{-}50}$ (Figure 2.S3A'), 20 mL cultures were grown to mid-log phase after 24 h of induction with RIF-OMVs. Rosetteless, a C-type lectin required for rosette formation in *S. rosetta*, has previously been shown to localize to rosette ECM (Levin *et al.*, 2014). Cells were concentrated, fixed, washed, and transferred to 96-well plates as described in the first section of "Immunostaining and imaging SeptA-ALFA." Cells were permeabilized with permeabilization buffer (1% [w/v] bovine serum albumin-fraction V; 0.3% [v/v] Triton X-100 in PEM) for 30 min and then stained with 1:200 rabbit anti-Rosetteless (Levin *et al.*, 2014) in blocking buffer (1% [w/v] bovine serum albumin-fraction in PEM). Cells were incubated with the primary antibody for 1 h while rocking at 300 rpm on an Eppendorf MixMate. The chamber was then gently washed three times with PEM and incubated with a final concentration of 2 µg/mL goat anti-rabbit secondary antibody conjugated to Alexa Fluor 568 (Thermo Fisher Scientific, Cat. No. A-11036) for 45 min while rocking at 300 rpm.

Following incubation with the secondary antibody, the chamber was washed three times with PEM and cells were imaged immediately using a Zeiss Axio Observer Widefield microscope equipped with a LD C-Apochromat 100×/1.46 Oil DIC (UV) M27 objective with a 1.6× Optovar setting. Epifluorescence images were acquired using a Cy3 filter set. Z-stacks were collected at 1 µm step sizes. Maximum-intensity projections were generated from a total Z-depth of 5 µm for the fluorescence channel, and the corresponding central DIC plane was used for merged images.

Phenotypic comparison of tagged *Sros_septA* strains

To compare phenotypes of wild-type, *Sros_septA*$^{1\text{-}50}$, *Sros_septA-ALFA*^{392}, and *Sros_septA-mSG* rosettes, cultures were grown for 24 h in six-well plates (3 mL per well) with RIF-OMVs. Cultures were prepared in duplicate and experiments to quantify cell volume (Figure 2.S4E) and rosette integrity (Figure 2.S4F) were performed on the same days. On one of the days, cultures were prepared in triplicate and representative DIC images (Figure 2.S4D) were also captured. To compare cell volume within wild-type, *Sros_septA*$^{1\text{-}50}$, *Sros_septA-ALFA*^{392}, and *Sros_septA-mSG* rosettes, microscopy and cell segmentation were performed as described in "Imaging and quantifying cell area and volume." The shorter rosette induction period used here may have contributed to the reduced severity of the *Sros_septA*$^{1\text{-}50}$ cell size phenotype observed in Figure 2.S4E compared to Figure 2.3B.

To analyze the rosette development phenotypes in wild-type, *Sros_septA*$^{1\text{-}50}$, *Sros_septA-ALFA*^{392}, and *Sros_septA-mSG*, we developed an imaging pipeline capable of resolving the number of cells per individual for single cells, doublets, triplets, and rosettes using the Attune CytPix Flow Cytometer (Figure 2.S4G). Using this pipeline, we analyzed septin-tagged rosettes after application of shear force to quantify rosette development (i.e. the combined phenotypes of rosette assembly and rosette integrity) in a single, high-throughput metric. Rosette-induced cultures were first exposed to shear through vortexing at high speed for 15 s using a Vortex Genie 2. The resulting cultures were analyzed on the Attune CytPix using the following settings: 400 µL acquisition volume at a flow rate of 200 µL/min; FSC detector voltage 150; SSC detector voltage 300; FSC threshold 30 × 10³; 5,000 images acquired. To mask the area of individuals and then identify number of cells within those individuals, we trained a custom segmentation and cell identification pipeline by iterative manual annotation of foreground and background objects until cell surfaces were accurately segmented. The custom pipeline was trained on thirty test images from across (1) the four strains analyzed and (2) a diversity of multicellular morphs to create a representative training model. Our CytPix user-trained model is available at Figshare (DOI: 10.6084/m9.figshare.31549345).

This pipeline was not used to analyze the rosette assembly and integrity defects of septin mutants in Figure 2.2H because, although the CytPix is gentle, it may still disrupt rosettes in non-vortexed cultures and thereby confound measurements of rosette assembly. Conversely, the analysis pipeline used for Figure 2.2H was not applied to the tagged septin strain comparison in Figure 2.S4F because we instead combined the rosette assembly and integrity phenotypes into a single metric that avoided measurement bias arising from differences in cell size. In Figure 2.2H, cell size bias was present in between-strain comparisons of rosette assembly; however, phenotypic differences were sufficiently large that this effect was considered acceptable. By contrast, rosette integrity comparisons done in Figure 2.2H were performed within strains, minimizing cell size bias for this metric.

For the representative images of wild-type, *Sros_septA*$^{1\text{-}50}$, *Sros_septA-ALFA*^{392}, and *Sros_septA-mSG* rosettes before and after vortexing (Figure 2.S4D), rosettes were either untreated or vortexed at high speed for 15 s as described above and imaged as described in "Imaging single cells, chains, and rosettes."

Statistics
Information about the quantification and statistical details of experiments can be found in the corresponding figure legends. Statistical tests and graphs were produced using Prism 9.0.0.

Data, script, reagent, and strain availability
Plasmids in this study have been deposited to Addgene (Addgene ID NK812; Cat. No. 253995). Choanoflagellate cell lines used in this study are available upon request. Sequence datasets, multiple sequence alignments, phylogenetic trees, and image-analysis scripts used in this study are available at Figshare (DOI: 10.6084/m9.figshare.31549345).

Chapter 2 Figures and Tables

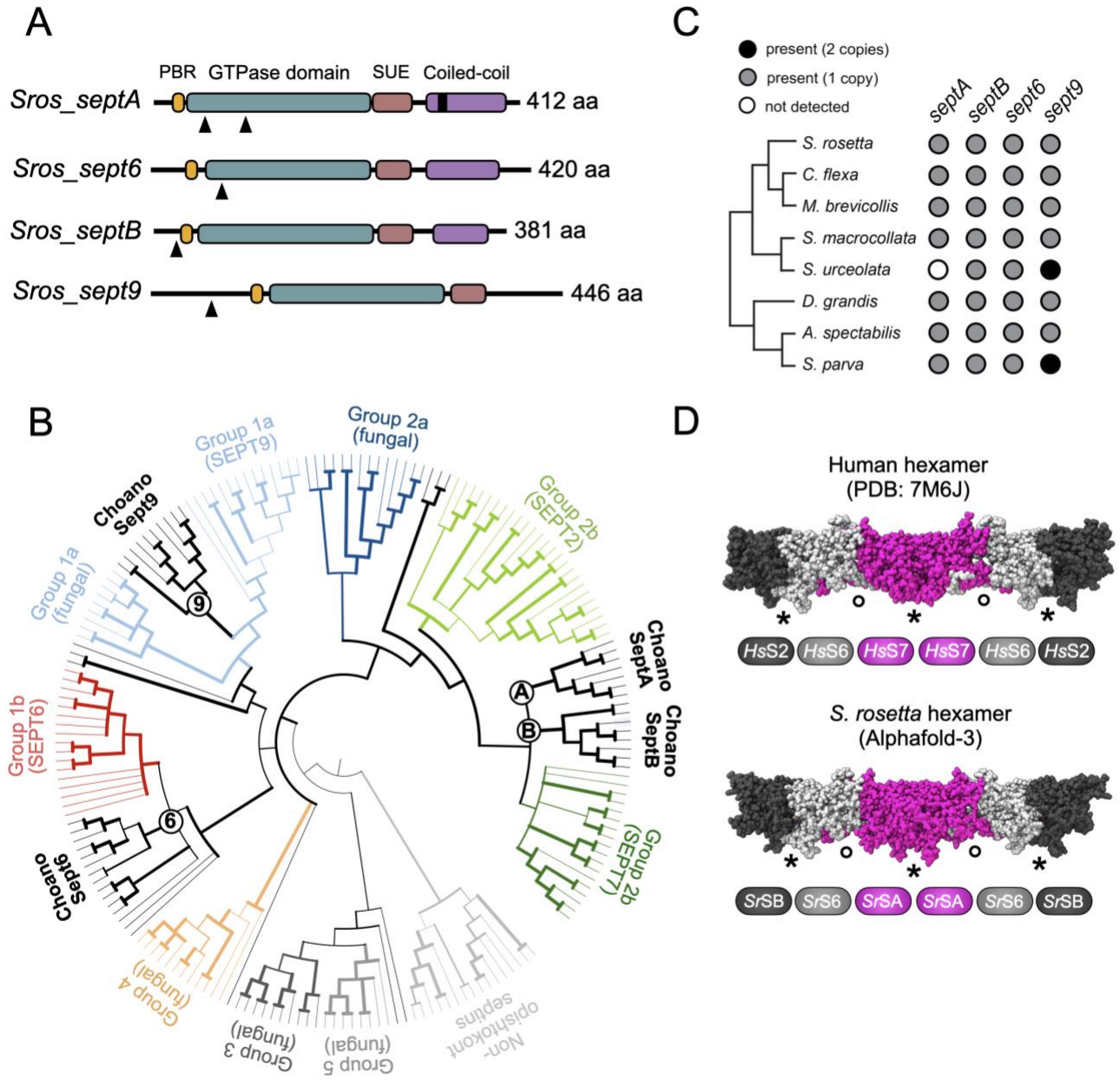

Figure 2.1. Phylogenetic relationships, conservation of protein domain architectures, and predicted hexamer assembly of *S. rosetta* septins. (A) *S. rosetta* encodes four septins – *Sros_septA*, *Sros_sept6*, *Sros_septB*, and *Sros_sept9* – each containing a polybasic region (PBR; orange), a GTPase domain (teal), and septin-unique element (SUE; salmon). A C-terminal coiled-coil domain (purple) is present in *Sros_septA*, *Sros_sept6*, and *Sros_septB*, while an amphipathic helix domain (black rectangle) is present in *Sros_septA*. Black arrowheads indicate

CRISPR-generated truncation sites (Figure 2.S2B; Booth and King, 2020). (B) Choanoflagellate septins are closely related to animal and fungal septins. Choanoflagellate Sept9 clusters with the animal SEPT9 clade (within Group 1a; light blue), while choanoflagellate Sept6 forms a polytomy with animal SEPT6 proteins (red), septins from other close animal relatives, and the *C. elegans* septin *UNC-61* (Group 1b) (Shuman and Momany, 2022). Choanoflagellate SeptA and SeptB form a polytomy with animal SEPT7 within the broader SEPT2/7 animal clade (Group 2b; dark green). A maximum-likelihood phylogeny is shown of predicted septin protein sequences from diverse opisthokonts and selected non-opisthokont taxa (File S1). Branch width scales with UFboot support and all nodes with less than 80% bootstrap support were collapsed. Branch lengths do not scale with evolutionary distance in this rendering. See Figure 2.S1A for full annotated version of this phylogeny. (C) Choanoflagellate septins analyzed in this study belong to four families – *septA*, *septB*, *sept6*, and *sept9* – each broadly distributed across choanoflagellate diversity. The presence of two genes (black circle), one gene (grey circle), or no detected genes (white circle) is indicated. Choanoflagellate septin families were defined based on the septin phylogeny in this study (Figure 2.1B and Figure 2.S1A) and are shown within a composite maximum likelihood phylogeny of choanoflagellates, derived from Carr *et al.* (2017) with the addition of *C. flexa* from Brunet *et al.* (2019). (D) *S. rosetta* septins are predicted to form hexamers resembling those of humans (shown) and other opisthokonts. Human septins within the cryo-EM structure of the human septin hexamer (Mendonça *et al.*, 2021): SEPT2 (*Hs*S2; dark grey), SEPT6 (*Hs*S6; light grey), and SEPT7 (*Hs*S7; magenta). *S. rosetta* septins modeled by AlphaFold-3: *Sros*_SeptB (*Sr*SB; dark grey), *Sros*_Sept6 (*Sr*S6; light grey), and *Sros*_SeptA (*Sr*SA; magenta), with termini trimmed to match the residue coverage of the solved human structure (Materials and Methods). Asterisks denote N- to C-terminal interfaces; circles denote GTP-binding domain interfaces. Confidence scores are given in Figure 2.S1B.

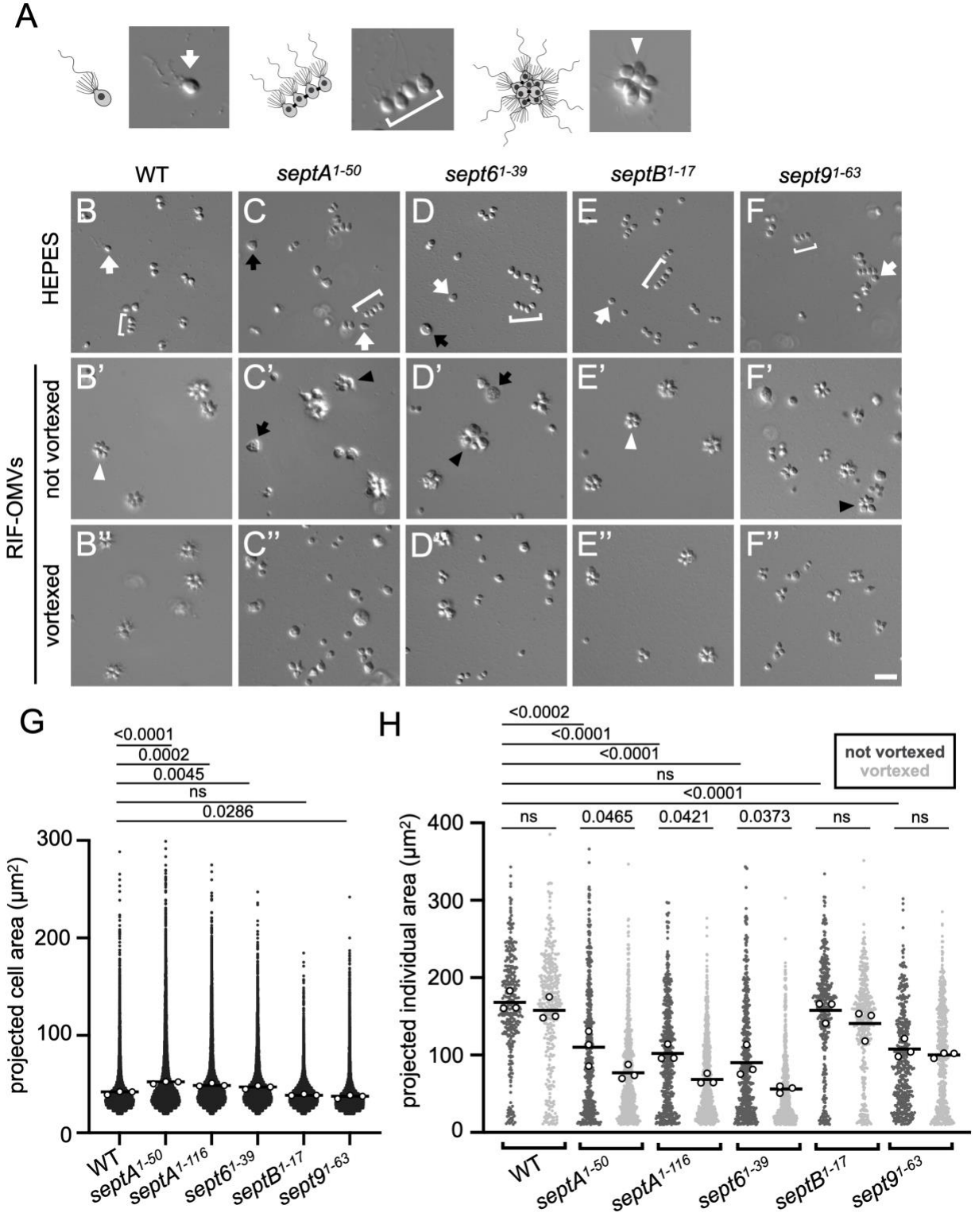
A
WT
septA1-50
sept61-39
septB1-17
sept91-63
HEPES
RIF-OMVs
not vortexed
vortexed
B
C
D
E
F
B'
C'
D'
E'
F'
B''
C''
D''
E''
F''
G
projected cell area (µm²)
<0.0001
0.0002
0.0045
ns
0.0286
WT
septA1-50
septA1-116
sept61-39
septB1-17
sept91-63
H
projected individual area (µm²)
<0.0002
<0.0001
<0.0001
ns
<0.0001
not vortexed
vortexed
ns
0.0465
0.0421
0.0373
ns
ns

Figure 2.2. Septins regulate cell size and the structural integrity of rosettes. (A) The life history of *S. rosetta* includes single cells (left), chains (middle), and rosettes (right). (B – F'') Defects in cell size and rosette morphology in septin mutants. (B – F) Wild-type (B) and septin mutants (C – F) grown with carrier control (HEPES–KOH, pH 7.5) produced slow swimmers (white arrows) and chains (brackets). *Sros_septA*$^{1\text{-}50}$ (C) and *Sros_sept6*$^{1\text{-}39}$ cultures (D) frequently contained larger cells (black arrows). (B' – F') After treatment with RIF-OMVs, wild-type (B') and *Sros_septB*$^{1\text{-}17}$ cultures (E') produced compact rosettes of comparably-sized cells (white arrowheads), whereas *Sros_septA*$^{1\text{-}50}$, *Sros_sept6*$^{1\text{-}39}$, and *Sros_sept9*$^{1\text{-}63}$ strains (C', D', and F') produced abnormal rosettes with both normal and comparatively larger cells (black arrowheads). (B'' – F'') Wild-type (B''), *Sros_septB*$^{1\text{-}17}$ (E''), and *Sros_sept9*$^{1\text{-}63}$ rosettes (F'') maintained their structural integrity after vortexing, while *Sros_septA*$^{1\text{-}50}$ (C'') and *Sros_sept6*$^{1\text{-}39}$ cultures (D'') contained colonies with fewer cells and more single cells after vortexing, indicating reduced structural integrity. Scale bar, 20 μm. (G) When grown without RIF-OMVs, *Sros_septA*$^{1\text{-}50}$ and *Sros_sept6*$^{1\text{-}39}$ strains exhibited significantly increased mean cell sizes compared with wild-type, while the mean cell size in *Sros_sept9*$^{1\text{-}63}$ was reduced. Black dots represent projected cell area of individual cells pooled from three biological replicates (18,382 – 23,313 total cells); white dots represent means per replicate; bars denote means across replicates. Statistics performed on replicate means (n = 3): one-way ANOVA with Dunnett's multiple comparisons test. Further analysis of size distributions is provided in Figure 2.S2F. (H) Septin mutants showed defects in both rosette assembly and rosette integrity. After RIF-OMV treatment, *Sros_septA*$^{1\text{-}50}$, *Sros_septA*$^{1\text{-}116}$, *Sros_sept6*$^{1\text{-}39}$, and *Sros_sept9*$^{1\text{-}63}$ formed smaller structures compared with wild-type, indicating defects in rosette assembly ("rosette assembly defect"). Upon vortexing, the size of individuals in *Sros_septA*$^{1\text{-}50}$, *Sros_septA*$^{1\text{-}116}$, and *Sros_sept6*$^{1\text{-}39}$ significantly decreased ("rosette integrity defect"). Dark grey and light grey dots represent projected area of individual cells or multicellular morphs pooled from three biological replicates for unvortexed and vortexed conditions, respectively (318 – 723 total individuals); white dots represent means per replicate; bars denote means across replicates. Statistics performed on replicate means (n = 3): two-way ANOVA with Dunnett's multiple comparisons test for between-strain and Šidák's test for within-strain comparisons.

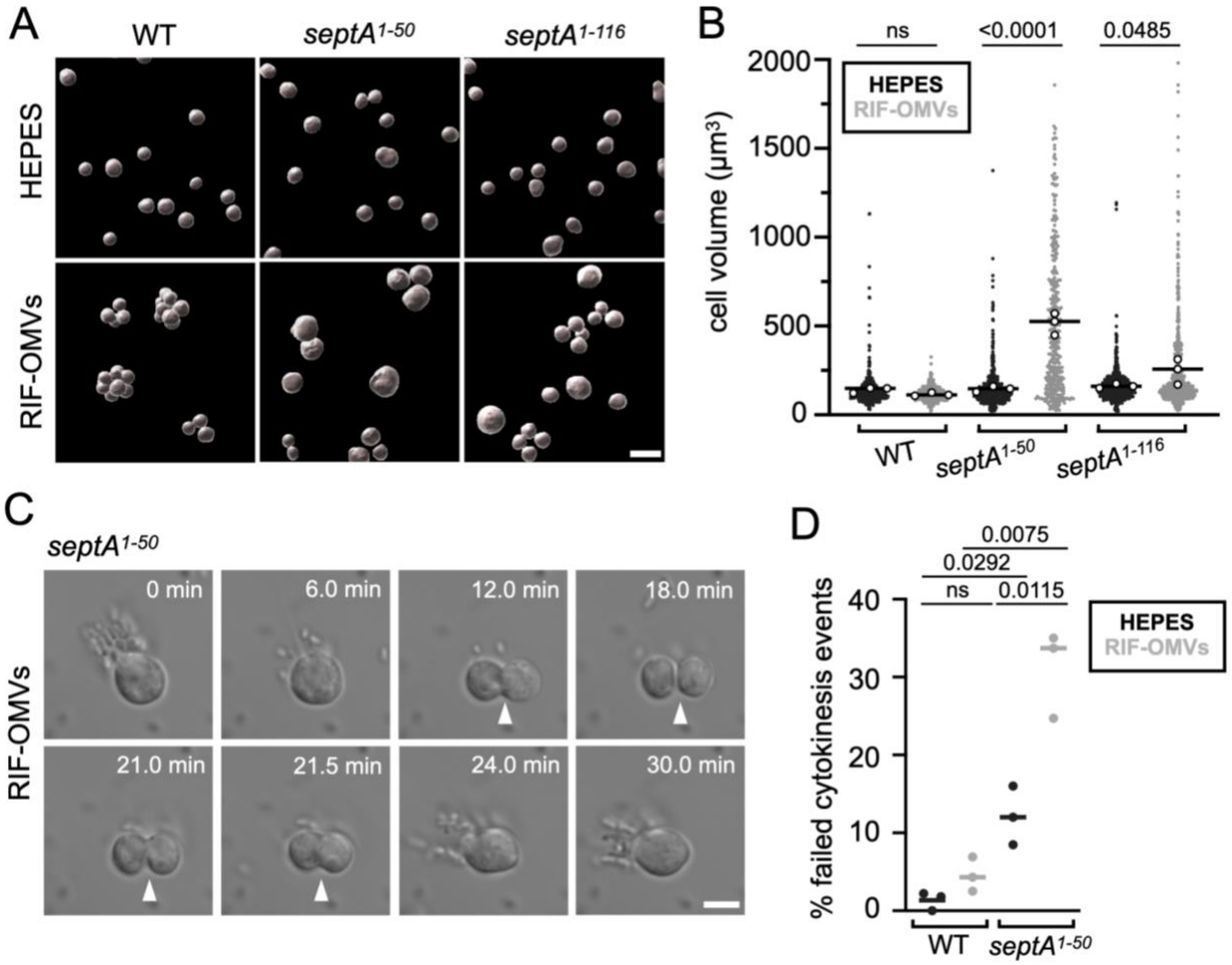

Figure 2.3. Rosette induction in *Sros_septA* mutants leads to increased cell size and cytokinesis defects. (A) Cell segmentation enables quantification of cell volume in single and rosette cells (Figure 2.S3B). Scale bar, 10 µm. (B) Mean cell volume increased significantly after rosette induction in *Sros_septA* mutants, but not in wild-type. Black and grey dots represent cell volumes of individual cells pooled from three biological replicates (359 – 600 cells total) for HEPES and RIF-OMV treatments, respectively; white dots represent means per replicate; bars denote means across replicates. Statistics performed on replicate means (n = 3): two-way ANOVA with Šidák's multiple comparisons test. (C) Time-lapse imaging of a representative *Sros_septA*$^{1-50}$ cell after rosette induction reveals late-stage cytokinesis failure (Video S2). White arrowheads indicate cleavage furrow ingression and cell fusion during cytokinesis progression and collapse (12.0–21.5 min). Scale bar, 5 µm. (D) RIF-OMV treatment increases the rate of cytokinesis failure in *Sros_septA*$^{1-50}$ cells. In wild-type cells, cytokinesis failure was rare and did not differ significantly between untreated and RIF-OMV-treated conditions. In contrast, *Sros_septA*$^{1-50}$ exhibited an elevated baseline failure rate relative to wild-type, which increased more than twofold upon RIF-OMV treatment. Dots represent means per replicate; bars denote means across three biological replicates (166-208 cell division events analyzed in total). Statistics performed on replicate means (n = 3): unpaired t-tests with Welch's correction for each pairwise comparison.

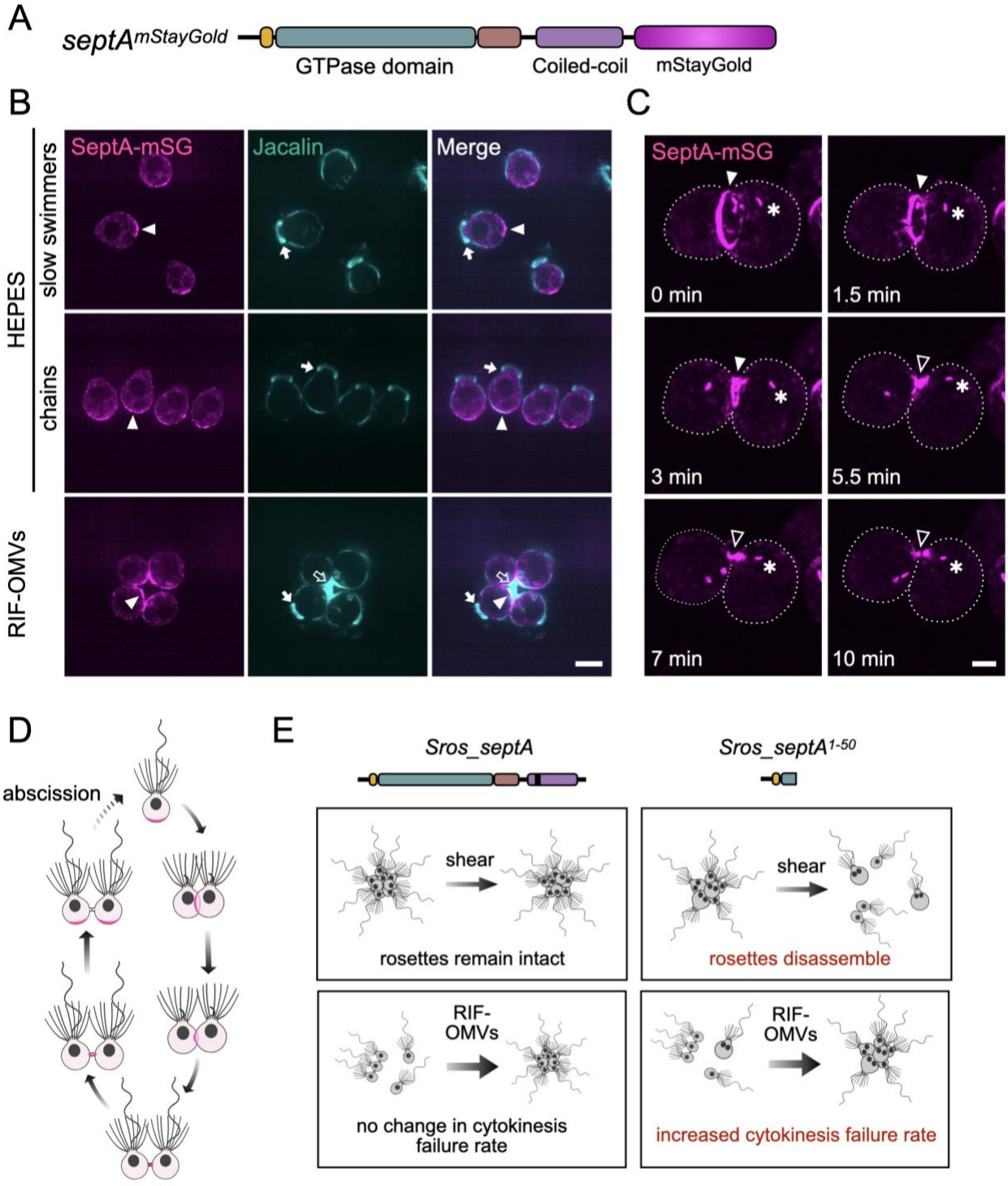
A
septA mStayGold
GTPase domain
Coiled-coil
mStayGold
B
C
HEPES
slow swimmers
chains
RIF-OMVs
SeptA-mSG
Jacalin
Merge
SeptA-mSG
0 min
1.5 min
3 min
5.5 min
7 min
10 min
D
abscission
E
Sros_septA
Sros_septA 1-50
shear
rosettes remain intact
shear
rosettes disassemble
RIF-OMVs
no change in cytokinesis failure rate
RIF-OMVs
increased cytokinesis failure rate

Figure 2.4. SeptA localizes to the basal pole in interphase *S. rosetta* cells and to the cleavage furrow and nascent intercellular bridge in dividing cells. (A) Domain structure of endogenously tagged SeptA-mStayGold (SeptA-mSG). (B) SeptA-mSG is distributed throughout the cytoplasm and enriched at the basal pole in interphase single cells (top row), cells in chains (middle row), and cells in rosettes (bottom row). The lectin Jacalin (teal) marks the collar base (filled arrow) and the ECM of rosettes (open arrow). HEPES served as carrier control for untreated cultures (yielding slow swimmers and chains); RIF-OMVs induced rosettes. Arrowheads mark basal poles of cells. Scale bar, 5 μm. (C) SeptA-mSG accumulates in a ring at the cleavage furrow (filled arrowhead). As cleavage progresses, the ring constricts and SeptA-mSG becomes enriched at the nascent intercellular bridge (open arrowhead), resolving into two puncta after several minutes. Dotted lines outline cell boundaries. Scale bar, 1 μm. Dynamic SeptA-mSG puncta of unknown function were also detected (asterisk). (D) Proposed model for SeptA localization during the cell cycle. In interphase, SeptA (magenta) localizes throughout the cell body and is enriched at the basal pole. During cytokinesis, the flagellum retracts and SeptA redistributes to the cleavage furrow, then to the nascent intercellular bridge. After abscission, SeptA returns to the basal pole. (E) Summary of phenotypes associated with *Sros_septA*$^{1\text{-}50}$. Wild-type cells show no change in cytokinesis failure rate following RIF-OMV treatment and form shear-resistant rosettes. In contrast, *Sros_septA*$^{1\text{-}50}$ mutants exhibit increased cytokinesis failure after rosette induction, resulting in enlarged cells, and form rosettes that disassemble upon shear**.**

Supplemental Figures

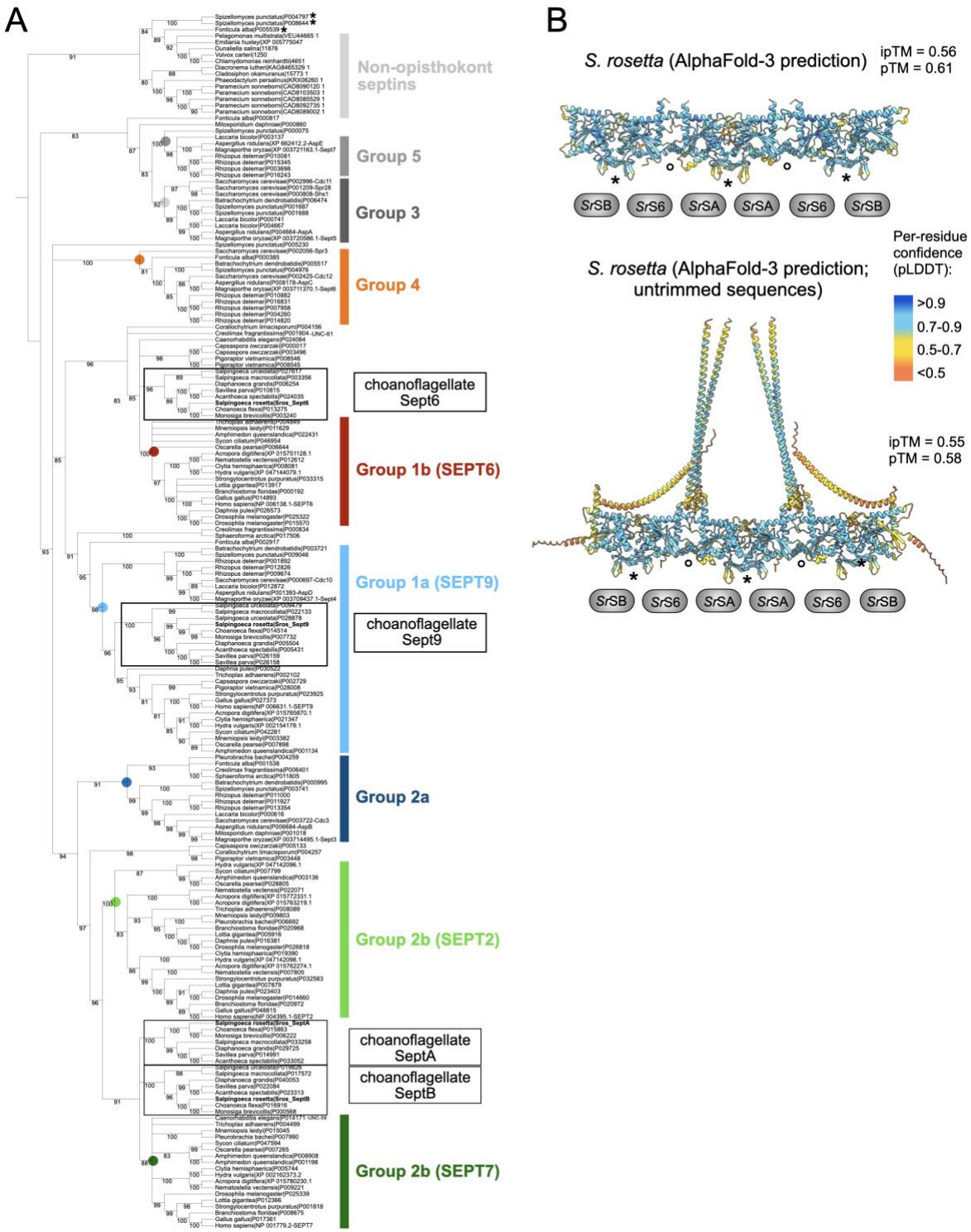

Figure 2.S1. Phylogenetic relationships among diverse eukaryotic septins and predicted assembly of *S. rosetta* septins. (A) Choanoflagellate Sept9 confidently groups within the established fungal and animal SEPT9 clade (Group 1a), while choanoflagellate Sept6 forms a polytomy with animal SEPT6, septins from other close animal relatives, and the *C. elegans* septin *UNC-61* (Group 1b) (Shuman and Momany, 2022). Choanoflagellate SeptA and SeptB form a polytomy with animal SEPT7 within the broader SEPT2/7 animal clade (Group 2b). A maximum-likelihood phylogeny is shown of predicted septin protein sequences from diverse opisthokonts and selected non-opisthokont taxa (File S1). All nodes with less than 80% bootstrap support were collapsed prior to visualization. Established animal and fungal groups are indicated with colored bars and dots at the corresponding nodes, choanoflagellate septin groups are indicated with boxes, and *S. rosetta* septins in bold. The tree is rooted using non-opisthokont septins as an outgroup. Asterisks indicate septins from two early-branching holomycotans, which grouped within the non-opisthokont septins, potentially stemming from complex patterns of duplication and loss, horizontal acquisition, or analytical artifacts. (B) The *S. rosetta* septin hexamer is depicted with the predicted local distance difference test (pLDDT) scores, which largely fell in the 70 – 90 range (Varadi *et al.*, 2022; Abramson *et al.*, 2024). Global model confidence (pTM) and interface confidence (ipTM) values fall below commonly used confidence thresholds but are interpreted cautiously given known limitations with these metrics, including sensitivity to sequence trimming and known limitations in confidently predicting multimeric structures (Liang *et al.*, 2024; Dunbrack, 2025). Top, model generated from trimmed sequences to match the solved human crystal structure (Figure 2.1D); bottom, model generated without trimming and used to define alignment pairs between human and *S. rosetta* septins for sequence trimming. *S. rosetta* septins modeled: *Sros*_SeptB (*Sr*SB), *Sros*_Sept6 (*Sr*S6), and *Sros*_SeptA (*Sr*SA). Asterisks denote N- to C-terminal interfaces and circles denote GTP-binding domain interfaces. Residue-level confidence is shown as a color gradient based on predicted local distance difference test (pLDDT) scores. pTM and ipTM values are indicated for each structure.

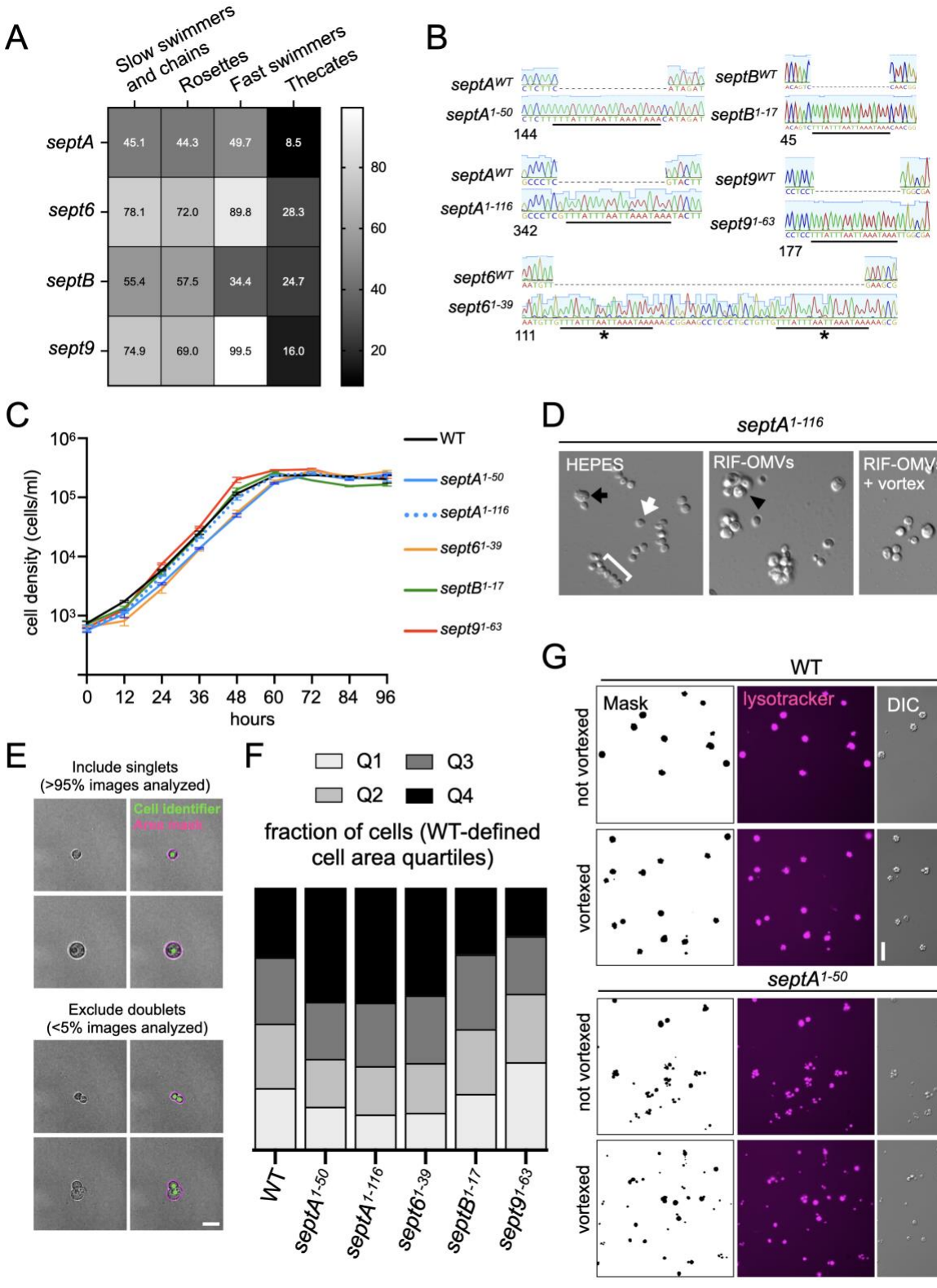
A
Slow swimmers and chains
Rosettes
Fast swimmers
Thecates
septA
septB
sept6
sept9
45.1
44.3
49.7
8.5
78.1
72.0
89.8
28.3
55.4
57.5
34.4
24.7
74.9
69.0
99.5
16.0
80
60
40
20
B
septA^WT
septA^1-50
144
septB^WT
septB^1-17
45
septA^WT
septA^1-116
342
sept9^WT
sept9^1-63
177
sept6^WT
sept6^1-39
111
*
*
C
cell density (cells/ml)
hours
WT
septA^1-50
septA^1-116
sept6^1-39
septB^1-17
sept9^1-63
D
septA^1-116
HEPES
RIF-OMVs
RIF-OMVs + vortex
E
Include singlets (>95% images analyzed)
Cell identifier
Area mask
Exclude doublets (<5% images analyzed)
F
Q1
Q2
Q3
Q4
fraction of cells (WT-defined cell area quartiles)
WT
septA^1-50
septA^1-116
sept6^1-39
septB^1-17
sept9^1-63
G
WT
Mask
lysotracker
DIC
not vortexed
vortexed
septA^1-50
not vortexed
vortexed

Figure 2.S2. Structural modeling, expression, gene editing, and phenotyping of *S. rosetta* septins. (A) Relative to slow swimmers and chains, the expression of all four septins was significantly downregulated in thecate cells ($q < 0.05$ for all comparisons). In contrast, no significant differences were detected between slow swimmers and chains vs. rosette cells. Fast swimmers had a modest but significant reduction in *Sros_septB* expression ($q = 0.048$) compared with slow swimmers and chains, whereas the other three septins showed no significant differences. (B) A premature termination sequence was introduced into each of the four *S. rosetta* septin genes to create septin mutant alleles. Clonally isolated cells were edited with CRISPR/Cas9 and then genotyped by PCR and Sanger sequencing. The premature termination sequence TTTATTTAATTAAATAAA (black lines), encoding a stop codon in every possible reading frame, was introduced in an exon near the 5' end of each gene. Numbers indicate position in the coding DNA sequence of the target gene. For *Sros_sept6*$^{1\text{-}39}$, the premature termination sequence incorporated tandemly (asterisks). (C) Cell proliferation is slightly reduced in *Sros_septA*$^{1\text{-}50}$ and *Sros_sept6*$^{1\text{-}39}$ compared with wild-type. Cells were diluted to 5,000 cells/mL, triplicate samples were collected, and cell density was counted every 12 h for 96 h. Mean values were plotted and error bars denote the standard deviation. (D) Defects in cell size and rosette morphology in *Sros_septA*$^{1\text{-}116}$. *Sros_septA*$^{1\text{-}116}$ cultures grown with a carrier control (HEPES) produced a mixture of single cells (white arrow) and chains (bracket) and also frequently contained larger single cells (black arrow). After treatment with RIF-OMVs, *Sros_septA*$^{1\text{-}116}$ cultures produced abnormal rosettes containing a mixture of normal and comparatively larger cells (black arrowhead). Following application of shear through vortexing, *Sros_septA*$^{1\text{-}116}$ cultures contained smaller colonies and more single cells compared with unvortexed *Sros_septA*$^{1\text{-}116}$ cultures, indicating a reduction in rosette integrity (quantification shown in Figure 2.2H). Scale bar, 20 μm. (E) Cell segmentation allowed for high-throughput analysis of projected area of single cells presented in Figure 2.2G. Cells analyzed through an imaging flow cytometer were processed through a cell segmentation pipeline to allow for accurate measurement of projected cell area. Single cells of variable sizes (top) were included in final analysis while images in which two or more cells were detected (bottom) were filtered out. The area mask (magenta) and cell identifier (green) are shown. Scale bar, 5 μm. (F) When grown without RIF-OMVs, *Sros_septA* and *Sros_sept6* mutants exhibited an increased frequency of oversized cells and a decreased frequency of smaller cells relative to wild-type. Conversely, *Sros_sept9*$^{1\text{-}63}$ exhibited an increased frequency of smaller cells and a decreased frequency of oversized cells. In all strains, the middle two quartiles remained similar. Cell area was quantified from individual cells pooled across three biological replicates (18,382 – 23,313 total cells per strain). Quartile ranges were defined using pooled wild-type data (Q1: <29.79 μm^2; Q2: 29.79 – 35.73 μm^2; Q3: 35.73 – 43.83 μm^2; Q4: >43.83 μm^2), and all septin mutant strains were analyzed relative to these thresholds. (G) An automated image analysis pipeline allowed for the quantification of rosette assembly and integrity phenotypes in wild-type and septin mutants shown in Figure 2.2H. Cells (top: differential interference contrast) were stained with LysoTracker Red DND-99 (middle) and imaged. By generating a binary mask from the fluorescent images, the projected area of each individual was measured (single cell, doublet, triplet, or rosette) in unvortexed and vortexed cultures, creating a proxy quantification of rosette assembly and integrity in response to shear, respectively. Representative images of wild-type and *Sros_septA*$^{1\text{-}50}$ are shown. Scale bar, 20 μm.

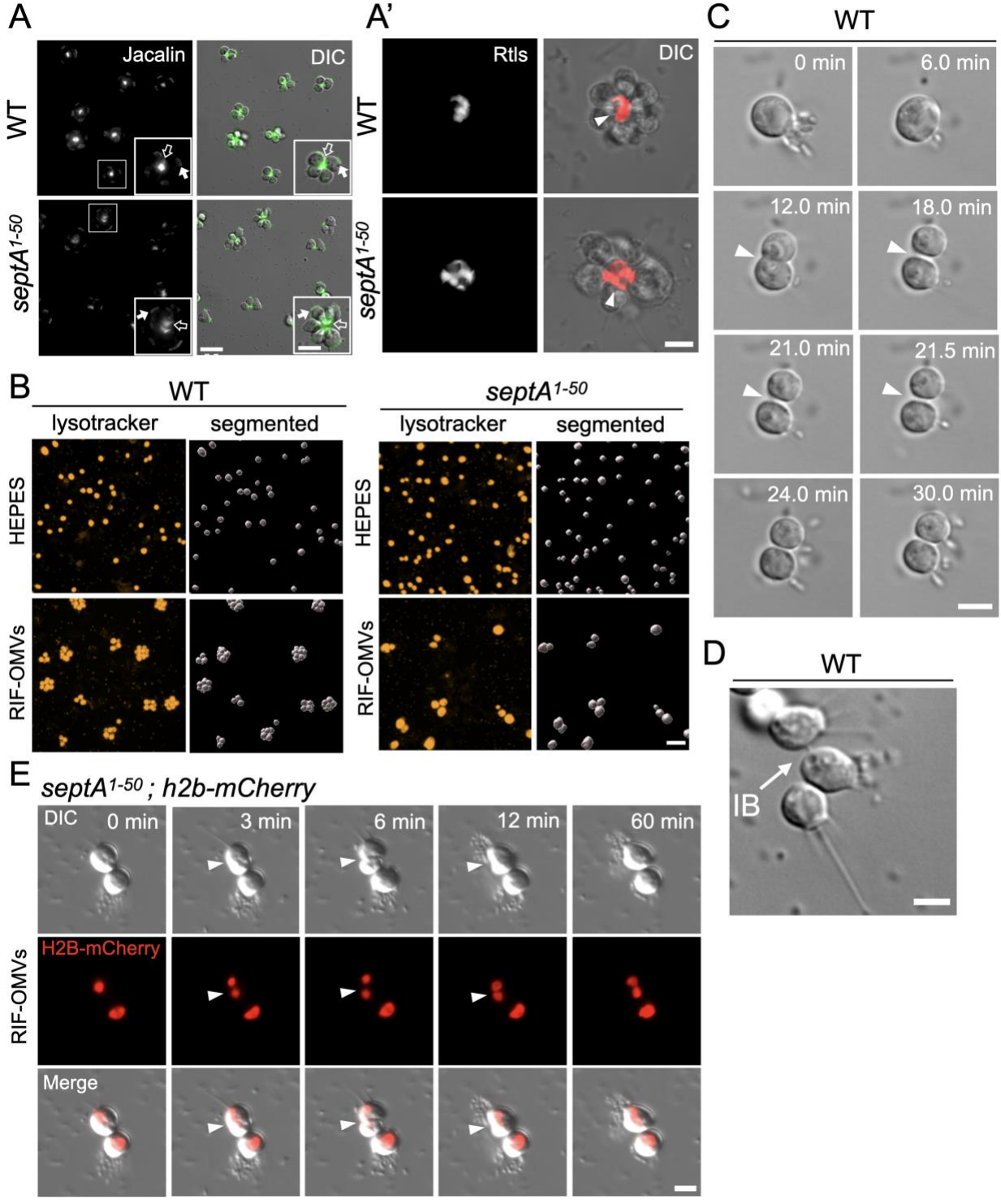
A
Jacalin
DIC
WT
septA1-50
A'
RtIs
DIC
WT
septA1-50
C
WT
0 min
6.0 min
12.0 min
18.0 min
21.0 min
21.5 min
24.0 min
30.0 min
B
WT
septA1-50
lysotracker
segmented
HEPES
RIF-OMVs
D
WT
IB
E
septA1-50 ; h2b-mCherry
DIC
0 min
3 min
6 min
12 min
60 min
H2B-mCherry
RIF-OMVs
Merge

Figure 2.S3: Cellular phenotypes of *Sros_septA* mutants and relevant wild-type *S. rosetta* cell biology. (A-A') *Sros_septA*$^{1\text{-}50}$ cells secrete Jacalin-positive (A) and Rosetteless-positive (A') ECM following rosette induction with RIF-OMVs. (A) Representative images of wild-type and *Sros_septA*$^{1\text{-}50}$ rosettes stained with fluorescein-labeled Jacalin (left), which stains the ECM of rosettes (empty arrow) and the collar base (filled arrow), along with a merged image that shows Jacalin-stained ECM along the basal cell poles at the center of each rosette. A representative rosette is highlighted in the inset for each strain. Scale bar, 10 μm. Inset scale bar, 5 μm. (A') Representative maximum Z-projection images of wild-type and *Sros_septA*$^{1\text{-}50}$ rosettes stained with an antibody to Rosetteless protein (left), a component of the rosette ECM that is necessary for rosette formation (Levin *et al.*, 2014). Fluorescent images merged with DIC (right) show the ECM along the basal cell poles (arrowhead) at the center of each representative rosette. Scale bar, 5 μm. (B) A cell segmentation pipeline allowed for analysis of cell volume of wild-type (left) and *Sros_septA*$^{1\text{-}50}$ (right) single cells and rosettes. Three-dimensional confocal fluorescence imaging of single cells and rosettes stained with LysoTracker Red DND-99 (left, center Z-section is shown) followed by machine learning-based segmentation (right, 3D top-down renderings shown) allowed for accurate cell volume measurements of cells in rosettes, enabling comparison of cell size between uninduced and rosette-induced cultures in both wild-type (B) and *septA*$^{1\text{-}50}$ mutants (B'). Scale bar, 15 μm. (C) Wild-type cells undergo cytokinesis and remain attached following cell division. Times shown were chosen to match the visual cues (6 min – bacterial ejection from collar; 12 min – furrow ingression; 18 min – two cells appear distinct) of the *Sros_septA*$^{1\text{-}50}$ cytokinesis failure panels in Figure 2.3C. Furrow ingression at the basal pole is indicated (arrowhead). In this representative time series, unlike with *Sros_septA*$^{1\text{-}50}$, a wild-type cell that divides between 6 and 18 min remains divided after 30 min (Video S1). Scale bar, 5 μm. (D) Cells in wild-type chains are connected by intercellular bridges. Shown is a representative image of a chain colony with an intercellular bridge (IB) indicated by a white arrow. Scale bar, 5 μm. (E) Cytokinesis failure in *Sros_septA*$^{1\text{-}50}$ results in multinucleated cells. A representative cytokinesis failure event is shown with a *Sros_septA*$^{1\text{-}50}$ cell expressing the nuclear marker H2B–mCherry following rosette induction: DIC (top); H2B–mCherry fluorescence (middle); merged images (bottom). H2B-mCherry-labeled nuclei divide during mitosis and remain distinct following cytokinesis failure, resulting in a multinucleated cell (Video S3). White arrowheads indicate the cleavage furrow. Time (minutes) is indicated. Scale bar, 5 μm.

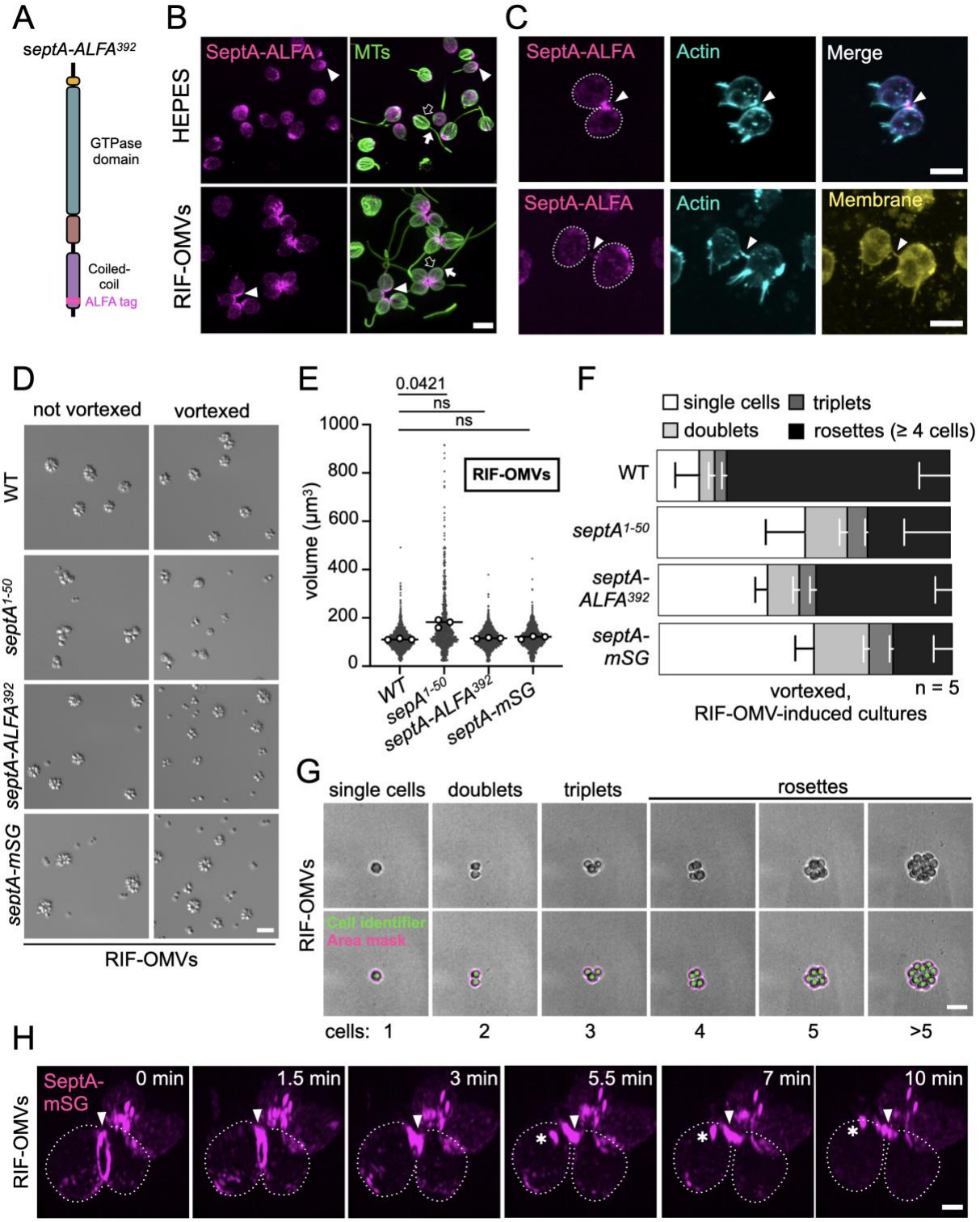
A
septA-ALFA392
GTPase domain
Coiled-coil
ALFA tag
B
HEPES
RIF-OMVs
SeptA-ALFA
MTs
C
SeptA-ALFA
Actin
Merge
SeptA-ALFA
Actin
Membrane
D
not vortexed
vortexed
WT
septA1-50
septA-ALFA392
septA-mSG
RIF-OMVs
E
0.0421
ns
ns
RIF-OMVs
volume (µm3)
1000
800
600
400
200
0
WT
sepA1-50
septA-ALFA392
septA-mSG
F
single cells
triplets
doublets
rosettes (≥ 4 cells)
WT
septA1-50
septA-ALFA392
septA-mSG
vortexed,
RIF-OMV-induced cultures
n = 5
G
single cells
doublets
triplets
rosettes
RIF-OMVs
Cell identifier
Area mask
cells: 1
2
3
4
5
>5
H
RIF-OMVs
SeptA-mSG
0 min
1.5 min
3 min
5.5 min
7 min
10 min

Figure 2.S4. Localization and phenotypic effects in ALFA-tagged and mStayGold-tagged *Sros_septA* strains. (A) *Sros_septA* was endogenously tagged with an ALFA epitope at amino acid position 392 of the predicted protein sequence, enabling immunofluorescence imaging using anti-ALFA nanobodies (Götzke *et al.*, 2019). (B) SeptA-ALFA^{392} localization patterns are similar to those of SeptA-mStayGold (Figure 2.4B). *Sros*_SeptA-ALFA stained with an anti-ALFA nanobody (left) reveals cytoplasmic and basal enrichment (arrowhead), while microtubules marking the cell body ("tubulin cage", empty arrow) and apical flagella (filled arrow) were visualized with an anti-α-tubulin antibody. Scale bar, 5 μm. (C) *Sros*_SeptA-ALFA localizes to intercellular bridges (arrowhead) in dividing cells. Top: representative example of strong SeptA-ALFA localization. Bottom: representative example of weak SeptA-ALFA localization. Actin is labeled with phalloidin; membrane is labeled with FM-1-43-FX dye. Scale bar, 5 μm. (D) Rosette integrity defects are associated with tagging *Sros_septA*. Representative images of rosette-induced cultures before and after application of shear through vortexing are shown. Wild-type rosettes appear unaffected after shear, while *Sros_septA$^{1-50}$* rosettes disassemble. *Sros_septA-ALFA^{392}* and *Sros_septA-mSG* strains also disassemble, with more single cells and smaller rosette structures following the application of shear. Scale bar, 10 μm. (E) Tagged septin strains do not have a cell size defect following rosette induction. In contrast to *Sros_septA$^{1-50}$*, mean cell volume is not significantly different in rosette-induced tagged septin strains compared with wild-type. Dots represent cell volume of individual cells pooled from three biological replicates following 24 h RIF-OMV treatment (831–1528 total cells); white dots represent means per replicate; bars denote means across replicates. Statistics performed on replicate means (n = 3): one-way ANOVA with Dunnett's multiple comparisons test to compare between strains. (F) Rosette integrity is decreased in tagged septin strains compared with wild-type. Using the cell segmentation pipeline described in (G), the fraction of individuals that were single cells, doublets, triplets, or rosettes per strain were determined and the means of 5 biological replicates (25,000 cells pooled in total) per strain are plotted with error bars representing standard deviation. (G) Image analysis pipeline allowed for high-throughput analysis of cells per individual following vortexing. Vortexed, rosette-induced cultures passed through a flow cytometer were imaged and processed through a cell segmentation pipeline that reliably identified cells per individual for structures up to 5 cells. Individual mask is shown in magenta while the cell identifier is in green. Scale bar, 10 μm. (H) SeptA-mSG accumulates in a ring at the cleavage furrow (filled arrowhead) and nascent intercellular bridge of dividing rosette-induced cells (Video S5) (localization in uninduced dividing cells shown in Figure 2.4C). As cleavage progresses, the SeptA-mSG ring constricts and becomes enriched at the nascent intercellular bridge connecting the daughter cells (open arrowhead), resolving into two puncta after several minutes. Dotted lines outline cell boundaries. Scale bar, 1 μm. In both single cells and rosette cells, we additionally detected dynamic SeptA-mSG puncta of unknown function (Figure 2.4C and 2.S4H, asterisks).

Supplemental Tables

Table S1 — Comparison of *S. rosetta* septin expression across life history states

Septin	Life history stage	Fold change vs slow swimmers/chains	p-value	q-value	Interpretation
Sros_septA	rosette	-0.036	0.859	1.000	Not significantly different
Sros_sept6	rosette	-0.121	0.539	1.000	Not significantly different
Sros_septB	rosette	0.063	0.802	1.000	Not significantly different
Sros_sept9	rosette	-0.126	0.527	1.000	Not significantly different
Sros_septA	fast swimmer	0.139	0.496	0.669	Not significantly different
Sros_sept6	fast swimmer	0.204	0.302	0.498	Not significantly different
Sros_septB	fast swimmer	-0.657	0.008	0.048	Significant, slight decrease
Sros_sept9	fast swimmer	0.415	0.036	0.129	Not significantly different
Sros_septA	thecate	-2.453	1.95e-33	2.58e-32	Significantly lower
Sros_sept6	thecate	-1.506	2.59e-14	1.15e-13	Significantly lower
Sros_septB	thecate	-1.208	1.26e-6	3.04e-6	Significantly lower
Sros_sept9	thecate	-2.273	1.00e-30	1.17e-29	Significantly lower

Table S2 — Mean cell size (slow swimmers & chains)

Strain	Mean cell area (µm²)	Fold change	p-value vs WT	Interpretation
Wild-type	41.28	—	—	Reference
Sros_septA$^{1\text{-}50}$	51.75	1.25×	< 0.0001	Significantly larger
Sros_septA$^{1\text{-}116}$	49.28	1.19×	0.0002	Significantly larger
Sros_sept6$^{1\text{-}39}$	46.77	1.13×	0.005	Significantly larger
Sros_sept9$^{1\text{-}63}$	37.15	0.90×	0.0286	Significantly smaller
Sros_septB$^{1\text{-}17}$	38.91	0.94×	0.2684	Not significantly different

Table S3 — Mean projected "individual" size after RIF-OMV–induced rosette formation (Individuals = single cells, doublets, triplets, or rosettes)

Strain	Mean area (µm²)	p-value vs WT	Interpretation
Wild-type	168.3	—	Reference
Sros_septA$^{1\text{-}50}$	110.1	0.0002	Significantly smaller
Sros_septA$^{1\text{-}116}$	102.1	< 0.0001	Significantly smaller
Sros_sept6$^{1\text{-}39}$	90.2	< 0.0001	Significantly smaller
Sros_sept9$^{1\text{-}63}$	107.9	< 0.0001	Significantly smaller
Sros_septB$^{1\text{-}17}$	157.8	0.8236	Not significantly different

Table S4 — Mean projected individual size after RIF-OMV-induced formation *after exposure to shear* (Individuals = single cells, doublets, triplets, or rosettes)

Strain	Mean area after shear (µm²)	p-value (vs pre-shear)	Interpretation
Wild-type	157.9	0.9382	Rosettes intact
Sros_septA$^{1\text{-}50}$	77.05	0.0465	Significant disassembly
Sros_septA$^{1\text{-}116}$	68.48	0.0421	Significant disassembly
Sros_sept6$^{1\text{-}39}$	56.03	0.0373	Significant disassembly
Sros_sept9$^{1\text{-}63}$	100.2	0.9856	No significant disassembly
Sros_septB$^{1\text{-}17}$	141.0	0.6301	No significant disassembly

Table S5 — Effect of RIF-OMV-induced rosette induction on cell volume

Strain	Condition	Mean cell volume (µm³)	Fold change	p-value	Interpretation
Wild-type	Uninduced	140.2	—	—	Reference
	RIF-OMV	115.7	0.83×	0.8345	No significant change
Sros_septA$^{1\text{-}50}$	Uninduced	145.9	—	—	Reference
	RIF-OMV	515.1	3.53×	< 0.0001	Strong increase
Sros_septA$^{1\text{-}116}$	Uninduced	162.2	—	—	Reference
	RIF-OMV	250.0	1.54×	0.0485	Moderate increase

Table S6 — Cytokinesis failure rates during the first 10 hours following RIF-OMV rosette induction

Strain	Condition	Cytokinesis failure rate (%)	Comparison	p-value	Interpretation
Wild-type	Uninduced	2.0	—	—	Baseline
Wild-type	RIF-OMV	4.6	vs WT uninduced	0.1101	No significant induction effect
Sros_septA$^{1-50}$	Uninduced	12.2	vs WT uninduced	0.0292	Elevated vs WT
Sros_septA$^{1-50}$	RIF-OMV	30.9	vs *Sros_septA*$^{1-50}$ uninduced	0.0115	Significantly higher failure rate following induction within *Sros_septA*$^{1-50}$

Supplemental videos and data files described below are available in the bioRxiv preprint.
Carver, M, and King, N (2026). Septins regulate cytokinesis and multicellular development in the closest living relatives of animals. *bioRxiv*, 2026.04.05.716596

Supplemental Videos

Video S1. Wild-type *S. rosetta* cells typically complete cytokinesis.

DIC time-lapse microscopy of a wild-type *S. rosetta* cell undergoing cell division. Time (hours:minutes:seconds) is indicated. Scale bar, 2 µm. Related to Figure 2.S3C.

Video S2. *Sros_septA*$^{1-50}$ mutant cells frequently fail cytokinesis following RIF-OMV induction.

DIC time-lapse microscopy of a *Sros_septA*$^{1-50}$ cell following rosette induction with RIF-OMVs. After cleavage furrow ingression, the two daughter cells fuse, indicating a defect in a late stage of cytokinesis. Time (hours:minutes:seconds) is indicated. Scale bar, 2 µm. Related to Figure 2.3C.

Video S3. Nuclei remain separated after cells re-fuse in *Sros_septA*$^{1-50}$ mutants.

DIC and fluorescence time-lapse microscopy of *Sros_septA*$^{1-50}$ cells expressing the nuclear marker H2B–mCherry following rosette induction with RIF-OMVs. Left: merge of H2B–mCherry fluorescence and DIC. Right: H2B–mCherry fluorescence. H2B–mCherry-labeled nuclei divide during mitosis and remain distinct following cytokinesis failure, resulting in a large, multinucleated cell. Time (hours:minutes:seconds) is indicated. Scale bar, 5 µm. Related to Figure 2.S3E.

Video S4. SeptA-mStayGold localizes to the cleavage furrow in uninduced dividing cells.

Three-dimensional fluorescence time-lapse microscopy of an endogenously tagged SeptA-mStayGold (*Sros_septA*-mSG) cell dividing under uninduced conditions (slow swimmer). SeptA-mSG accumulates in a ring at the cleavage furrow during ingression, constricts as cytokinesis progresses, and becomes enriched at the nascent intercellular bridge, ultimately resolving into two puncta. Time (hours:minutes:seconds) is indicated. Related to Figure 2.4C.

Video S5. SeptA-mStayGold localizes to the cleavage furrow in rosette-induced dividing cells.

Three-dimensional fluorescence time-lapse microscopy of an endogenously tagged SeptA-mStayGold (*Sros_septA*-mSG) cell dividing following rosette induction with RIF-OMVs. Similar to uninduced cells, SeptA-mSG accumulates at the cleavage furrow and nascent intercellular bridge, resolving into two puncta after several minutes. Scale bar, 1 μm. Related to Figure 2.S4H.

Supplemental Data

File S1. Data underlying phylogenetic and structural analysis of septins.

This file documents the identification and filtering of septin sequences used to construct the phylogeny in Figure 2.S1A. Tab “probe_sequences" lists the four human septin sequences (SEPT2, SEPT6, SEPT7, SEPT9) used as BLAST probes. Tab "species_used" lists all species queried. Tab "interproscan_putseptins_all" provides raw InterProScan domain predictions for all 201 candidate sequences. Tab "PF00735-positives" lists the protein length and lowest e-value PF00735 domain for each of the 201 putative septins. Tab "filtered_final_list" contains the 192 sequences retained after filtering by domain architecture and protein length. Tab "excluded" lists the 9 sequences removed after domain filtering, with reasons. Tab “structural analysis” contains the N- and C-terminally trimmed human septins used to align and trim the *S. rosetta* septins (also listed) used for AlphaFold-3 structural predictions.

File S2. Corrected *Sros_septB* (PTSG_04364) coding and protein sequence.

Tab "Sros_septB_corrected-seq" provides the revised *Sros_septB* CDS and protein sequences, corrected using RNA-seq read evidence (deposited at GenBank under accession PZ120989). Tab "RNAseq_reads_revision" documents the RNA-seq read support counts used to identify and correct intron–exon boundaries in the original genome annotation, with intron coordinates, strand, and read support for each junction.

File S3. Differential expression of *S. rosetta* septin genes across cell states.

Tab "Sros_septins_RNAseq" reports pairwise differential expression statistics for all four *S. rosetta* septin genes (*Sros_septA*, *Sros_sept6*, *Sros_septB*, *Sros_sept9*) across cell state comparisons (slow swimmers and chains vs. thecate, rosette, and fast swimmer cells). The upper section includes TPM values for individual biological replicates (three per condition), condition averages, standard deviations, p-values, q-values, $\log_2$ fold-change, and standard error of fold-change, as well as Ensembl, UniProt, Pfam, InterPro, GO, and eggNOG annotations. The lower

section summarizes results using condition averages only, with a qualitative "Comment" column. Data are from Leon *et al*. (2025) and underlie Figure 2.S2A and Table S1.

File S4. CRISPR-Cas9 reagents for septin gene disruption and tagging.

Tab "CRISPR gene edits" provides gRNA sequences, repair template sequences, insertion sites (CDS position), and genotyping primer pairs for all gene truncation and tagging experiments, including alleles of *Sros_septA* (two truncation lengths: 50 and 116 aa; plus ALFA-tag insertion), *Sros_sept6* (39 aa), *Sros_septB* (17 aa), *Sros_sept9* (63 aa), and the *rpl36a*-P56Q cycloheximide-resistance locus. Also includes editing efficiency metrics (number of experiments, clones genotyped, and independent edited clones obtained). Tab "ALFA-tag" provides further details about the ALFA-tag repair template design, including annotated sequences for the crRNA binding site sequence and ALFA-tag insertion, along with the associated *Sros_septA* CDS.

File S5. Reagents for endogenous *Sros_SeptA*–mStayGold (SeptA-mSG) tagging.

Tab "SeptA-mSG_sequences" documents all sequences used to generate the SeptA-mSG knock-in strain (NK812), including: the mStayGold nucleotide and protein sequences; the SGGSGGS linker sequences; the gene block for Gibson assembly into plasmid pMS18; Gibson cloning and PCR amplification primers (with annealing temperature and extension time); the crRNA sequence; and three genotyping primer pairs for confirming correct insertion. Tab "SeptA-mSG_codon-changes" lists the eight synonymous codon substitutions introduced into the plasmid-encoded *Sros_septA* recovery region to reduce homologous recombination with the repair template, with original and replacement codons and their relative usage frequencies (from Leon *et al*. (2025)).

Appendix 1

Additional data and future directions on septin function in *S. rosetta*

Introduction

The following data extend the findings of Chapter 2 by examining the localization of *Sros*_SeptA and F-actin to intercellular bridges and putative filopodia in *S. rosetta*. These observations suggest new directions for future research, but I present them separately because their biological significance remains uncertain and will require additional testing. This appendix also outlines broader future directions motivated by Chapter 2, with a focus on how cell division, multicellularity, and septin function intersect in choanoflagellates, and how these relationships may inform our understanding of animal origins.

*Sros*_SeptA and actin localize to intercellular bridges in S. rosetta

S. rosetta chain and rosette colonies are frequently connected through intercellular bridges, but the molecular mechanisms underlying intercellular bridge formation in *S. rosetta* remain unknown (Dayel *et al.*, 2011; Chaigne and Brunet, 2022). Through adapted fixation techniques (Appendix 1 and Chapter 2 methods), I have been able to retain and image intercellular bridges in doublets and chains of uninduced *S. rosetta* cultures (Figure A1.1A and A1.1B-B''). Phalloidin staining of fixed chain colonies revealed their cells were often connected by intercellular bridges that contained two discrete F-actin signals, either in puncta or short bar-like structures, positioned on either side of the bridge, with a central gap between (Figure A1.1A insets, white arrows). This pattern was observed frequently and was distinct from the more diffuse cortical actin staining elsewhere in the cell. The exclusion of F-actin from the central region is consistent with previous observations that multiple cytoplasmic regions are separated by electron dense plates at the center of intercellular bridges (Dayel *et al.*, 2011). Notably, *Sros*_SeptA also localized to intercellular bridges as two puncta during early bridge formation in my Chapter 2 study (Figure 2.4C), suggesting that septins and actin may share a similar spatial organization at these sites.

The observation that actin and *Sros*_SeptA localize to intercellular bridges as two puncta flanking a central gap suggests that bridge architecture in *S. rosetta* is spatially organized along its length. A similar organization has been described in animal cells, where late-stage intercellular bridges contain two flanking rings composed of actomyosin, septins, and associated scaffolding proteins positioned on either side of the midbody (Karasmanis et al., 2019; Gerhold et al., 2022). These structures are thought to define sites of membrane remodeling and contribute to the regulation of abscission. The similarity in spatial pattern raises the possibility that actin and septins in *S. rosetta* intercellular bridges mark similar molecular machinery.

Imaging of phalloidin-labeled F-actin and nanobody-stained *Sros*_SeptA-ALFA revealed variable staining patterns at intercellular bridges between images, including differences in relative intensity (Figure A1.1B–B'', white arrowheads). In some intercellular bridges, strong *Sros*_SeptA signal was accompanied by weaker F-actin signal (Figure A1.1B), whereas in others F-actin was more prominent and *Sros*_SeptA signal was reduced (Figure A1.1B' and B''). These differential staining patterns suggest that either the localization or abundance of F-actin and *Sros*_SeptA is dynamic across different stages of intercellular bridge development, or that the fixation or staining methods produce variable signal across samples.

In Chapter 2, I demonstrated that *Sros*_SeptA-mStayGold localized to nascent intercellular bridges after division (Figure 2.4C) but was not detectable at connections between cells in chain colonies (Figure 2.4A). These observations raise the possibility that *Sros*_SeptA localization or abundance changes during intercellular bridge maturation. Because F-actin is often enriched at intercellular bridges in chains (Figure A1.1A), one possible model is that septins are enriched earlier in bridge formation, whereas actin persists or becomes more prominent later. However, these patterns could also reflect differences in mechanical state or experimental variation introduced by fixation and staining, rather than age. Distinguishing between these possibilities will require time-resolved imaging and quantitative analysis of intercellular bridge composition.

These observations also motivate broader tests of conserved intercellular bridge-regulatory machinery in *S. rosetta*. This includes Aurora kinase, ALIX, TSG101, VPS4, and components of the ESCRT-III machinery (CHMP2, 4, and 6) (Chaigne and Brunet, 2022). In animal cells, delayed or incomplete abscission can stabilize intercellular bridges, and this process is regulated by various factors, including Aurora B signaling, septins, and ESCRT recruitment (Estey *et al.*, 2010; Mierzwa and Gerlich, 2014; Chaigne and Brunet, 2022). Beyond the focus of septin function, a project targeting these conserved factors through CRISPR/Cas9-mediated disruption or fluorescent tagging may provide insights into whether animal-like bridge regulation mechanisms are conserved in choanoflagellates and are thus potentially ancestral characteristics of the choanozoan stem lineage.

Sros*_SeptA and actin localize to putative filopodia in *S. rosetta

In addition to their localization at intercellular bridges, both F-actin and *Sros*_SeptA were observed in protrusive structures extending from the basal pole of uninduced cells (Figure A1.1C, white arrows). These structures resembled basal filopodia previously described in *S. rosetta* (Dayel *et al.*, 2011). Actin was distributed along the length of the protrusion and *Sros*_SeptA was enriched near the base. So far, however, I have not been able to observe these putative filopodia in rosettes using phalloidin staining or *Sros*_SeptA-ALFA staining, potentially because the rosette interior is dense and more difficult to resolve by fluorescence microscopy relative to basal pole structures in single cells.

Septin localization to filopodia-like structures suggests that septins may have functions outside cytokinesis in *S. rosetta.* In animal cells, septins localize to filopodia and regulate their formation and stability (Hu *et al.*, 2012b; Radler *et al.*, 2023). The localization pattern observed in *S. rosetta*, with septins enriched at the base of actin-rich protrusions, raises the possibility that septins contribute to filopodial organization in this system as well. In rosette colonies, basal filopodia extend into the ECM and are thought to help anchor cells within the colony (Dayel *et al.*, 2011; Larson *et al.*, 2020). If septins regulate these structures, this could provide a direct link between septin function and rosette integrity. Moreover, if septins localize to and regulate filopodia in choanoflagellates, this would suggest that this function predates the divergence of choanoflagellates and animals.

Future directions

Although Chapter 2 provides a detailed account of the phenotypes associated with disruption of the septin cytoskeleton, as well as the localization pattern of *Sros*_SeptA, many questions remain. One central question is how the multicellular context of rosettes alters septin function during cytokinesis (Figure A1.2A). Two possibilities seem plausible: (1) the mechanical environment of rosette development places additional demands on the cytokinetic machinery, and (2) septins are regulated differently in rosettes than in single cells.

One way to test whether the physical environment contributes to the septin mutant phenotype in rosettes would be to manipulate uninduced cells to more closely resemble the adhesive or mechanical conditions of rosettes, and then test the septin mutants in those conditions. For example, attaching cells to a surface coated with different concentrations of glycosylated substrate could serve as a proxy for the adhesive environment of a rosette. This would allow cytokinesis defects to be compared between wild-type and septin mutants under controlled conditions of increased substrate attachment. If septin mutants were more sensitive to cell-surface adhesion, as measured by an increased cytokinesis failure rate, this would suggest that adhesion directly contributes to the rosette-specific phenotype. A related approach would be to alter the properties of rosette ECM and test how these changes influence cytokinesis. Treatment with strontium chloride, which has been proposed to stiffen the rosette ECM (Larson *et al.*, 2020), could be used to assess whether increased ECM stiffness enhances cell size or cytokinesis failure rate in both wild-type and septin mutant cells.

A related question is whether septin-dependent phenotypes require the full rosette developmental program. This could potentially be tested in a *rosetteless* mutant background, which lacks proper ECM secretion and does not form rosettes (Levin *et al.*, 2014). One caveat is that the *rosetteless* phenotype is not fully understood: it may reflect a defect in ECM structure alone, or it may also affect the upstream response to RIF-OMV induction. Even so, disrupting *Sros_septA* in this background and assessing cytokinesis failure with and without RIF-OMV induction could test whether the phenotype observed in *Sros_septA*$^{1–50}$ cultures persists without structural rosette formation. If cytokinesis defects remain elevated after RIF-OMV induction, this would suggest that septin function is affected by RIF-OMV-induced signaling independently of ECM secretion and attachment. If uninduced and induced cultures no longer differ, the result would be harder to interpret, but would be consistent with the multicellular environment contributing to the phenotype observed in *Sros_septA*$^{1–50}$.

A second explanation for the rosette-dependent cytokinesis phenotype is that *Sros_septA* could be differentially regulated in rosettes vs. single cells (Figure A1.2A). As mentioned in Chapter 2, transcriptomics showed that the expression levels of *Sros_septA*, along with the other septins, do not differ between these two states (Figure 2.S2A; Leon *et al.*, 2025). However, post-transcriptional regulation of protein abundance or post-translational modification could alter septin function, as is often the case in animals (Sharma and Menon, 2023). Comparative proteomics of uninduced and RIF-OMV-induced cultures could test whether septin protein abundance changes despite similar transcript levels. Mass spectrometry following *Sros*_SeptA affinity purification approaches could be used to ask whether *Sros*_SeptA carries rosette-specific

post-translational modifications, such as phosphorylation, that might alter septin assembly, localization, or activity.

The role of septins in rosette integrity also remains unclear (Figure A1.2B). The observation that septins localize to basal, filopodia-like structures raises the possibility that they contribute to filopodia-regulated cell-ECM attachment within rosettes (Dayel *et al.*, 2011). This possibility could be explored by first determining whether filopodia in rosettes could be imaged using an actin marker such as Lifeact-mCherry. If Lifeact-mCherry-positive filopodia can be imaged in this context, generating a *Sros_septA*$^{1–50}$; *Lifeact-mCherry* strain would allow direct assessment of whether septin disruption alters filopodial number, length, or dynamics. Alternatively, if rosette filopodia could be resolved through phalloidin staining, comparing stained wild-type and *Sros_septA*$^{1–50}$ rosettes may be sufficient to begin to explore this question.

Additional insights into the rosette integrity defect may come from septin mutant phenotypes that separate cytokinesis defects from effects on rosette organization. For example, tagged *Sros*_SeptA strains had normal cell size but altered rosette development in Chapter 2 (Figure 2.S4D-F), suggesting that these phenotypes can be uncoupled. Further analysis of these strains could focus on cellular phenotypes during rosette morphogenesis, including spindle positioning during division, cell positioning within the colony, ECM secretion, and the strength of cell-cell or cell-ECM attachment. If ECM production appears normal but cells fail to maintain stable positioning within the colony, this would support a model in which septins contribute directly to rosette cohesion rather than indirectly through cytokinesis defects. This model could be tested further through targeted mutations or a deletion series designed to separate septin roles in cytokinesis from their roles in multicellular organization. Together, these approaches would help define how septins may help coordinate cell division with multicellular development. More broadly, these future directions would help test whether septin functions in cytokinesis, cortical organization, and multicellular morphogenesis were already coordinated in the choanozoan stem lineage.

To further detail septin cytoskeletal organization in choanoflagellates, future experiments could explore whether *Sros*_SeptA localization depends on other septins. Strains that combine fluorescently-tagged *Sros*_SeptA with disruption of *Sros_septB*, *Sros_sept6*, or *Sros_sept9* would help determine whether *Sros*_SeptA localizes independently or instead requires other septins for stable recruitment to cytokinetic and other cortical sites. This approach could be expanded by generating additional fluorescently tagged septins and septin mutants with targeted changes in regions that mediate protein-protein interactions, including the GTPase domain, N- and C-terminal regions, and coiled-coil domain. These experiments would also help distinguish whether the phenotypes caused by septin disruption reflect loss of individual septin functions or broader defects in septin complex assembly.

This work suggests that septins may have served ancestral functions that later became important to animal cells. Because septins regulate cytokinesis in both animals and fungi, an ancestral role for septins in cytokinesis in the opisthokont lineage is likely (Mostowy and Cossart, 2012). However, the localization of *Sros*_SeptA to the cleavage furrow and nascent intercellular bridges in choanoflagellates, together with its demonstrated role in *S. rosetta* cytokinesis, supports the idea that septins regulated both membrane ingression and intercellular bridge maturation within a

more animal-like cortical environment before animal origins (Balasubramanian *et al.*, 2004). *Sros*_SeptA localization to putative basal filopodia further raises the possibility that septins also contributed to cortical organization or actin-based protrusions in the choanozoan stem lineage, especially in light of septin roles in regulating animal filopodia (Radler *et al.*, 2023). This possibility is also supported by previous work suggesting that septins and actin co-localize at membrane blebs in amoeboid *S. rosetta* cells, a role septins also play in modern animal cells (Gilden *et al.*, 2012; Brunet *et al.*, 2021). Additionally, the basal localization observed here and in previous work (Booth *et al.*, 2018) suggests that septins are organized with respect to apicobasal polarity in *S. rosetta*, reminiscent of septin localization and function during apicobasal organization in animal epithelia (Fares *et al.*, 1995; Spiliotis *et al.*, 2008; Bowen *et al.*, 2011). Additional insights into the ancestral functions of septins will require more detailed molecular investigation, but this work suggests that septins may have already been positioned at cellular structures relevant to both division and multicellular organization in the animal stem lineage.

Appendix 1 Materials and Methods

S. rosetta strains and culture conditions

All experiments were performed using strains of *S. rosetta* co-cultured with *Echinicola pacifica* bacteria (strain designation: *SrEpac*) (Levin and King, 2013). Wild-type *SrEpac* cells were used for Figure A1.1A. *Sros_septA-ALFA* cells were used for Figure A1.1B–B" and Figure A1.1C. Development of the *Sros_septA-ALFA* strain, which tagged *Sros*_SeptA with an ALFA epitope at amino acid position 392, is described in Chapter 2 ("CRISPR guide RNA and repair template design" methods section).

All strains were maintained as described in "Choanoflagellate culturing" in Chapter 2 methods. Briefly, cells were grown in low nutrient media (LNM), passaged every two days at a 1:500 dilution into fresh LNM, and supplemented with 0.4% (v/v) of a 10 mg/mL *E. pacifica* food pellet. Cultures were maintained at 22°C and 60% humidity, and experiments were performed using cells grown under these conditions and collected in mid-log phase.

Fixation, staining, and imaging intercellular bridges

To visualize intercellular bridges in both *SrEpac* and *Sros_SeptA-ALFA* cells for Figure A1.1A and Figure A1.1B–B", respectively, 20 mL of uninduced culture was grown to early log phase, which contained the greatest number of chain colonies. Thirteen mL of culture was gently added to a 15 mL Falcon tube and concentrated by low-speed centrifugation (600 × g for 5 min) using a swinging-bucket rotor centrifuge. To avoid disturbing the loose pellet, 10 mL of supernatant was removed and a 200 µL aliquot was then gently aspirated directly from the pellet using a wide-bore 200 µL tip. The aspirated pellet was then transferred to a poly-D-lysine-coated 96-well plate to preserve chain and intercellular bridge structures.

Cells were fixed directly in the chamber using 6% acetone, 4% PFA, and 1:300 phalloidin conjugated to Alexa Fluor 488 (Life Technologies, Cat. No. A12379) in PBS at room temperature for 15 min in the dark. Acetone, PFA, and phalloidin were added simultaneously because this combination, along with gentle culture handling, preserved a higher number of intercellular bridges in chain colonies compared with previously established fixation protocols (Booth *et al.*, 2018), potentially due to phalloidin stabilizing intercellular bridge structures, which often contained F-actin.

Following fixation, wells were either imaged immediately as described below (Figure A1.1A; *SrEpac* cells stained only with phalloidin) or washed twice with PEM and then incubated in permeabilization buffer (1% [w/v] bovine serum albumin-fraction V; 0.3% [v/v] Triton X-100 in PEM) on a shaker at 300 rpm for 30 min (Figure A1.1B–B"; *Sros_SeptA-ALFA* cells, to be co-stained with anti-ALFA nanobody). *Sros_SeptA-ALFA* cells were then incubated with 12.5 nM anti-ALFA nanobody conjugated to Alexa Fluor 657 on a shaker at 300 rpm for 1 h.

After antibody staining, *Sros_SeptA-ALFA* cells were washed three times with PEM. Cells were imaged immediately using a Nikon Ti2 inverted microscope (Nikon Instruments) with a Yokogawa CSU-W1 spinning disk confocal unit and a Hamamatsu ORCA-Flash4.0 C14440-20UP CMOS camera (Hamamatsu Photonics) equipped with a Plan Apo λ 100× oil immersion objective. Fluorescent images were collected using 488 nm excitation with a FITC emission filter

(phalloidin-labeled F-actin) for *SrEpac* and Sros_SeptA-ALFA cells, and 647 nm excitation with a Cy5 emission filter (*Sros*_SeptA-ALFA) for *Sros_SeptA-ALFA* cells only. In both Figure A1.1A and Figure A1.1B–B'', Z-stacks were acquired at 0.2 µm intervals and maximum-intensity projections were generated from a total Z-depth of 1 µm.

Fixation, staining, and imaging putative filopodia

To visualize putative filopodia in *Sros_SeptA-ALFA* cells for Figure A1.1C, cells were fixed as described in the first part of "Immunostaining and imaging SeptA-ALFA" in Chapter 2 methods, with changes to the staining conditions. One minute before fixation, 1 µg/mL FM 1-43FX dye (Thermo Fisher Scientific, Cat. No. F35355) was added to the cultures to label membranes. Cells were stained with 12.5 nM anti-ALFA nanobody conjugated to Alexa Fluor 657 (NanoTag Biotechnologies, Cat. No. N1502-AF647-L) as described in "Immunostaining and imaging SeptA-ALFA," and 1:300 phalloidin conjugated to Alexa Fluor 488 (Life Technologies, Cat. No. A12379) was added to label F-actin immediately before imaging, without a subsequent wash, because background fluorescence was low under these conditions and the signal was strongest when samples were stained immediately before imaging.

Stained cells were then imaged as described above in "Fixation, staining, and imaging intercellular bridges," with the addition of collecting FM 1-43FX-stained membrane images with 488 nm excitation and a TRITC emission filter. For Figure A1.1C images, Z-stacks were acquired at 0.2 µm intervals, and maximum-intensity projections were generated from a total Z-depth of 1 µm.

Appendix 1 Figures

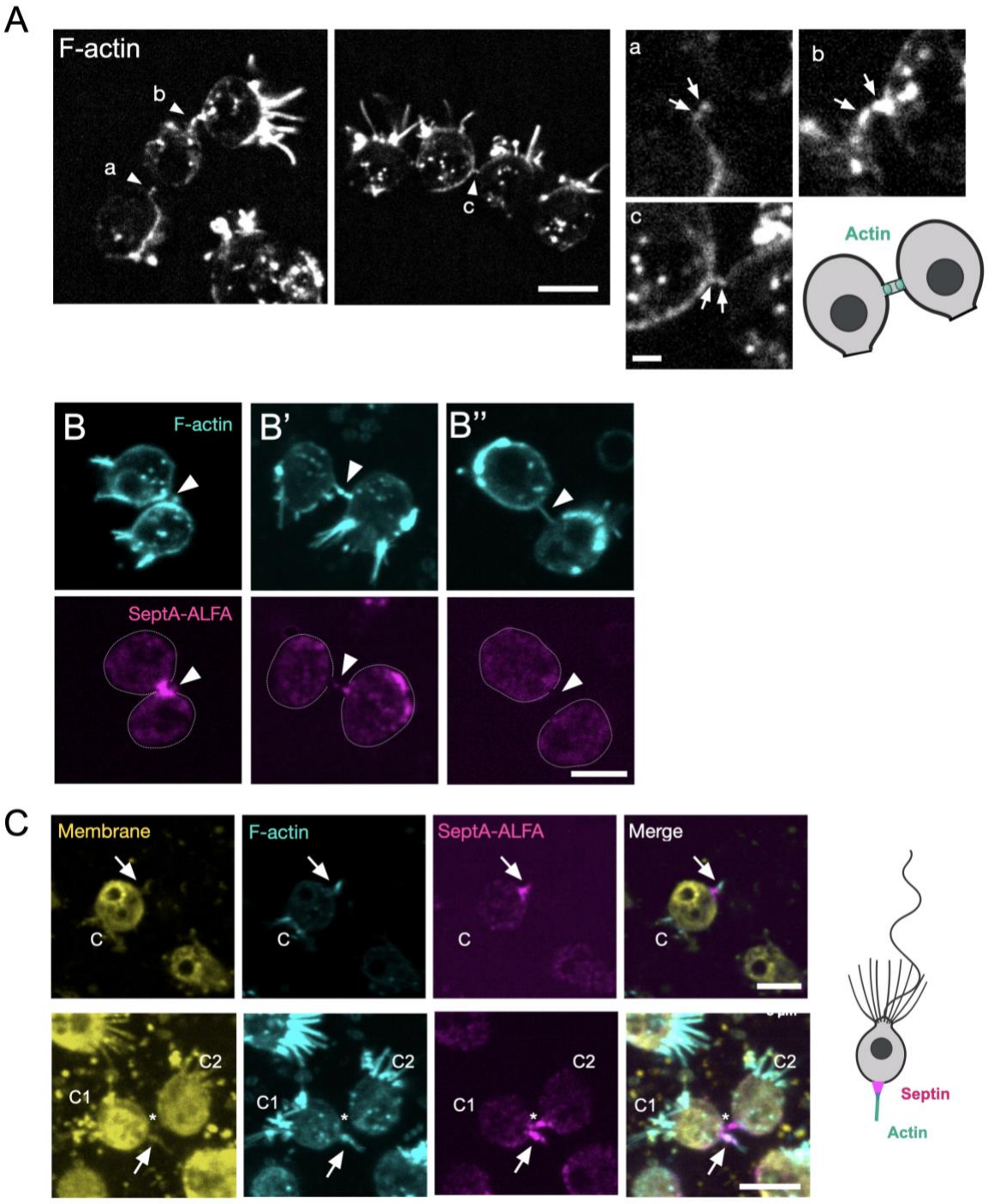

Figure A1.1: *Sros*_SeptA and actin localize to the intercellular bridge and putative basal filopodia of *S. rosetta* single cells and chains. (A) Actin localizes to the intercellular bridges in *S. rosetta* chains, often forming a doublet pattern of puncta or short bars on either side of the bridge. Two representative images of fixed *S. rosetta* chains are shown. Arrowheads indicate F-actin enrichment at the intercellular bridge. Insets a, b, and c show enlarged examples of intercellular bridges with arrows denoting doublet localization pattern. Actin is labeled with phalloidin. Scale bar, 5 μm in the main images and 1 μm in insets a, b, and c. A depiction of actin localization at the intercellular bridge between two cells is illustrated. (B-B") F-actin and *Sros*_SeptA both localize to bridges, but their relative enrichment varies. Arrowheads indicate the intercellular bridge. Actin is labeled with phalloidin (teal) and *Sros*_SeptA-ALFA is labeled with anti-ALFA nanobody (magenta). Scale bar, 5 μm. (C) *Sros*_SeptA and actin localize to filopodia-like structures at the basal cell pole. Representative images are shown. Arrows indicate protrusive basal structures positive for F-actin and *Sros*_SeptA-ALFA. The schematic to the right shows a possible model in which *Sros*_SeptA localizes near the base of the putative filopodium, while F-actin localizes along the protrusion. Actin is labeled with phalloidin (teal); membrane is labeled with FM 1-43FX (yellow); and *Sros*_SeptA-ALFA is labeled with anti-ALFA nanobody (magenta). Collar positions are labeled with a C within the image, with C1 and C2 indicating the two collars of the two cells shown. Scale bar, 5 μm.

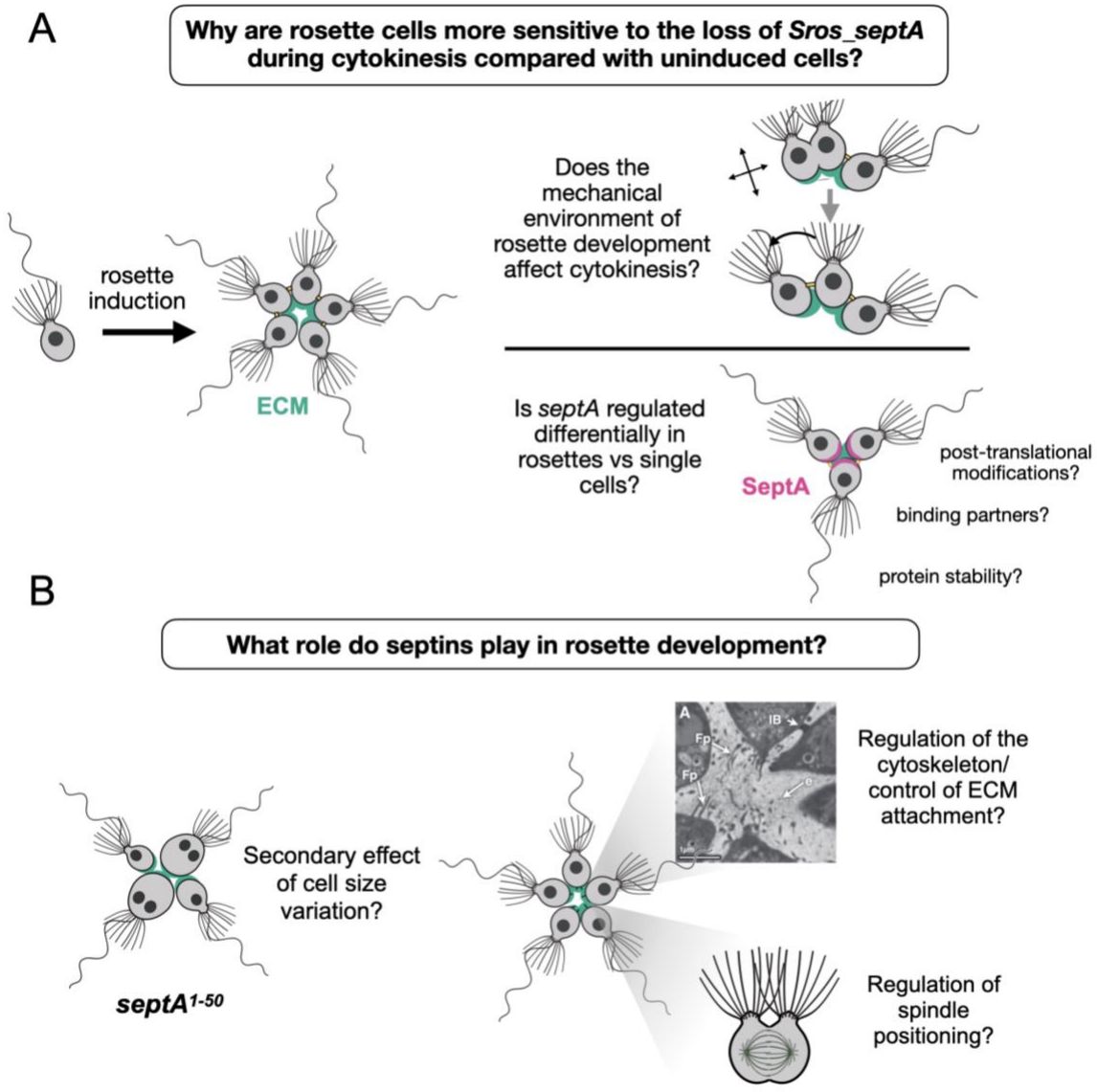

Figure A1.2. Future directions for septin research in *S. rosetta*. (A) Models proposed for why rosette cells are more sensitive to loss of *Sros_septA* during cytokinesis than uninduced cells. Rosette induction may alter the mechanical environment of cytokinesis through ECM-based attachment, or *Sros*_SeptA may be regulated differently in rosettes than in single cells. Top: black arrows indicate possible cell-ECM and cell-cell forces within a rosette; the black curved arrow represents post-division movement required for proper rosette morphogenesis. (B) Possible roles for septins during rosette development. Septin disruption may affect rosette integrity indirectly through changes in cell size, or more directly through regulation of the cytoskeleton, cell-ECM attachment, or spindle positioning. Image is adapted from Dayel *et al.* (2011): *S. rosetta* rosette colony midsection, thin-section TEM micrograph; Fp, filopodia; IB, intercellular bridge; e, extracellular matrix. Scale bar, 1 μm.

Appendix 2

Characterization of "Solo", an *S. rosetta* mutant that is unable to form chain or rosette colonies

Introduction

Chapter 1 introduced septins as candidate regulators of cytokinesis in multicellular contexts, and Chapter 2 tested this possibility directly. A complementary approach to exploring the connection between cell division and multicellular development is to start with a mutant phenotype rather than a candidate gene family. Forward genetic screens in *S. rosetta* have identified several genes required for rosette development, demonstrating the value of unbiased approaches for discovering mechanisms of multicellularity in choanoflagellates (Levin *et al.*, 2014; Wetzel *et al.*, 2018). This appendix focuses on one such mutant, Solo, which is relevant to this thesis because it appears to disrupt the transition from cell division to clonal development.

Solo has a general defect in clonal multicellularity (Figure 1.4D"; Levin *et al.*, 2014). Unlike wild-type cells, which readily form chain colonies under standard culture conditions and differentiate into rosettes upon induction (Dayel *et al.*, 2011), Solo exists primarily as a single-celled culture, only rarely forming cell doublets and never forming longer chains or rosettes (Levin *et al.*, 2014). This suggests that Solo, which is the only *S. rosetta* mutant with this class of phenotype, is defective in a cellular process required to maintain stable cell-cell connections following division. Chain and rosette colonies both arise through serial rounds of cell division and form colonies connected by persistent intercellular bridges, suggesting that Solo may provide a unique opportunity to probe mechanisms linking cytokinesis to multicellular organization. However, although the colony defect in Solo has been described in general terms and its genome has been sequenced, the specific point of failure in persistent cell-cell attachment and the causative mutation(s) underlying this phenotype remain unknown.

Results

To understand why Solo daughter cells separate after division rather than remain persistently attached, I observed Solo division events by time-lapse imaging. These movies revealed that cytokinesis produces two daughter cells that are initially connected by an intercellular bridge (Figure A2A). However, unlike wild-type cells, which often develop into chain colonies in which daughter cells remain stably connected and similarly oriented, Solo daughter cells frequently reorient after division. This reorientation is followed by bridge elongation and eventual breakage, causing the daughter cells to separate completely (Figure A2A). In most cases, bridge elongation was followed by cell separation. The reorientation shown in the model was common (Figure A2B), but varied in both direction and degree in the roughly dozen division instances observed. Future quantification will be needed to determine how consistently reorientation contributes to bridge elongation and cell separation in Solo.

Another approach to discovering the mechanistic basis of the Solo phenotype is by identifying the gene(s) responsible. The Solo genome was previously sequenced through unpublished work by former King lab graduate students Kayley Hake and Laura Wetzel. Laura then compared the Solo to a reference genome, performed the initial variant calling, and identified 23 coding-sequence mutations as possible candidates for the causative mutation (Table A2.1). At Laura's suggestion, candidate mutations were prioritized by variant-call quality score and read coverage, features that had previously helped distinguish genuine mutations from false positives in King lab forward genetic screens (Wetzel *et al.*, 2018). Each candidate was evaluated by PCR

amplification and Sanger sequencing of the candidate genomic region. The eight mutations with the highest variant-call quality scores were tested. Of these, six were false positives and two were confirmed. Two additional putative coding-sequence mutations, within the gene models PTSG_10591 and PTSG_12024, were also tested because BLASTP searches using their predicted protein sequences returned hits to nexin and Cep164, respectively, gene types that could both plausibly be involved in cell division. However, both mutations were determined to be false positives following genotyping. Because the remaining candidate mutations had either low variant-call quality scores or low read depth, and because previous King lab forward genetic screens have suggested that background mutation rates are generally low in *S. rosetta* mutants (Levin et al., 2014; Wetzel et al., 2018), the two confirmed mutations represent the current strongest candidates for the causative mutation in Solo.

The first confirmed mutation is a 19-bp deletion in PTSG_08492 that introduces a frameshift near the C-terminus of the predicted protein (Figure A2C). The predicted protein is 1,698 amino acids in length with a predicted microtubule-binding domain (PF04212), a predicted septin GTPase domain (PF00735), and a RasGEF domain (PF00617), suggesting a potential role in cytoskeletal organization or signaling. However, while BLASTP searches recovered a potential homolog in *M. brevicollis*, non-choanoflagellate hits aligned over only small fractions and were mostly RasGEF-domain-containing proteins. The second mutation is a point mutation in PTSG_06868 that introduces a premature stop codon near the middle of the predicted coding sequence; this gene, encoding a predicted 762-amino-acid protein, does not contain any annotated domains and did not recover any hits with a BLASTP search, making its potential function unclear (Figure A2C'). To test whether either mutation is causative, I used CRISPR/Cas9-based genome editing to attempt to either (1) recapitulate the Solo mutations or (2) introduce early truncations in each candidate gene. Despite multiple attempts, these experiments did not yield successful edits (Figure A2C; Table A2.2), preventing direct validation of candidate gene function.

Discussion

Solo represents an opportunity to study the regulation of multicellular development in *S. rosetta* starting from an unbiased genetic screen. The results presented here identify two key features of Solo. First, time-lapse imaging showed that Solo cells complete cytokinesis and initially form an intercellular bridge, but often fail to maintain this connection after division. Instead, daughter cells frequently reorient, the bridge elongates, and the cells eventually separate (Figure A2A and B). Second, follow-up analysis of candidate mutations identified two confirmed coding-sequence mutations, including one in PTSG_08492, which encodes a predicted protein with cytoskeletal and signaling domains (Figure A2C and C'). Together, these results suggest that Solo disrupts the transition from cell division to stable multicellular organization, rather than blocking bridge formation outright.

The cellular basis of this defect remains unknown. Solo may affect spindle orientation or division plane positioning, or another earlier step in cytokinesis that only becomes apparent after division. Alternatively, Solo may affect a later step in bridge maturation, stabilization, or maintenance. Distinguishing between these possibilities will require quantitative analysis of division orientation, daughter-cell reorientation, bridge elongation, and bridge breakage.

Resolving the genetic basis of Solo will be important for future mechanistic work. The two confirmed candidate mutations provide possible entry points. Most promising is the discovery of a confirmed mutation in the PTSG_08492, which encodes a protein with predicted cytoskeletal and signaling domains. The predicted septin GTPase domain is intriguing, although its 1,698-amino-acid length and domain organization are markedly unlike canonical septins and it remains unclear what role, if any, this predicted protein has in interacting with the septin cytoskeleton. Together with the predicted microtubule-binding and RasGEF domains, however, this domain architecture raises the possibility that the protein product of PTSG_08492 participates in cytoskeletal organization or signaling during cytokinesis or bridge stabilization.

Because CRISPR/Cas9 editing did not successfully recapitulate either mutation or generate early truncations in the candidate genes, the causative mutation remains unvalidated. One possibility is that early truncations in either gene are lethal, while the editing cargo used to recreate the Solo mutations, which are presumably non-lethal, may have failed because of inefficient gRNA activity at that target. Future work could use alternative CRISPR/Cas9 strategies in *S. rosetta*, especially given recent improvements to electroporation efficiency (Nguyen *et al.*, 2026) and alternative editing approaches (Combredet *et al.*, 2025). In addition, these genes could be fluorescently tagged either by introducing transfected constructs or by using the endogenous tagging method I developed in Chapter 2. As an initial test, localization patterns could provide clues about protein function. Together, future work that combines improved genome editing with quantitative analysis of bridge formation, daughter-cell re-orientation, bridge extension, and bridge breakage should help determine how Solo disrupts intercellular bridge stability and identify basic cellular processes required for clonal multicellularity in *S. rosetta*.

Appendix 2 Materials and Methods

S. rosetta strains and culture conditions

The Solo mutant, a previously isolated *S. rosetta* mutant (Levin *et al.*, 2014), was used for the time-lapse imaging experiment shown in Figure A2A. Solo was maintained as described in "Choanoflagellate culturing" in Chapter 2 methods. Briefly, cells were grown in low nutrient media (LNM), passaged every two days at a 1:500 dilution into fresh LNM, and supplemented with 0.4% (v/v) of a 10 mg/mL *E. pacifica* food pellet. Cultures were maintained at 22°C and 60% humidity, and experiments were performed using cells grown under these conditions and collected in mid-log phase.

Time-lapse imaging of Solo cell division

Time-lapse imaging of Solo cell division was performed as described for "Imaging and quantifying cytokinesis failure in slow swimmers and rosettes" in Chapter 2, except that cells were imaged without RIF-OMV treatment and at higher magnification. Briefly, Solo cells were diluted to 150,000 cells/mL and gently vortexed for 5 s on low speed. A 200 µL aliquot of diluted culture supplemented with 2 µL *E. pacifica* food pellet was added to the center of a poly-D-lysine-coated FluoroDish. FluoroDishes were washed three times with ASW before use, and the final wash was left in place for 30 min. Then, 1.5 mL of Anti-Evaporation Oil was layered on top of the 200 µL culture droplet, and cells were allowed to settle for 10 min at 22°C.

Cells were imaged using DIC time-lapse microscopy on a Zeiss Axio Observer Widefield microscope equipped with a Plan-Apochromat 63×/1.40 Oil DIC M27 objective. A single field of view with a high density of cells was chosen for each experiment, and images were collected at 30 s intervals for 6 h. A representative division event was selected for Figure A2A. This experiment was repeated on multiple days with multiple objective magnifications, and the combined observations from these division events were used to describe the phenotype discussed in this appendix.

Solo genome sequencing and candidate mutation prioritization

The *S. rosetta* Solo mutant genome was previously sequenced through unpublished work by Kayley Hake and Laura Wetzel. Genomic DNA from Solo, originally named M18F12, was prepared by CsCl purification and sequenced on an Illumina HiSeq 2000 platform, generating 100-bp reads. Candidate mutations were identified by comparing the Solo mutant genome to the *S. rosetta* reference genome and generating variant-call files. The available VCF header indicates that variants were called using SAMtools v0.1.18, and predicted variant effects were annotated using SnpEff v3.4i. Variants unique to Solo were identified by comparison with variant-call files from other sequenced mutant strains. The resulting variant-call file was filtered for mutations predicted to affect coding sequences and for variants in which all or nearly all mapped reads supported the mutant allele. This filtered file contained 23 candidate coding-sequence mutations in Solo.

Candidate mutations were prioritized for follow-up based on variant-call quality score, read depth, and predicted functional relevance to the Solo phenotype. Rather than applying a strict numerical cutoff, candidates were ranked by variant-call quality score and inspected in that

order, with two additional candidates selected based on predicted functional relevance: PTSG_10591 and PTSG_12024, for which BLASTP searches returned hits to nexin and Cep164, respectively, both of which had plausible links to cell division or cytoskeletal organization. This strategy was based on prior King lab forward genetic screens, in which confirmed mutations were often associated with higher variant-call quality scores and read depths near the genome average. The highest-priority candidates that could be amplified reliably were then tested by PCR amplification and Sanger sequencing. Eight candidates were tested this way; six were false positives and two were confirmed. After these two mutations were confirmed (located within PTSG_06868 and PTSG_08492), further Sanger validation of lower-priority candidates was not pursued because additional candidates were lower-priority and several loci were technically difficult to amplify and sequence. Therefore, although unlikely, additional candidate mutations may remain among the untested lower-priority variants.

PCR amplification and Sanger sequencing of candidate mutations

PCR amplification and Sanger sequencing were used to genotype Solo at candidate mutation sites, following the approach described in Chapter 2 ("Genome editing" in Materials and Methods), with the following changes. Genotyping PCRs were performed individually in PCR tubes rather than as pooled genotyping reactions. For each candidate locus, primers were designed to amplify the genomic region surrounding the predicted mutation site, and PCR products were submitted for Sanger sequencing.

Unlike most CRISPR edit-site genotyping performed in Chapter 2, where one to three primer pairs were generally sufficient, several Solo candidate loci required many additional primer pairs to obtain usable sequence coverage across the predicted mutation site. This was especially common for candidate mutations that were later determined to be false positives. Therefore, candidate mutations were only considered confirmed when Sanger sequencing clearly supported the predicted mutant allele.

Protein domain annotation and homology searches

Protein domains were predicted using InterProScan, and homology searches were performed using NCBI BLASTP, following the approach described in Chapter 2 ("BLAST searches for septin genes" in Materials and Methods).

CRISPR/Cas9 attempts to validate Solo candidate mutations

To test candidate causative genes in Solo, CRISPR/Cas9 genome editing was attempted using the protocols described in "CRISPR guide RNA and repair template design" and "Genome editing" in Chapter 2 methods. gRNAs, repair oligonucleotides, and sequencing primers are listed in Table A2.2. For each target, edited populations were clonally isolated and screened by PCR amplification and Sanger sequencing of the target locus. In all cases, the target sites could be resolved by Sanger sequencing with the primers listed in Table A2.2, allowing the presence or absence of the intended edit to be assessed.

Table A2.2 also outlines the number of independent editing experiments and estimated number of clones sequenced per CRISPR/Cas9 gRNA/oligonucleotide repair pair. For PTSG_08492, four total gRNA/oligonucleotide pairs were tested: one pair was used in two independent attempts to re-introduce the Solo mutation, one pair was used in two independent attempts to introduce the

most N-terminal premature stop codon, and two additional pairs were each tested once to introduce premature stop codons at other sites. For PTSG_06868, three gRNA/oligonucleotide pairs were tested, with one independent editing attempt performed for each pair. No edited clones were recovered for either candidate gene. Because the target loci were successfully sequenced after editing, this negative result is most consistent with either failed editing/recovery of the intended alleles or reduced viability of cells carrying the engineered truncations, rather than failure to genotype the target sites.

Appendix 2 Figures and Tables

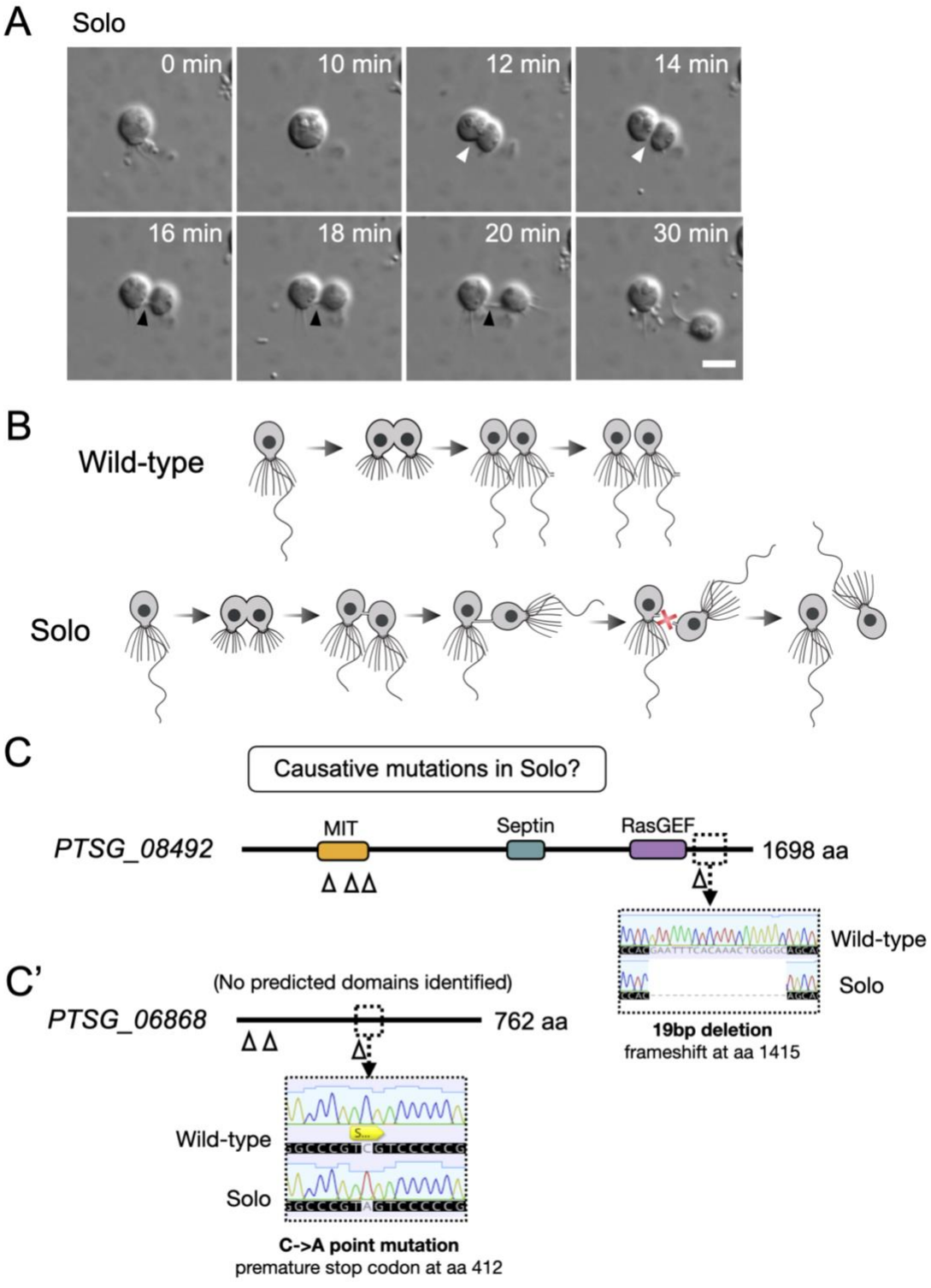

Figure A2. Solo creates intercellular bridges but often fails to maintain them, and two candidate mutations have been identified. (A) Time-lapse imaging showed that Solo daughter cells are initially connected by an intercellular bridge after cytokinesis, but in most observed cases the bridge later elongated and the cells separated. Re-orientation of the daughter cells after division was also common, although the direction and extent of re-orientation varied between events. One representative division is shown. White arrowheads indicate cleavage furrow ingression, and black arrowheads indicate the intercellular bridge after formation and during elongation before daughter-cell separation. Time is shown in minutes. Scale bar, 5 μm. (B) Model comparing wild-type and Solo colony formation. The re-orientation depicted is a simplified model of a common but variable behavior. (C–C') Two candidate mutations were confirmed in Solo. (C) PTSG_08492 contains a 19-bp deletion predicted to cause a frameshift near the C-terminus of a protein with predicted microtubule-binding, septin GTPase, and RasGEF domains. (C') PTSG_06868 contains a C-to-A point mutation predicted to introduce a premature stop codon in a protein with no annotated domains. Open triangles indicate CRISPR/Cas9 target sites tested for genome editing; however, successful edits have not yet been recovered.

Table A2.1. Two confirmed mutations in Solo among 23 candidate coding-sequence mutations identified by variant calling. Two of the 23 candidate coding-sequence variants identified by variant calling were confirmed by follow-up PCR and Sanger sequencing. Candidates were initially prioritized based on variant-call quality score at the candidate site, as ordered above. Of the 23 candidates, two were confirmed, eight were false positives, and thirteen were not tested by Sanger-sequencing. Variant-call quality score refers to the Phred-scaled confidence of the variant call. Read depth indicates the number of reads covering the candidate site.

Variant-call quality score	Read depth (×)	Gene (PTSG_)	Sequencing results
222	208	6868	confirmed
214	174	2443	FALSE
214	94	7288	FALSE
214	205	8492	confirmed
146	108	2470	FALSE
88.5	73	2381	FALSE
74.6	15	4316	FALSE
66.6	12	10033	FALSE
44	84	10785	not sequenced
33.5	161	955	not sequenced
31.3	7	6612	not sequenced
19.3	128	10591	FALSE
16.3	30	2551	not sequenced
14.6	29	10148	not sequenced
14.4	10	2820	not sequenced
14.4	11	2956	not sequenced
12.5	143	11690	not sequenced
10.3	68	5035	not sequenced
9.01	3	8988	not sequenced
7.45	72	4154	not sequenced
5.77	183	12024	FALSE
3.96	7	12381	not sequenced
3.12	47	2823	not sequenced

Table A2.2: Nucleotide sequences for CRISPR/Cas9 editing of genes with potential causative mutations in Solo. *Exact clone numbers are estimates for pooled-clone experiments. For these experiments, cells from four plates were pooled when approximately 75% of wells contained growing clones. The estimated number of clones screened was calculated as: number of successfully sequenced wells per final pooled plate × 4 plates × 0.75.

Target / intended effect	crRNA sequence	Repair oligo sequence	Forward sequencing primer	Reverse sequencing primer	Independent editing attempts / # clones sequenced*
PTSG_08492 / replicate exact Solo mutation	CCAGTTTGTGAAATTCGTGG	GTGTTGCGTAACTGCAAGCAGGAGCGTGACTGGGAAGACTTTTTCCTGCTGTGGAGGAATCCCTGCCCACGCGTTTTGACCTGTCCTCAAACAAGGCGCG	TGGCAACCAACATGCTGCC	ACAGACGCGCCACAAACGC	2 / 528*
PTSG_08492 / KO	AATCTGTTGCAGGCGCTCAA	CAGCCAGGGCCACGTTGATGAGGCCGAGGATTTGTTCCAGGCAGCCTTTGTTTATTTAATTAAATAAAAGCGCCTGCAACAGATTAGCGAGCAGTCTGCTGACCGCCGCGACGCCCTC	ATTGTCGCCGCAGGCCG	TGCTGAGGGCTGAAGCAGC	2 / 510*
PTSG_08492 / KO	GCTGCTCGTTGCTGGTGAAG	AACAACAGCGGATCTGAGCGCGCAAGCAGCAGAGCTGCTCGTTGCTGGTGTTTATTTAATTAAATAAAAAGAGGCCCAAGCTCTTGAGAACTATGAGGAAGCCAAGGAGTGCTTCGTG	ATCGTTGGCGAGACAGCGTC	TGTGCCCGTGCTTCCTGC	1 / 246*
PTSG_08492 / KO	AGCCAAGGAGTGCTTCGTGG	TGAAGAGGCCCAAGCTCTTGAGAACTATGAGGAAGCCAAGGAGTGCTTCGTTTATTTAATTAAATAAATGGAGGCCGTCGACATCTTCTTTGAACTCGTGCGTGGTTTGTGTGTGTGT	ATCGTTGGCGAGACAGCGTC	TGTGCCCGTGCTTCCTGC	1 / 282*
PTSG_06868 / replicate exact Solo mutation	CATTGGCGAGTGCAAAACGG	GTTGCACCCTTCGAGCTACCCACTATCGTGCCGGCACTCATTGGCGAGTGCAAAACGGGGGACTACGGGCCGCCGCCGTGTTCACCATCGTCGCCACCGACAACGTCACT	GGTGCCGCAAGAAGACGTGG	ACATTGCGGCGGAGGCTG	1 / 51* (very few wells were successfully sequenced in pooled plate)
PTSG_06868 / KO	TTCTTCCCCGCTTTGTCGGA	TCATCTTCGGGCAGCGACTTGCGCTGTGTCTTCTTCTTCCCCGCTTTGTCTTTATTTAATTAAATAAAGGAGGGCGTCATGGTCATGAACCTGGAGACAACGGGTGATGGATGGAACG	AACTCGCACACGGCGACTTCA	TTGCCGTTCCGCTTTGGTGC	1 / 255*
PTSG_06868 / KO	TCGAAAAAGCAGGTGCACGA	TGCGACACGAGCTCAACAGCAGCAGACGCGGCGTCGAAAAAGCAGGTGCATTTATTTAATTAAATAAACGAGGGCTCGCTCTTCTGCCTGTATCCGGAGCTCGGCGAGGAGACGTTGG	AACTCGCACACGGCGACTTCA	TTGCCGTTCCGCTTTGGTGC	1 / 249*

Appendix 3

Investigating the functions of cadherins in *S. rosetta*

Introduction

Although this thesis has focused primarily on the connection between cell division and multicellular development, animal multicellularity depends on diverse mechanisms that extend beyond the regulation of cytokinesis, including cell signaling and adhesion (Brunet and King, 2017). Many genes involved in these processes have well-characterized roles in animals, but their ancestral functions remain less clear. Choanoflagellates encode homologs of many animal signaling and adhesion genes, providing a comparative framework for inferring their possible ancestral functions in the animal stem lineage. However, in many cases, their functions in choanoflagellates have not been directly tested (King *et al.*, 2003; Brunet and King, 2017). This appendix examines one such gene family, cadherins, to test how molecular systems associated with animal adhesion and signaling function in choanoflagellates.

Cadherins are a diverse family of transmembrane proteins best known for their roles in animal cell adhesion and signaling (Halbleib and Nelson, 2006). Animals encode many cadherin families, most notably classical cadherins, which mediate cell-cell adhesion in epithelial tissues through extracellular cadherin repeats and conserved cytoplasmic domains that connect with catenins to regulate the actin cytoskeleton (Shapiro and Weis, 2009). Genomic sequencing has revealed that choanoflagellates also encode large and diverse cadherin repertoires, including 29 predicted cadherins in *S. rosetta* (Abedin and King, 2008; Nichols et al., 2012). However, most choanoflagellate cadherins do not fall into animal cadherin subfamilies, suggesting that cadherin repertoires expanded largely independently in choanoflagellates and animals. For example, choanoflagellates do not encode recognizable classical cadherin genes (Figure A3.1A). Despite the abundance of cadherins in choanoflagellates and their critical roles in animal development, their functions in choanoflagellates remain largely unknown. Studying choanoflagellate cadherins may therefore help distinguish whether this gene family had related functions in animal ancestors, or whether cadherins were later co-opted into animal-specific developmental roles. This appendix begins to test that possibility by examining the function of two *S. rosetta* cadherin families, Hedglings and SH2-type cadherins (Figure A3.1A-C).

Hedgling cadherins are found throughout choanoflagellates and in some early-branching animals, including sponges and cnidarians, and contain a Hedge domain similar to the N-terminal signaling domain of animal Hedgehog proteins (Figure A3.1A-C; Adamska *et al.*, 2007; Nichols *et al.*, 2012). However, Hedgling function has not been directly tested in choanoflagellates, and studies in early-branching animals remain limited to sequence analysis and developmental expression. In the sponge *Amphimedon*, Hedgling is expressed in a posterior band associated with pigment ring formation (Adamska *et al.*, 2007), while in the cnidarian *Nematostella* it is expressed in endodermal domains (Matus *et al.*, 2008), suggesting possible roles in cell-cell communication or developmental patterning but without clear evidence for a defined cellular function.

SH2-type cadherins, by contrast, are absent from animals (Figure A3.1A). However, they appear to be broadly conserved in choanoflagellates (Figure A3.1B). Unlike many choanoflagellate cadherins, SH2-type cadherins contain a predicted intracellular domain: an SH2 (Src-homology 2) domain, which could link extracellular interactions to phosphotyrosine signaling (Waksman *et al.*, 2004; Figure A3.1C; Abedin and King, 2008; Nichols *et al.*, 2012). In *M. brevicollis*,

antibodies recognizing SH2-type cadherins suggested localization to the microvillar collar, and SH2-type cadherin protein abundance varied with both the type and amount of bacteria used as food during preliminary western blot experiments (Abedin and King, 2008; Abedin, 2010).

S. rosetta provides an interesting system for testing cadherin function because it undergoes several behaviors that could plausibly involve adhesion or cell-surface signaling. These include clonal colony development in chains and rosettes, aggregation in response to environmental cues, bacterial prey capture with an actin-rich collar, and attachment to extracellular matrix or substrates during different life-history stages (Dayel *et al.*, 2011; Dayel and King, 2014; Woznica *et al.*, 2017). However, because the cellular functions of choanoflagellate cadherins are essentially unknown, these processes represent exploratory starting points rather than established roles.

Results

To begin testing the functions of cadherins in *S. rosetta*, I focused on Hedgling cadherins and SH2-type cadherins. *S. rosetta* encodes two Hedglings, here called *Hedgling* and *LrgHedgling*, and three SH2-type cadherins, here called *Sros_SH2CD1*, *Sros_SH2CD2*, and *Sros_SH2CD3* (Figure A3.1C). Using CRISPR/Cas9-mediated genome editing, I introduced premature stop codons near the N terminus of the predicted proteins encoded by both Hedgling genes, creating both individually edited strains and a *Hedgling*; *LrgHedgling* double-edited strain. I also edited each of the three SH2-type cadherin genes individually (Figure A3.1C), but not combinatorially. In all cases, the premature stop codons were introduced before annotated domains, including the transmembrane domain, and are therefore likely to have generated strong loss-of-function alleles. The resulting alleles are named in Figure A3.2 after the number of amino acids predicted to remain after insertion of the premature termination sequence (e.g. the $Hedgling^{1\text{-}10}$ allele is predicted to encode the N-terminal 10 amino acids).

I first tested whether cadherin disruption affected cell proliferation. Growth curves did not reveal obvious differences between wild-type cultures and Hedgling mutants (Figure A3.2A). *Sros_SH2CD1* and *Sros_SH2CD2* mutant cultures showed a modest trend toward higher cell densities than wild-type during growth, but additional replicates followed by statistical analyses will be required to determine whether this represents a reproducible phenotype (Figure A3.2A'). Together, these data suggest that, under standard laboratory conditions with abundant *E. pacifica* food provided at the start of the experiment, these cadherins are not individually required to maintain near-wild-type proliferation.

I next examined whether cadherin mutants had obvious defects in chain or rosette development. Preliminary imaging did not reveal obvious defects in chain formation, rosette formation or rosette integrity in either single or double Hedgling mutant strains, or in one SH2-type cadherin mutant, $Sros\_SH2CD1^{1\text{-}13}$ (Figure A3.2B). The other two individual SH2-type cadherin knockout strains have also been examined qualitatively, and no obvious colony morphology defect has been observed. Although these phenotypes have been consistent over multiple rounds of observed rosette induction experiments, additional replicate-level data along with quantitative analysis will be necessary to see if subtler defects are present and ensure these phenotypes are robust across replicates.

Because cadherins could also contribute to other *S. rosetta* behaviors, I preliminarily examined additional phenotypes. In a pilot experiment, chondroitinase-induced swarming was tested in both the single and double Hedgling mutant strains, but the swarming response appeared similar in these mutants compared with wild-type (Figure A3.2C, white arrows). However, additional replicates will be necessary to confirm these observations. I also used FM 1-43 staining to examine collar morphology in the *Hedgling* mutant (Figure A3.2D). These images did not reveal a dramatic defect in collar organization. In the future, this assay could be developed further to quantify microvillar number, spacing, collar width, or overall collar organization. Therefore, although no clear cadherin mutant phenotype has been identified so far, these strains provide a foundation for more targeted tests of cadherin function.

Discussion

These preliminary experiments did not identify an obvious requirement for Hedgling or SH2-type cadherins in *S. rosetta* growth, rosette formation, rosette integrity, chondroitinase-induced swarming, or gross collar morphology. This result suggests that the mutant strains tested so far are not obviously defective in several major laboratory-observable behaviors under the conditions tested. However, because choanoflagellate cadherins remain largely uncharacterized, and because combinatorial knockouts in these families have either not been made or fully tested, the absence of an obvious phenotype should be interpreted cautiously. These genes may act redundantly, function only under specific environmental conditions, or regulate more subtle cellular processes that were not captured by the initial assays presented here.

One clear next step is to test for redundancy, especially among SH2-type cadherins. *S. rosetta* encodes three SH2-type cadherins, but only individual mutant strains have been generated so far. Generating double and triple mutants would provide a more convincing test case of whether this family contributes to functions in collar organization, bacterial interactions, or signaling. This is especially important because prior work in *M. brevicollis* suggested that SH2-type cadherins localize to the microvillar collar and vary in abundance depending on bacterial food source (Abedin and King, 2008; Abedin, 2010). Functional redundancy is additionally complicated by the large number of cadherins encoded in the *S. rosetta* genome. An additional approach would be to begin editing the remaining 24 cadherins in *S. rosetta*, beginning with families of conservation or interesting domain architecture (Nichols *et al.*, 2012), to expand the repertoire of mutants to test for cadherin function.

Future studies may benefit from focusing on three broad classes of hypothesized cadherin functions: intracellular organization, bacterial interactions, and intercellular interactions (Figure A3.3). First, cadherins may influence collar structure or organization, either through direct effects on microvilli or through links between extracellular interactions and intracellular signaling. This hypothesis is supported by the previously reported localization of cadherins to the collar in *M. brevicollis* (Abedin and King, 2008) and the roles of protocadherins in microvillar adhesion in the intestinal brush border of vertebrate epithelial cells (Crawley *et al.*, 2014). This could be tested by quantifying collar width, microvillar number, microvillar spacing, and collar symmetry in wild-type and cadherin mutant strains using similar methods to my preliminary collar imaging (Figure A3.2D). Second, cadherins may contribute to bacterial recognition, prey

capture, or feeding efficiency, as suggested by both the preliminary SH2-type cadherin expression data presented in Abedin's dissertation (2010) and by the existing interactions of bacteria and cadherins during bacterial pathogenesis in mammalian cells (Mengaud *et al.*, 1996). These possibilities could be tested by first expanding the growth assay conditions to include different types and amounts of bacteria. Third, cadherins may contribute to cell-cell or cell-ECM interactions during clonal colony formation, aggregation, or substrate attachment, given the well-studied roles of cadherins in cell-cell interactions in animals (Halbleib and Nelson, 2006; Brasch *et al.*, 2012). Although no obvious rosette defect was observed in the initial assays, more quantitative measurements of colony size, cell packing, rosette shear resistance, aggregation efficiency, and attachment behavior may reveal phenotypes not apparent from qualitative imaging.

Together, these results establish a starting point for functional analysis of cadherins in *S. rosetta*. The absence of strong phenotypes in the initial assays suggests that Hedgling and SH2-type cadherins are not individually essential for growth or obvious multicellular development under standard laboratory conditions. At the same time, the diversity of possible cadherin functions in choanoflagellates means that these experiments should be viewed as an initial screen rather than a definitive test. Future work guided by the candidate functions outlined in Figure A3.3 may help determine whether choanoflagellate cadherins regulate collar organization, bacterial interactions, signaling, or adhesion, and whether any of these functions illuminate how cadherin families were deployed before the origin of animal development.

Appendix 3 Materials and Methods

Phylogenetic searches for Hedgling and SH2-type cadherins in choanoflagellates

InterProScan (Jones *et al.*, 2014), which detects Pfam domains through Hidden Markov Model-based searches performed with HMMER, was used to identify predicted protein domains in choanoflagellate proteomes to determine the presence or absence of Hedglings and SH2-type cadherins in Figure A3.1A and B. To identify candidate cadherin-domain-containing proteins, InterProScan output files were searched for proteins containing extracellular cadherin repeat domains, defined by the SMART cadherin domain accession SM00112. Custom R scripts were then used to extract all SM00112 domain coordinates from the InterProScan output and retrieve the corresponding amino acid sequences from the original protein FASTA files. To identify candidate Hedgling and SH2-type cadherins, the same SM00112-containing proteins were filtered for the presence of either a Hedgling domain (PF01085) or an SH2 domain (SM00252), respectively. Hedglings were defined as genes containing both SM00112 and PF01085 domains while SH2-type cadherins were defined as genes containing both SM00112 and SM00252 domains.

S. rosetta strains and culture conditions

All experiments were performed using strains of *S. rosetta* co-cultured with *Echinicola pacifica* bacteria (strain designation: *SrEpac*) (Levin and King, 2013). *S. rosetta rpl36a* cells and the cadherin mutant strains described below were used for the experiments in Appendix 3. The *rpl36a* control and cadherin mutant strains were generated by CRISPR/Cas9-mediated gene disruption, as described in "CRISPR/Cas9 disruption of cadherin genes".

All strains were maintained as described in "Choanoflagellate culturing" in Chapter 2 methods. Briefly, cells were grown in low nutrient media (LNM), passaged every two days at a 1:500 dilution into fresh LNM, and supplemented with 0.4% (v/v) of a 10 mg/mL *E. pacifica* food pellet. Cultures were maintained at 22°C and 60% humidity, and experiments were performed using cells grown under these conditions and collected in mid-log phase.

CRISPR/Cas9 disruption of cadherin genes

For CRISPR editing of cadherin genes, the protocol outlined in "CRISPR guide RNA and repair template design" and "Genome editing" Chapter 2 methods was followed. gRNAs, repair oligonucleotides, and sequencing primers are listed in Table A3.

Growth curves

Growth curves in Figure A3.2A and A' were performed as described in Chapter 2 ("Growth curves" methods section), with the following changes: Cells were instead grown in high nutrient media (HNM), described in Chapter 2 ("Choanoflagellate culturing" methods section) because HNM was the standard growth condition used in the lab and in previous *S. rosetta* growth experiments (Booth et al., 2018) when these experiments were performed. As discussed in Chapter 2, later experiments used low-nutrient media because it reduced bacterial biofilm formation in some cases.

In Figure A3.2A, cells were seeded at an initial density of 50,000 cells/mL and supplemented with 400 µg/mL *E. pacifica* food pellet, while in Figure A3.2A' cells were seeded at an initial

density of 5,000 cells/mL and supplemented with 66.7 µg/mL *E. pacifica* food pellet. Cells were prepared and washed as described in Chapter 2, and 500 µL of culture was aliquoted into each well of a 24-well plate (Fisher Scientific, Cat. No. 09-761-146) and incubated at 22°C and 60% humidity. Plates were maintained in a covered plastic container with dampened paper towels and the lid loosely affixed to minimize evaporation while allowing gas exchange.

Every 12 h, starting at 0 h and continuing for 84 h, three technical replicate wells per strain were fixed with 10 µL of 16% paraformaldehyde (Thermo Fisher Scientific, Cat. No. 50-980-487) and stored at 4°C. After all timepoints were collected, wells were mixed, 10 µL was removed, and then counted on a Luna cell counter (Logos Biosystems, Cat. No. L20001).

Imaging of single cells, chains, and rosettes in wild-type and cadherin mutant cells
To image *S. rosetta* wild-type and cadherin mutant cultures shown in Figure A3.2B, cultures were grown for 24 h in six-well plates (Thermo Fisher Scientific, Cat. No. 140675) (2 mL per well) with or without RIF-OMVs. For RIF-OMV-induced cultures subjected to shear, cultures were vortexed for 15 s at high speed using a Vortex Genie 2 (Scientific Industries) in a 15 mL Falcon tube (Corning, Cat. No. 352196) before imaging.

For each strain and condition, 1 mL of culture was gently concentrated by low-speed centrifugation (600 × g for 2 min) using a swinging-bucket rotor centrifuge. To avoid disturbing the loose pellet, the supernatant was left in place and a 200 µL aliquot was gently aspirated directly from the pellet using a wide-bore 200 µL tip and transferred to a poly-D-lysine (Millipore Sigma, Cat. No. P6407) coated 96-well plate (Thermo Fisher Scientific, Cat. No. 167008). The gentle centrifugation and transfer preserved chain and rosette structures while concentrating cells for ease of imaging. Cells were allowed to settle for 10 min at 22°C before live imaging by differential interference contrast (DIC) microscopy on a Zeiss Axio Observer Widefield microscope equipped with a Plan-Apochromat 40×/1.1 W Korr UV VIS IR water immersion objective with a 2.5× Optovar setting.

Chondroitinase treatment
Wild-type, *Hedgling*, and *LrgHedgling* mutant cultures were prepared at 1×10^6 cells/mL in high nutrient media and plated in uncoated 8-well Ibidi plates. Cells were treated with either 0.01% BSA carrier control or 0.1 U/mL chondroitinase, diluted from a 5 U/mL stock. For each condition, 196 µl culture was used and treated with 4 µL chondroitinase stock or the equivalent carrier control. Cultures were incubated for 30 min before imaging, based on the expected time required for chondroitinase activity (Woznica *et al.*, 2017). DIC images were collected on a Zeiss Axio Observer Widefield microscope equipped with a Plan-Apochromat 10× objective with a 1.6× Optovar setting. Images shown are representative fields from each condition. This experiment was performed once.

FM 1-43 staining and collar imaging
FM 1-43 dye was freshly prepared as a 200 µg/mL stock by resuspending 100 µg dye in 500 µL ddH_2O and was kept on ice and protected from light until use. For each sample, 5 µL of FM 1-43 stock was added to 195 µL of cell culture immediately before imaging. Labeled cells were transferred to poly-L-lysine-coated 96-well plates that had been washed twice with ASW. Cells were imaged immediately after dye addition to minimize effects of dye internalization over time.

FM 1-43-stained samples were imaged on a Zeiss LSM 880 Axio Observer microscope equipped with an Airyscan detector and a Plan-Apochromat 63×/1.4 Oil DIC M27 objective. Images were acquired in Fast Airyscan mode using a 458 nm laser and Airyscan detection. Z-stacks were collected with a 79.8 nm pixel size and a 162.3 nm Z-step. Images were acquired with 3× zoom, bidirectional scanning, line-sequential acquisition, two-frame averaging, a 1.86 µs pixel dwell time, and an Airyscan detector gain of 711. The image shown was acquired as a 552 × 552 pixel field of view with 46 Z-slices, corresponding to a 44.0 × 44.0 × 7.5 µm imaging volume. Airyscan processing was performed using 3D deconvolution with automatic parameter estimation.

Appendix 3 Figures and Tables

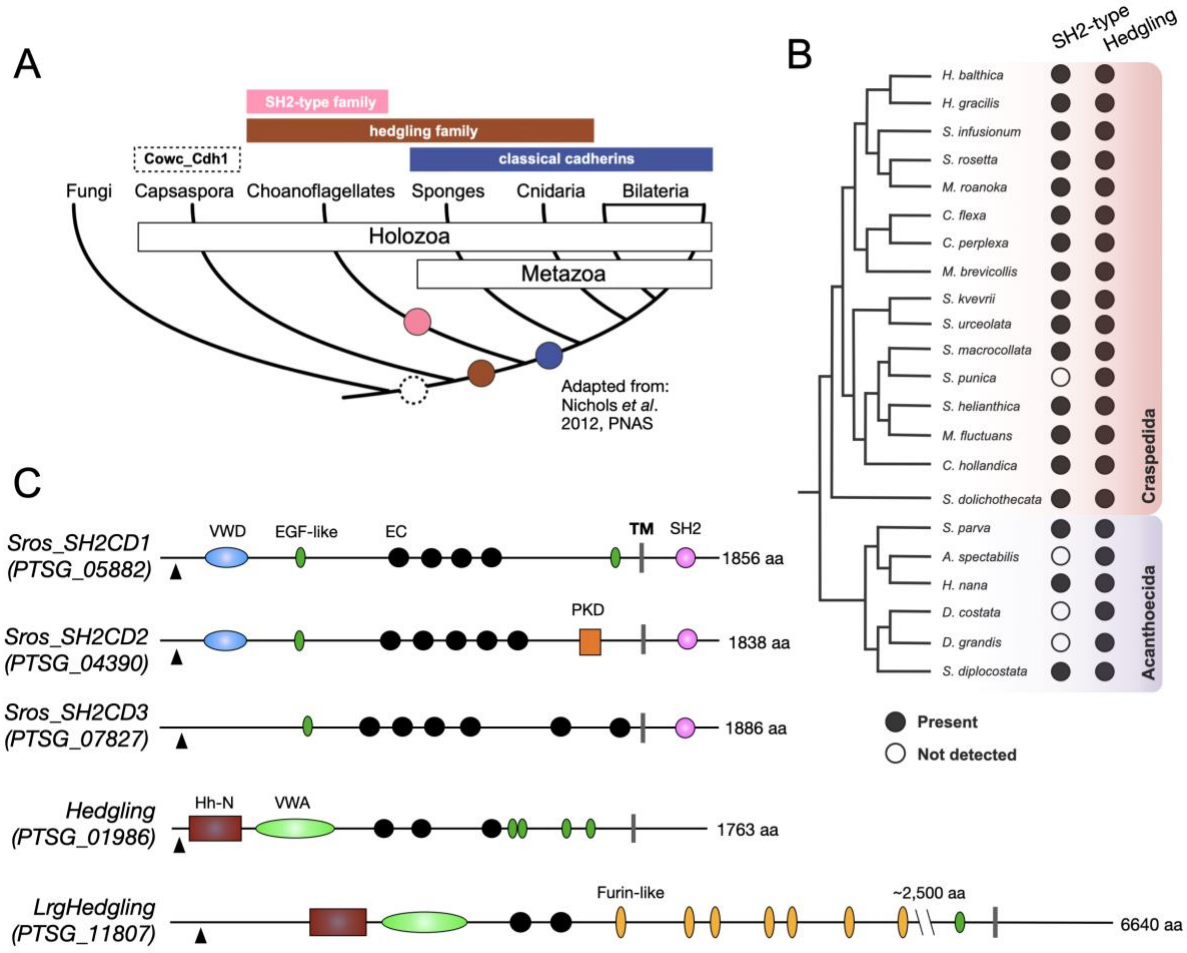

Figure A3.1: Two candidate cadherin gene families for functional characterization in *S. rosetta*. (A) Cadherins likely originated before choanozoan diversification, but most extant cadherin families are not shared between choanoflagellates and animals, with the exception of at least one family. A simplified phylogeny of opisthokonts is shown, with the cadherin gene families relevant to Appendix 3 indicated. SH2-type cadherins are found only in choanoflagellates (pink), whereas Hedgling cadherins are found in choanoflagellates and some early-branching animals (brown). Classical cadherins are conserved throughout animal diversity but not choanoflagellates (blue). *Capsaspora*, another close animal relative, has a single cadherin representative, suggesting that cadherins may predate the choanoflagellate-animal stem lineage (dotted circle). Figure adapted from Nichols *et al.* (2012). (B) SH2-type and Hedgling cadherins are broadly distributed across choanoflagellates. Filled circles indicate detected genes, and open circles indicate genes not detected. Searches were performed using InterProScan with the proteomes of each species (Richter *et al.*, 2018; Brunet *et al.*, 2019). The phylogenetic relationships shown are derived from Carr *et al.* (2017) with the addition of *C. flexa* from Brunet *et al.* (2019). (C) Three SH2-type and two Hedgling cadherins were targeted by CRISPR/Cas9

disruption. PTSG designations and names used in this appendix are listed for each gene. VWD, Von Willebrand factor type D domain; EGF-like, epidermal growth factor-like domain; EC, extracellular cadherin repeat; TM, transmembrane domain; SH2, Src homology 2 domain; PKD, polycystic kidney disease domain; Hh-N, Hedgehog amino-terminal signaling domain; VWA, von Willebrand factor type A domain. Black arrowheads indicate CRISPR-generated truncation sites (Booth and King, 2020).

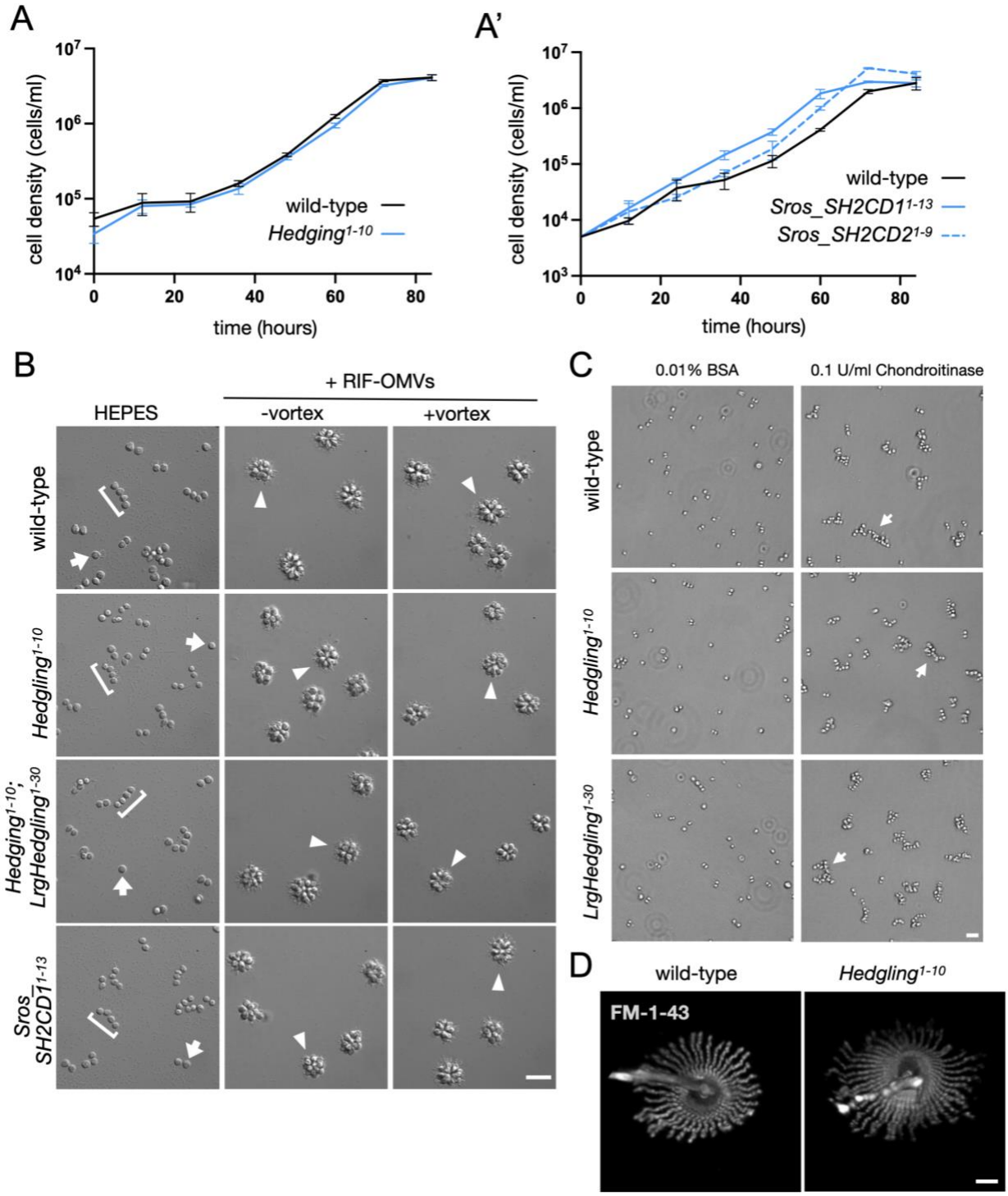
A
cell density (cells/ml)
time (hours)
wild-type
Hedging1-10
A'
cell density (cells/ml)
time (hours)
wild-type
Sros_SH2CD11-13
Sros_SH2CD21-9
B
HEPES
+ RIF-OMVs
-vortex
+vortex
wild-type
Hedgling1-10
Hedging1-10; LrgHedgling1-30
Sros_SH2CD11-13
C
0.01% BSA
0.1 U/ml Chondroitinase
wild-type
Hedgling1-10
LrgHedgling1-30
D
wild-type
Hedgling1-10
FM-1-43

Figure A3.2: Preliminary phenotypic findings in Hedgling and SH2-type cadherin mutants in *S. rosetta*. (A-A') Disruption of select cadherin genes does not obviously affect cell proliferation under the conditions tested. Growth curves comparing (A) wild-type and *Hedgling* mutant cultures and (A') wild-type, *Sros_SH2CD1* mutant, and *Sros_SH2CD2* mutant cultures are shown. Superscript notations indicate predicted amino acid sequences remaining for each mutant following CRISPR/Cas9-mediated gene editing. Cells were diluted to equal concentrations, triplicate samples were collected, and cell density was counted over time. Mean values are plotted, and error bars denote standard deviation. (B) Both single and double Hedgling mutants, along with the *Sros_SH2CD1* mutant, form single cells (arrows), chains (brackets), and, following RIF-OMV induction, shear-resistant rosettes (arrowheads) that resemble wild-type structures. Representative DIC images of wild-type and cadherin mutant cultures treated with carrier control (HEPES) or RIF-OMVs are shown. Scale bar, 20 μm. (C) Preliminary experiment indicates that Hedgling mutants retain clustering response to chondroitinase treatment. Representative DIC images of wild-type, *Hedgling* mutant, and *LrgHedgling* mutant cultures treated with carrier control or 0.1 U/mL chondroitinase are shown. Chondroitinase-treated cultures show increased cluster formation in wild-type and mutant backgrounds (white arrows). Scale bar, 20 μm. (D) *Hedgling* mutants appear to retain organized collar microvilli in preliminary observations. Representative images of wild-type and *Hedgling* mutant collars stained with the membrane marker FM-1-43 and imaged from the apical end of the cell are shown. Scale bar, 1 μm.

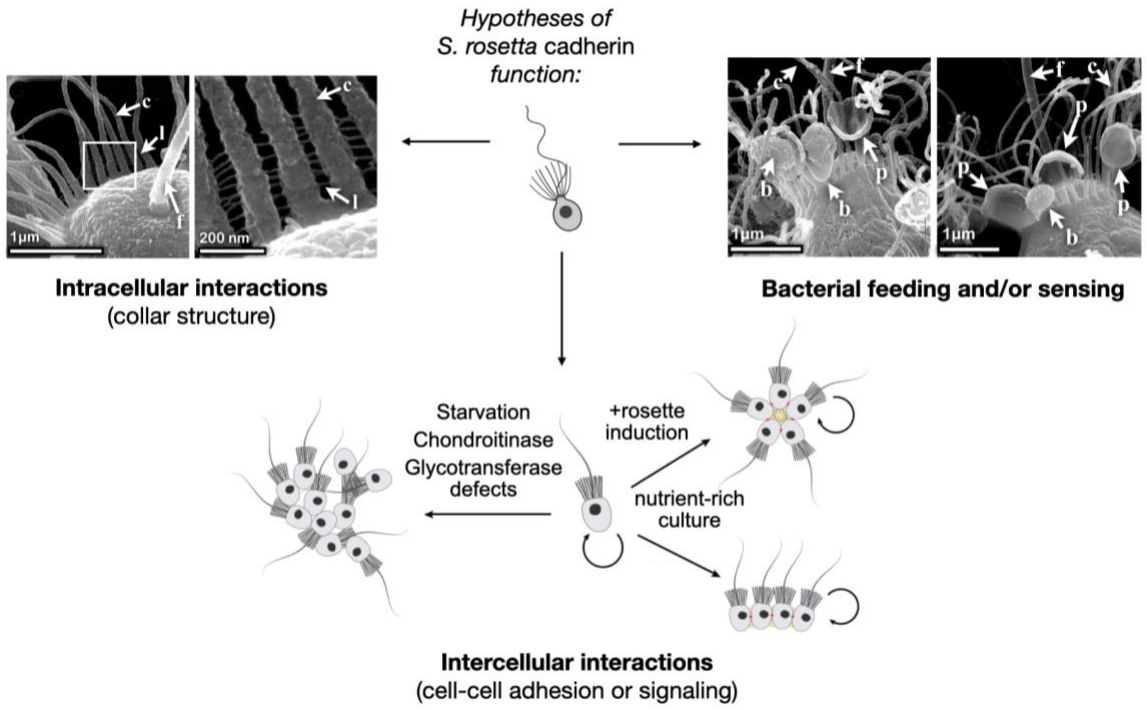

Figure A3.3: Future directions for research on cadherin function in *S. rosetta*. Candidate cellular functions for cadherins in *S. rosetta*. Future studies could test whether cadherins regulate collar organization, bacterial interactions, intercellular adhesion, or cell-ECM/substrate attachment during chain or rosette colony development. These assays may reveal specific cadherin functions not detected in the preliminary experiments shown in Figure A3.2. Images adapted from Dayel and King (2014). Labels: f, flagellum; c, collar microvilli; b, bacterium; p, phagocytic cup; v, food vacuole; t, theca; e, extracellular matrix; l, collar links.

Table A3. Nucleotide sequences for CRISPR/Cas9 gene editing of Hedgling and SH2-type cadherin genes.

Target (PTSG identifier / gene name)	crRNA sequence	Repair oligo sequence	Forward sequencing primer	Reverse sequencing primer
PTSG_01986 / *Hedgling*	GACAGCCAGGGCCACAACGA	GTCTGCGGAGTGCAGGACGGTGGTTGCGTTTGCGACAGCCAGGGCCACAATTTATTTAATTAAATAAACGAGGGCCAGGCAGACGCGCAGGTACGCCATG	GCGACCTTGCACCGAGC	TGGGCGCCAGAACCCAT
PTSG_11807 / *LrgHedgling*	ACACACGCTCGTCCACAAGA	GGTGTCTTTGTGGCACTCGTTGCAGTGCCTGCGACACACGCTCGTCCACATTTATTTAATTAAATAAAAGAAGGCATCATCAAGCCTCCAATGCCATCCGACACGTTTCTGGTATGTT	CGTTGCTGTGCCGAGTCCA	TTGGAAATCACGGTGGCGG
PTSG_05882 / *Sros_SH2CD1*	CAAGAAGAAGCCAGCCACAA	AAGACAACAAACGATGCGCGCACCAGGAGGCGTGTGCGCCGCCACCGTTGTTTATTTAATTAAATAAATGGCTGGCTTCTTCTTGCTGTTGACATGCGTCAGCGCTGGTGGGTACTGG	CGCGCCTGGGAAAACAACAC	TGCACACGTCACATCACGC
PTSG_04390 / *Sros_SH2CD2*	CCACCAGCAGCATGACACAG	TGTCCACGTGGATGCGCTGGGCAGCGGCAGAGGCCACCAGCAGCATGACATTTATTTAATTAAATAAACAGAGGCCAAGCATGCGCAGAGCAGCCATGGTTGGCAGTGTGTTGGAGCA	AACCAACGCCTGCTTCTCGTG	TGGGTGGTGCAAATGATGGGC
PTSG_07827 / *Sros_SH2CD3*	AGCGCGTCGCTGTACTACAA	AAGGATTTCACCATTGTGACGGAGCCCATTGACAGCGCGTCGCTGTACTATTTATTTAATTAAATAAACAACGGCTTTGACCTGCCGGACCTGAGCCTGGAGACGGCCCCGCGGCCCT	GCACACCAACCACACAACAGACC	AAACCTGCGCACGGTGGA

Bibliography

Abedin, M (2010). Cadherin evolution and the origin of animals [Doctoral dissertation, University of California, Berkeley]. eScholarship. https://escholarship.org/uc/item/59s8x1cb.

Abedin, M, and King, N (2008). The Premetazoan Ancestry of Cadherins. Science 319, 946–948.

Abedin, M, and King, N (2010). Diverse evolutionary paths to cell adhesion. Trends Cell Biol 20, 734–742.

Abramson, J, Adler, J, Dunger, J, Evans, R, Green, T, Pritzel, A, Ronneberger, O, Willmore, L, Ballard, AJ, Bambrick, J, *et al.* (2024). Accurate structure prediction of biomolecular interactions with AlphaFold 3. Nature 630, 493–500.

Adamska, M, Matus, DQ, Adamski, M, Green, K, Rokhsar, DS, Martindale, MQ, and Degnan, BM (2007). The evolutionary origin of hedgehog proteins. Curr Biol 17, R836–R837.

Alegado, RA, Brown, LW, Cao, S, Dermenjian, RK, Zuzow, R, Fairclough, SR, Clardy, J, and King, N (2012). A bacterial sulfonolipid triggers multicellular development in the closest living relatives of animals. Elife 1, e00013.

Alegado, RA, Grabenstatter, JD, Zuzow, R, Morris, A, Huang, SY, Summons, RE, and King, N (2013). Algoriphagus machipongonensis sp. nov., co-isolated with a colonial choanoflagellate. Int J Syst Evol Microbiol 63, 163–168.

Amini, R, Goupil, E, Labella, S, Zetka, M, Maddox, AS, Labbé, J-C, and Chartier, NT (2014). C. elegans Anillin proteins regulate intercellular bridge stability and germline syncytial organization. J Cell Biol 206, 129–143.

Anderson, DP, Whitney, DS, Hanson-Smith, V, Woznica, A, Campodonico-Burnett, W, Volkman, BF, King, N, Thornton, JW, and Prehoda, KE (2016). Evolution of an ancient protein function involved in organized multicellularity in animals. eLife 5, e10147.

Arakaki, Y, Fujiwara, T, Kawai-Toyooka, H, Kawafune, K, Featherston, J, Durand, PM, Miyagishima, S, and Nozaki, H (2017). Evolution of cytokinesis-related protein localization during the emergence of multicellularity in volvocine green algae. BMC Evol Biol 17, 243.

Balasubramanian, MK, Bi, E, and Glotzer, M (2004). Comparative analysis of cytokinesis in budding yeast, fission yeast and animal cells. Curr Biol 14, R806-818.

Baluška, F, Volkmann, D, Menzel, D, and Barlow, P (2012). Strasburger's legacy to mitosis and cytokinesis and its relevance for the Cell Theory. Protoplasma 249, 1151–1162.

Barone, V, Tagua, A, Román, JÁA-S, Hamdoun, A, Garrido-García, J, Lyons, DC, and Escudero, LM (2024). Local and global changes in cell density induce reorganisation of 3D packing in a proliferating epithelium. Development 151, dev202362.

Bauer, R, Begerow, D, Sampaio, JP, Weiβ, M, and Oberwinkler, F (2006). The simple-septate basidiomycetes: a synopsis. Mycol Progress 5, 41–66.

Berepiki, A, Lichius, A, Shoji, J-Y, Tilsner, J, and Read, ND (2010). F-actin dynamics in Neurospora crassa. Eukaryot Cell 9, 547–557.

Bertin, A, McMurray, MA, Grob, P, Park, S-S, Garcia, G, Patanwala, I, Ng, H, Alber, T, Thorner, J, and Nogales, E (2008). Saccharomyces cerevisiae septins: Supramolecular organization of heterooligomers and the mechanism of filament assembly. Proceedings of the National Academy of Sciences 105, 8274–8279.

Betschinger, J, and Knoblich, JA (2004). Dare to Be Different: Asymmetric Cell Division in Drosophila, C. elegans and Vertebrates. Current Biology 14, R674–R685.

Bolkent, S (2024). Cellular and molecular mechanisms of asymmetric stem cell division in tissue homeostasis. Genes Cells 29, 1099–1110.

Booth, DS, and King, N (2020). Genome editing enables reverse genetics of multicellular development in the choanoflagellate Salpingoeca rosetta. Elife 9, e56193.

Booth, DS, and King, N (2022). The history of Salpingoeca rosetta as a model for reconstructing animal origins. Curr Top Dev Biol 147, 73–91.

Booth, DS, Szmidt-Middleton, H, and King, N (2018). Transfection of choanoflagellates illuminates their cell biology and the ancestry of animal septins. Mol Biol Cell 29, 3026–3038.

Boraas, ME, Seale, DB, and Boxhorn, JE (1998). Phagotrophy by a flagellate selects for colonial prey: A possible origin of multicellularity. Evolutionary Ecology 12, 153–164.

Bowen, JR, Hwang, D, Bai, X, Roy, D, and Spiliotis, ET (2011). Septin GTPases spatially guide microtubule organization and plus end dynamics in polarizing epithelia. J Cell Biol 194, 187–197.

Bozdag, GO, Zamani-Dahaj, SA, Day, TC, Kahn, PC, Burnetti, AJ, Lac, DT, Tong, K, Conlin, PL, Balwani, AH, Dyer, EL, *et al.* (2023). De novo evolution of macroscopic multicellularity. Nature 617, 747–754.

Brasch, J, Harrison, OJ, Honig, B, and Shapiro, L (2012). Thinking outside the cell: how cadherins drive adhesion. Trends Cell Biol 22, 299–310.

Bray, NL, Pimentel, H, Melsted, P, and Pachter, L (2016). Near-optimal probabilistic RNA-seq quantification. Nat Biotechnol 34, 525–527.

Bridges, AA, and Gladfelter, AS (2015). Septin Form and Function at the Cell Cortex*. J Biol Chem 290, 17173–17180.

Brunet, T, Albert, M, Roman, W, Coyle, MC, Spitzer, DC, and King, N (2021). A flagellate-to-amoeboid switch in the closest living relatives of animals. eLife 10, e61037.

Brunet, T, and King, N (2017). The Origin of Animal Multicellularity and Cell Differentiation. Dev Cell 43, 124–140.

Brunet, T, Larson, BT, Linden, TA, Vermeij, MJA, McDonald, K, and King, N (2019). Light-regulated collective contractility in a multicellular choanoflagellate. Science 366, 326–334.

Buckley, CE, and Johnston, DS (2022). Apical–basal polarity and the control of epithelial form and function. Nat Rev Mol Cell Biol 23, 559–577.

Burki, F, Roger, AJ, Brown, MW, and Simpson, AGB (2020). The New Tree of Eukaryotes. Trends Ecol Evol 35, 43–55.

Buss, LW (1987). The Evolution of Individuality, Princeton, NJ: Princeton University Press.

Cadart, C, Zlotek-Zlotkiewicz, E, Le Berre, M, Piel, M, and Matthews, HK (2014). Exploring the function of cell shape and size during mitosis. Dev Cell 29, 159–169.

del Campo, J, and Ruiz-Trillo, I (2013). Environmental Survey Meta-analysis Reveals Hidden Diversity among Unicellular Opisthokonts. Mol Biol Evol 30, 802–805.

Carim, SC, Kechad, A, and Hickson, GRX (2020). Animal Cell Cytokinesis: The Rho-Dependent Actomyosin-Anilloseptin Contractile Ring as a Membrane Microdomain Gathering, Compressing, and Sorting Machine. Front Cell Dev Biol 8, 575226.

Carlton, JG, Caballe, A, Agromayor, M, Kloc, M, and Martin-Serrano, J (2012). ESCRT-III governs the Aurora B-mediated abscission checkpoint through CHMP4C. Science 336, 220–225.

Carr, M, Leadbeater, BSC, Hassan, R, Nelson, M, and Baldauf, SL (2008). Molecular phylogeny of choanoflagellates, the sister group to Metazoa. Proc National Acad Sci 105, 16641–16646.

Chaigne, A, and Brunet, T (2022). Incomplete abscission and cytoplasmic bridges in the evolution of eukaryotic multicellularity. Curr Biol 32, R385–R397.

Chandra, S, and Rutaganira, FU (2025). Glycerol improves the viability of a cryopreserved choanoflagellate. Cryobiology 118, 105183.

Chen, X, Zaro, JL, and Shen, W-C (2013). Fusion protein linkers: Property, design and functionality. Advanced Drug Delivery Reviews 65, 1357–1369.

Combredet, C, Ansel, M, and Brunet, T (2025). A selection-based knockout approach for a choanoflagellate reveals regulation of multicellular development by Hippo signaling. Cell Rep 44, 116345.

Coyle, MC, Tajima, AM, Leon, F, Choksi, SP, Yang, A, Espinoza, S, Hughes, TR, Reiter, JF, Booth, DS, and King, N (2023). An RFX transcription factor regulates ciliogenesis in the closest living relatives of animals. Curr Biol 33, 3747-3758.e9.

Crawley, SW, Shifrin, DA, Grega-Larson, NE, McConnell, RE, Benesh, AE, Mao, S, Zheng, Y, Zheng, QY, Nam, KT, Millis, BA, *et al.* (2014). Intestinal Brush Border Assembly Driven by Protocadherin-Based Intermicrovillar Adhesion. Cell 157, 433–446.

Dayel, MJ, Alegado, RA, Fairclough, SR, Levin, TC, Nichols, SA, McDonald, K, and King, N (2011). Cell differentiation and morphogenesis in the colony-forming choanoflagellate Salpingoeca rosetta. Dev Biol 357, 73–82.

Dayel, MJ, and King, N (2014). Prey Capture and Phagocytosis in the Choanoflagellate Salpingoeca rosetta. Plos One 9, e95577.

Delic, S, Shuman, B, Lee, S, Bahmanyar, S, Momany, M, and Onishi, M (2024). The evolutionary origins and ancestral features of septins. Front Cell Dev Biol 12, 1406966. https://doi.org/10.3389/fcell.2024.1406966

Delic, S, Vetrano, P, Simon, CS, Su, D, Xiang, Y, Wu, S-Z, Heyde, EL von der, Tajima-Shirasaki, N, Chen, S-A, Brillada, C, *et al.* (2026). Septin-mediated coupling of protein import and division during chloroplast evolution. bioRxiv, 2026.03.28.715002.

Delmer, D, Dixon, RA, Keegstra, K, and Mohnen, D (2024). The plant cell wall-dynamic, strong, and adaptable-is a natural shapeshifter. Plant Cell 36, 1257–1311.

Díaz-de-la-Loza, M-D-C, and Stramer, BM (2024). The extracellular matrix in tissue morphogenesis: No longer a backseat driver. Cells Dev 177, 203883.

Dix, CL, Matthews, HK, Uroz, M, McLaren, S, Wolf, L, Heatley, N, Win, Z, Almada, P, Henriques, R, Boutros, M, *et al.* (2018). The Role of Mitotic Cell-Substrate Adhesion Remodeling in Animal Cell Division. Dev Cell 45, 132-145.e3.

Domozych, DS, and Domozych, CE (2014). Multicellularity in green algae: upsizing in a walled complex. Front Plant Sci 5, 649.

Du, Q, Kawabe, Y, Schilde, C, Chen, Z, and Schaap, P (2015). The Evolution of Aggregative Multicellularity and Cell–Cell Communication in the Dictyostelia. Journal of Molecular Biology 427, 3722–3733.

Dunbrack, RL (2025). Rēs ipSAE loquunt: What's wrong with AlphaFold's ipTM score and how to fix it. bioRxiv, 2025.02.10.637595.

Eisenhoffer, GT, Loftus, PD, Yoshigi, M, Otsuna, H, Chien, C-B, Morcos, PA, and Rosenblatt, J (2012). Crowding induces live cell extrusion to maintain homeostatic cell numbers in epithelia. Nature 484, 546–549.

Estey, MP, Ciano-Oliveira, CD, Froese, CD, Bejide, MT, and Trimble, WS (2010). Distinct roles of septins in cytokinesis: SEPT9 mediates midbody abscission. J Cell Biol 191, 741–749.

Evans, T, Rosenthal, ET, Youngblom, J, Distel, D, and Hunt, T (1983). Cyclin: a protein specified by maternal mRNA in sea urchin eggs that is destroyed at each cleavage division. Cell 33, 389–396.

Fairclough, SR, Chen, Z, Kramer, E, Zeng, Q, Young, S, Robertson, HM, Begovic, E, Richter, DJ, Russ, C, Westbrook, MJ, *et al.* (2013). Premetazoan genome evolution and the regulation of cell differentiation in the choanoflagellate Salpingoeca rosetta. Genome Biol 14, R15.

Fairclough, SR, Dayel, MJ, and King, N (2010). Multicellular development in a choanoflagellate. Curr Biol 20, R875–R876.

Fares, H, Peifer, M, and Pringle, JR (1995). Localization and possible functions of Drosophila septins. Mol Biol Cell 6, 1843–1859.

Farhadifar, R, Röper, J-C, Aigouy, B, Eaton, S, and Jülicher, F (2007). The influence of cell mechanics, cell-cell interactions, and proliferation on epithelial packing. Curr Biol 17, 2095–2104.

Founounou, N, Loyer, N, and Le Borgne, R (2013). Septins Regulate the Contractility of the Actomyosin Ring to Enable Adherens Junction Remodeling during Cytokinesis of Epithelial Cells. Dev Cell 24, 242–255.

Gabbert, AM, Campanale, JP, Mondo, JA, Mitchell, NP, Myers, A, Streichan, SJ, Miolane, N, and Montell, DJ (2023). Septins regulate border cell surface geometry, shape, and motility downstream of Rho in Drosophila. Dev Cell 58, 1399-1413.e5.

Gibson, MC, Patel, AB, Nagpal, R, and Perrimon, N (2006). The emergence of geometric order in proliferating metazoan epithelia. Nature 442, 1038–1041.

Gibson, WT, Veldhuis, JH, Rubinstein, B, Cartwright, HN, Perrimon, N, Brodland, GW, Nagpal, R, and Gibson, MC (2011). Control of the Mitotic Cleavage Plane by Local Epithelial Topology. Cell 144, 427–438.

Gilbert, OM, Foster, KR, Mehdiabadi, NJ, Strassmann, JE, and Queller, DC (2007). High relatedness maintains multicellular cooperation in a social amoeba by controlling cheater mutants. Proceedings of the National Academy of Sciences 104, 8913–8917.

Gilden, JK, Peck, S, Chen, Y-CM, and Krummel, MF (2012). The septin cytoskeleton facilitates membrane retraction during motility and blebbing. J Cell Biol 196, 103–114.

Gillies, TE, and Cabernard, C (2011). Cell division orientation in animals. Curr Biol 21, R599-609.

Gómez-Gálvez, P, Vicente-Munuera, P, Tagua, A, Forja, C, Castro, AM, Letrán, M, Valencia-Expósito, A, Grima, C, Bermúdez-Gallardo, M, Serrano-Pérez-Higueras, Ó, *et al.* (2018). Scutoids are a geometrical solution to three-dimensional packing of epithelia. Nat Commun 9, 2960.

Götzke, H, Kilisch, M, Martínez-Carranza, M, Sograte-Idrissi, S, Rajavel, A, Schlichthaerle, T, Engels, N, Jungmann, R, Stenmark, P, Opazo, F, *et al.* (2019). The ALFA-tag is a highly versatile tool for nanobody-based bioscience applications. Nat Commun 10, 4403.

Gow, NAR (2025). Fungal cell wall biogenesis: structural complexity, regulation and inhibition. Fungal Genetics and Biology 179, 103991.

Green, RA, Paluch, E, and Oegema, K (2012). Cytokinesis in Animal Cells. Annu Rev Cell Dev Biol 28, 29–58.

Greenbaum, MP, Iwamori, T, Buchold, GM, and Matzuk, MM (2011). Germ Cell Intercellular Bridges. Csh Perspect Biol 3, a005850.

Grill, SW, Gönczy, P, Stelzer, EH, and Hyman, AA (2001). Polarity controls forces governing asymmetric spindle positioning in the Caenorhabditis elegans embryo. Nature 409, 630–633.

Guertin, DA, Trautmann, S, and McCollum, D (2002). Cytokinesis in Eukaryotes. Microbiol Mol Biol Rev 66, 155–178.

Guillot, C, and Lecuit, T (2013). Adhesion disengagement uncouples intrinsic and extrinsic forces to drive cytokinesis in epithelial tissues. Dev Cell 24, 227–241.

Haglund, K, Nezis, IP, and Stenmark, H (2011). Structure and functions of stable intercellular bridges formed by incomplete cytokinesis during development. Commun Integr Biol 4, 1–9.

Hake, KH, West, PT, McDonald, K, Laundon, D, Reyes-Rivera, J, Bayonas, AGDL, Feng, C, Burkhardt, P, Richter, DJ, Banfield, JF, *et al.* (2024). A large colonial choanoflagellate from Mono Lake harbors live bacteria. mBio 15, e01623-24.

Halbleib, JM, and Nelson, WJ (2006). Cadherins in development: cell adhesion, sorting, and tissue morphogenesis. Gene Dev 20, 3199–3214.

Hallegraeff, G, Anderson, D, and Cembella, A (2004). Manual on Harmful Marine Microalgae, Paris, France: United Nations Educational, Scientific and Cultural Organization.

Hanschen, ER, Marriage, TN, Ferris, PJ, Hamaji, T, Toyoda, A, Fujiyama, A, Neme, R, Noguchi, H, Minakuchi, Y, Suzuki, M, *et al.* (2016). The Gonium pectorale genome demonstrates co-option of cell cycle regulation during the evolution of multicellularity. Nat Commun 7, 11370.

Harashima, H, Dissmeyer, N, and Schnittger, A (2013). Cell cycle control across the eukaryotic kingdom. Trends Cell Biol 23, 345–356.

Hartwell, LH, Culotti, J, Pringle, JR, and Reid, BJ (1974). Genetic Control of the Cell Division Cycle in Yeast. Science 183, 46–51.

Hartwell, LH, Mortimer, RK, Culotti, J, and Culotti, M (1973). GENETIC CONTROL OF THE CELL DIVISION CYCLE IN YEAST: V. GENETIC ANALYSIS OF cdc MUTANTS. Genetics 74, 267–286.

Herron, MD (2016). Origins of multicellular complexity: Volvox and the volvocine algae. Mol Ecol 25, 1213–1223.

Herron, MD, Borin, JM, Boswell, JC, Walker, J, Chen, I-CK, Knox, CA, Boyd, M, Rosenzweig, F, and Ratcliff, WC (2019). De novo origins of multicellularity in response to predation. Sci Rep 9, 2328.

Herszterg, S, Pinheiro, D, and Bellaïche, Y (2014). A multicellular view of cytokinesis in epithelial tissue. Trends in Cell Biology 24, 285–293.

Hibberd, DJ (1975). Observations on the ultrastructure of the choanoflagellate Codosiga botrytis (Ehr.) saville-kent with special reference to the flagellar apparatus. J Cell Sci 17, 191–219.

Higashi, T, Arnold, TR, Stephenson, RE, Dinshaw, KM, and Miller, AL (2016). Maintenance of the Epithelial Barrier and Remodeling of Cell-Cell Junctions during Cytokinesis. Curr Biol 26, 1829–1842.

Hooke, R (1665). Micrographia: or some physiological descriptions of minute bodies made by magnifying glasses, with observations and inquiries thereupon, London, UK: Jo. Martyn and Ja. Allestry.

Hoops, HJ, Nishii, I, and Kirk, DL (2006). Cytoplasmic Bridges in Volvox and Its Relatives. In: Cell-Cell Channels, New York, NY: Springer, 65–84.

Hu, C-K, Coughlin, M, and Mitchison, TJ (2012a). Midbody assembly and its regulation during cytokinesis. Mol Biol Cell 23, 1024–1034.

Hu, J, Bai, X, Bowen, JR, Dolat, L, Korobova, F, Yu, W, Baas, PW, Svitkina, T, Gallo, G, and Spiliotis, ET (2012b). Septin-Driven Coordination of Actin and Microtubule Remodeling Regulates the Collateral Branching of Axons. Curr Biol 22, 1109–1115.

Hümpfer, N, Marin, Z, Zehtabian, A, Bruckmann, K, Spierling, D, Schmoranzer, J, Ries, J, and Ewers, H (2025). Multiscale imaging of cytokinesis. bioRxiv, 2025.09.24.678330.

Ivorra-Molla, E, Akhuli, D, McAndrew, MBL, Scott, W, Kumar, L, Palani, S, Mishima, M, Crow, A, and Balasubramanian, MK (2024). A monomeric StayGold fluorescent protein. Nat Biotechnol 42, 1368–1371.

Iwamori, T, Iwamori, N, Ma, L, Edson, MA, Greenbaum, MP, and Matzuk, MM (2010). TEX14 interacts with CEP55 to block cell abscission. Mol Cell Biol 30, 2280–2292.

Jones, P, Binns, D, Chang, H-Y, Fraser, M, Li, W, McAnulla, C, McWilliam, H, Maslen, J, Mitchell, A, Nuka, G, *et al.* (2014). InterProScan 5: genome-scale protein function classification. Bioinformatics 30, 1236–1240.

Joo, E, Surka, MC, and Trimble, WS (2007). Mammalian SEPT2 Is Required for Scaffolding Nonmuscle Myosin II and Its Kinases. Dev Cell 13, 677–690.

Jürgens, G (2005). Plant cytokinesis: fission by fusion. Trends Cell Biol 15, 277–283.

Kamranvar, SA, Gupta, DK, Huang, Y, Gupta, RK, and Johansson, S (2016). Integrin signaling via FAK-Src controls cytokinetic abscission by decelerating PLK1 degradation and subsequent recruitment of CEP55 at the midbody. Oncotarget 7, 30820–30830.

Karasmanis, EP, Hwang, D, Nakos, K, Bowen, JR, Angelis, D, and Spiliotis, ET (2019). A Septin Double Ring Controls the Spatiotemporal Organization of the ESCRT Machinery in Cytokinetic Abscission. Curr Biol 29, 2174-2182.e7.

Karpov, SA, and Coupe, SJ (1998). A Revision of Choanoflagellate Genera Kentrosiga Schiller, 1953 and Desmarella Kent, 1880. Acta Protozoologica 37, 23–27.

Karpov, SA, and Leadbeater, BSC (1997). Cell and nuclear division in a freshwater choanoflagellate, Monosiga ovata Kent. Eur J Protistol 33, 323–334.

Karpov, SA, and Leadbeater, BSC (1998). Cytoskeleton Structure and Composition in Choanoflagellates. J Eukaryot Microbiol 45, 361–367.

Kechad, A, Jananji, S, Ruella, Y, and Hickson, GRX (2012). Anillin Acts as a Bifunctional Linker Coordinating Midbody Ring Biogenesis during Cytokinesis. Current Biology 22, 197–203.

Kim, MS, Froese, CD, Estey, MP, and Trimble, WS (2011). SEPT9 occupies the terminal positions in septin octamers and mediates polymerization-dependent functions in abscission. J Cell Biol 195, 815–826.

King, N, Hittinger, CT, and Carroll, SB (2003). Evolution of Key Cell Signaling and Adhesion Protein Families Predates Animal Origins. Science 301, 361–363.

King, N, Westbrook, MJ, Young, SL, Kuo, A, Abedin, M, Chapman, J, Fairclough, S, Hellsten, U, Isogai, Y, Letunic, I, *et al.* (2008). The genome of the choanoflagellate Monosiga brevicollis and the origin of metazoans. Nature 451, 783–788.

Kinoshita, M (2003). The septins. Genome Biol 4, 236.

Kinoshita, M, Field, CM, Coughlin, ML, Straight, AF, and Mitchison, TJ (2002). Self- and actin-templated assembly of Mammalian septins. Dev Cell 3, 791–802.

Kirk, DL, Birchem, R, and King, N (1986). The extracellular matrix of Volvox: a comparative study and proposed system of nomenclature. J Cell Sci 80, 207–231.

Kloareg, B, Badis, Y, Cock, JM, and Michel, G (2021). Role and Evolution of the Extracellular Matrix in the Acquisition of Complex Multicellularity in Eukaryotes: A Macroalgal Perspective. Genes (Basel) 12, 1059.

Knoblich, JA (2008). Mechanisms of Asymmetric Stem Cell Division. Cell 132, 583–597.

Knoll, AH (2011). The Multiple Origins of Complex Multicellularity. Annual Review of Earth and Planetary Sciences 39, 217–239.

Kulukian, A, and Fuchs, E (2013). Spindle orientation and epidermal morphogenesis. Philos Trans R Soc Lond B Biol Sci 368, 20130016.

Lafaurie-Janvore, J, Maiuri, P, Wang, I, Pinot, M, Manneville, J-B, Betz, T, Balland, M, and Piel, M (2013). ESCRT-III assembly and cytokinetic abscission are induced by tension release in the intercellular bridge. Science 339, 1625–1629.

Lancaster, OM, Le Berre, M, Dimitracopoulos, A, Bonazzi, D, Zlotek-Zlotkiewicz, E, Picone, R, Duke, T, Piel, M, and Baum, B (2013). Mitotic rounding alters cell geometry to ensure efficient bipolar spindle formation. Dev Cell 25, 270–283.

Landino, J, Misterovich, E, van den Goor, L, Adhikary, B, Chumki, S, Davidson, LA, and Miller, AL (2025). Neighbor cells restrain furrowing during Xenopus epithelial cytokinesis. Developmental Cell 60, 2139-2148.e6.

Larson, BT, Ruiz-Herrero, T, Lee, S, Kumar, S, Mahadevan, L, and King, N (2020). Biophysical principles of choanoflagellate self-organization. Proc National Acad Sci 117, 1303–1311.

Leadbeater, BSC (1994). Developmental studies on the loricate choanoflagellate *Stephanoeca diplocostata* ellis. European Journal of Protistology 30, 171–183.

Leadbeater, BSC (2015). The choanoflagellates: evolution, biology, and ecology, Cambridge (GB): Cambridge university press.

Lechler, T, and Fuchs, E (2005). Asymmetric cell divisions promote stratification and differentiation of mammalian skin. Nature 437, 275–280.

Lechler, T, and Mapelli, M (2021). Spindle positioning and its impact on vertebrate tissue architecture and cell fate. Nat Rev Mol Cell Biol 22, 691–708.

Leon, F, Espinoza-Esparza, JM, Deng, V, Coyle, MC, Espinoza, S, and Booth, DS (2025). Cell differentiation controls iron assimilation in the choanoflagellate Salpingoeca rosetta. mSphere 10, e00917-24.

Letunic, I, and Bork, P (2021). Interactive Tree Of Life (iTOL) v5: an online tool for phylogenetic tree display and annotation. Nucleic Acids Res 49, W293–W296.

Levin, TC, Greaney, AJ, Wetzel, L, and King, N (2014). The rosetteless gene controls development in the choanoflagellate S. rosetta. Elife 3, e04070.

Levin, TC, and King, N (2013). Evidence for Sex and Recombination in the Choanoflagellate Salpingoeca rosetta. Curr Biol 23, 2176–2180.

Liang, F, Sun, M, Xie, L, Zhao, X, Liu, D, Zhao, K, and Zhang, G (2024). Recent advances and challenges in protein complex model accuracy estimation. Computational and Structural Biotechnology Journal 23, 1824–1832.

Lo, WS, and Dranginis, AM (1996). FLO11, a yeast gene related to the STA genes, encodes a novel cell surface flocculin. J Bacteriol 178, 7144–7151.

López-Escardó, D, Grau-Bové, X, Guillaumet-Adkins, A, Gut, M, Sieracki, ME, and Ruiz-Trillo, I (2019). Reconstruction of protein domain evolution using single-cell amplified genomes of uncultured choanoflagellates sheds light on the origin of animals. Philos Trans R Soc Lond B Biol Sci 374, 20190088.

Matus, DQ, Magie, CR, Pang, K, Martindale, MQ, and Thomsen, GH (2008). The Hedgehog gene family of the cnidarian, Nematostella vectensis, and implications for understanding metazoan Hedgehog pathway evolution. Dev Biol 313, 501–518.

McMurray, MA, Bertin, A, Garcia, G, Lam, L, Nogales, E, and Thorner, J (2011). Septin Filament Formation is Essential in Budding Yeast. Dev Cell 20, 540–549.

Mendonça, DC, Guimarães, SL, Pereira, HD, Pinto, AA, Farias, MA de, Godoy, AS de, Araujo, APU, Heel, M van, Portugal, RV, and Garratt, RC (2021). An atomic model for the human septin hexamer by cryo-EM. J Mol Biol 433, 167096.

Meng, EC, Goddard, TD, Pettersen, EF, Couch, GS, Pearson, ZJ, Morris, JH, and Ferrin, TE (2023). UCSF ChimeraX: Tools for structure building and analysis. Protein Science 32, e4792.

Mengaud, J, Ohayon, H, Gounon, P, Mège, R-M, and Cossart, P (1996). E-Cadherin Is the Receptor for Internalin, a Surface Protein Required for Entry of L. monocytogenes into Epithelial Cells. Cell 84, 923–932.

Menon, MB, Sawada, A, Chaturvedi, A, Mishra, P, Schuster-Gossler, K, Galla, M, Schambach, A, Gossler, A, Förster, R, Heuser, M, *et al.* (2014). Genetic Deletion of SEPT7 Reveals a Cell Type-Specific Role of Septins in Microtubule Destabilization for the Completion of Cytokinesis. PLOS Genetics 10, e1004558.

Mierzwa, B, and Gerlich, DW (2014). Cytokinetic Abscission: Molecular Mechanisms and Temporal Control. Dev Cell 31, 525–538.

Miller, SM, and Kirk, DL (1999). glsA, a Volvox gene required for asymmetric division and germ cell specification, encodes a chaperone-like protein. Development 126, 649–658.

Momany, M, Zhao, J, Lindsey, R, and Westfall, PJ (2001). Characterization of the Aspergillus nidulans septin (asp) gene family. Genetics 157, 969–977.

Mostowy, S, and Cossart, P (2012). Septins: the fourth component of the cytoskeleton. Nat Rev Mol Cell Biol 13, 183–194.

Murray, AW, and Kirschner, MW (1989). Cyclin synthesis drives the early embryonic cell cycle. Nature 339, 275–280.

Nagy, LG, Varga, T, Csernetics, Á, and Virágh, M (2020). Fungi took a unique evolutionary route to multicellularity: Seven key challenges for fungal multicellular life. Fungal Biology Reviews 34, 151–169.

Nakajima, Y, Meyer, EJ, Kroesen, A, McKinney, SA, and Gibson, MC (2013). Epithelial junctions maintain tissue architecture by directing planar spindle orientation. Nature 500, 359–362.

Neufeld, TP, and Rubin, GM (1994). The Drosophila peanut gene is required for cytokinesis and encodes a protein similar to yeast putative bud neck filament proteins. Cell 77, 371–379.

Nguyen, MHT, Hernandez, IS, and Rutaganira, FU (2026). An accessible transfection protocol for choanoflagellates. bioRxiv, 2026.03.10.710884. https://doi.org/10.64898/2026.03.10.710884

Nguyen, TQ, Sawa, H, Okano, H, and White, JG (2000). The C. elegans septin genes, unc-59 and unc-61, are required for normal postembryonic cytokineses and morphogenesis but have no essential function in embryogenesis. J Cell Sci 113, 3825–3837.

Nichols, SA, Roberts, BW, Richter, DJ, Fairclough, SR, and King, N (2012). Origin of metazoan cadherin diversity and the antiquity of the classical cadherin/β-catenin complex. Proc National Acad Sci 109, 13046–13051.

Nicolas, WJ, Grison, MS, Trépout, S, Gaston, A, Fouché, M, Cordelières, FP, Oparka, K, Tilsner, J, Brocard, L, and Bayer, EM (2017). Architecture and permeability of post-cytokinesis plasmodesmata lacking cytoplasmic sleeves. Nat Plants 3, 17082.

Nishii, I, and Miller, SM (2010). Volvox: Simple steps to developmental complexity? Curr Opin Plant Biol 13, 646–653.

Nurse, P (1990). Universal control mechanism regulating onset of M-phase. Nature 344, 503–508.

Ong, S, Foote, C, and Tan, C (2010). Mutations of DMYPT cause over constriction of contractile rings and ring canals during *Drosophila* germline cyst formation. Developmental Biology 346, 161–169.

Onishi, M, Umen, JG, Cross, FR, and Pringle, JR (2020). Cleavage-furrow formation without F-actin in Chlamydomonas. Proc Natl Acad Sci U S A 117, 18511–18520.

Osswald, M, and Morais-de-Sá, E (2019). Dealing with apical-basal polarity and intercellular junctions: a multidimensional challenge for epithelial cell division. Curr Opin Cell Biol 60, 75–83.

Ozugergin, I, and Piekny, A (2022). Diversity is the spice of life: An overview of how cytokinesis regulation varies with cell type. Front Cell Dev Biol 10, 1007614.

Palander, O, El-Zeiry, M, and Trimble, WS (2017). Uncovering the Roles of Septins in Cilia. Front Cell Dev Biol 5, 36.

Parra-Acero, H, Harcet, M, Sánchez-Pons, N, Casacuberta, E, Brown, NH, Dudin, O, and Ruiz-Trillo, I (2020). Integrin-Mediated Adhesion in the Unicellular Holozoan Capsaspora owczarzaki. Curr Biol 30, 4270-4275.e4.

Paweletz, N (2001). Walther Flemming: pioneer of mitosis research. Nat Rev Mol Cell Biol 2, 72–75.

Pentz, JT, Márquez-Zacarías, P, Bozdag, GO, Burnetti, A, Yunker, PJ, Libby, E, and Ratcliff, WC (2020). Ecological Advantages and Evolutionary Limitations of Aggregative Multicellular Development. Current Biology 30, 4155-4164.e6.

Pepling, ME, Cuevas, M de, and Spradling, AC (1999). Germline cysts: a conserved phase of germ cell development? Trends in Cell Biology 9, 257–262.

Perotti, O, Esparza, GV, and Booth, DS (2025). A red algal polysaccharide influences the multicellular development of the choanoflagellate Salpingoeca rosetta. Current Biology 35, 3767-3776.e4.

Piekny, AJ, and Glotzer, M (2008). Anillin is a scaffold protein that links RhoA, actin, and myosin during cytokinesis. Curr Biol 18, 30–36.

Pimentel, H, Bray, NL, Puente, S, Melsted, P, and Pachter, L (2017). Differential analysis of RNA-seq incorporating quantification uncertainty. Nat Methods 14, 687–690.

Price, KL, Tharakan, DM, Salvenmoser, W, Ayers, K, Mah, J, Dunn, C, Hobmayer, B, and Cooley, L (2025). Examination of Germline and Somatic Intercellular Bridges in Hydra vulgaris Reveals Insights into the Evolutionarily Conserved Mechanism of Intercellular Bridge Formation. Mol Biol Evol 42, msaf248.

Rabie, EM, Zhang, SX, Dunn, CE, and Nelson, CM (2021). Substratum stiffness signals through integrin-linked kinase and β1-integrin to regulate midbody proteins and abscission during EMT. Mol Biol Cell 32, 1664–1676.

Radler, MR, Liu, X, Peng, M, Doyle, B, Toyo-Oka, K, and Spiliotis, ET (2023). Pyramidal neuron morphogenesis requires a septin network that stabilizes filopodia and suppresses lamellipodia during neurite initiation. Curr Biol 33, 434-448.e8.

Ragkousi, K, and Gibson, MC (2014). Cell division and the maintenance of epithelial order. J Cell Biol 207, 181–188.

Ramus, J (1969). PIT CONNECTION FORMATION IN THE RED ALGA PSEUDOGLOIOPHLOEA. J Phycol 5, 57–63.

Ratcliff, WC, Fankhauser, JD, Rogers, DW, Greig, D, and Travisano, M (2015). Origins of multicellular evolvability in snowflake yeast. Nat Commun 6, 6102.

Reichhardt, C, Ferreira, JAG, Joubert, L-M, Clemons, KV, Stevens, DA, and Cegelski, L (2015). Analysis of the Aspergillus fumigatus Biofilm Extracellular Matrix by Solid-State Nuclear Magnetic Resonance Spectroscopy. Eukaryot Cell 14, 1064–1072.

Renshaw, MJ, Liu, J, Lavoie, BD, and Wilde, A (2014). Anillin-dependent organization of septin filaments promotes intercellular bridge elongation and Chmp4B targeting to the abscission site. Open Biol 4, 130190.

Richter, DJ, Berney, C, Strassert, JFH, Poh, Y-P, Herman, EK, Muñoz-Gómez, SA, Wideman, JG, Burki, F, and de Vargas, C (2022). EukProt: a database of genome-scale predicted proteins across the diversity of eukaryotes. Peer Community Journal 2, e56. https://doi.org/10.24072/pcjournal.173

Richter, DJ, Fozouni, P, Eisen, MB, and King, N (2018). Gene family innovation, conservation and loss on the animal stem lineage. Elife 7, e34226.

Rose, L, and Gönczy, P (2014). Polarity establishment, asymmetric division and segregation of fate determinants in early C. elegans embryos. WormBook, 1–43.

Ros-Rocher, N, Reyes-Rivera, J, Horo, U, Combredet, C, Foroughijabbari, Y, Larson, BT, Coyle, MC, Houtepen, EAT, Vermeij, MJA, Steenwyk, JL, *et al.* (2026). Clonal-aggregative multicellularity tuned by salinity in a choanoflagellate. Nature 651, 974–985.

Ross, MH, and Pawlina, W (2006). Histology: A Text and Atlas: With Correlated Cell and Molecular Biology, Baltimore, MD: Lippincott Williams & Wilkins.

Ruiz-Trillo, I, Roger, AJ, Burger, G, Gray, MW, and Lang, BF (2008). A Phylogenomic Investigation into the Origin of Metazoa. Mol Biol Evol 25, 664–672.

Sambandamoorthy, S, Mathew-Steiner, S, Varney, S, Zuidema, JM, Gilbert, RJ, Van De Water, L, and LaFlamme, SE (2015). Matrix compliance and the regulation of cytokinesis. Biol Open 4, 885–892.

Sayers, EW, Bolton, EE, Brister, JR, Canese, K, Chan, J, Comeau, DC, Farrell, CM, Feldgarden, M, Fine, AM, Funk, K, *et al.* (2023). Database resources of the National Center for Biotechnology Information in 2023. Nucleic Acids Res 51, D29–D38.

Schindelin, J, Arganda-Carreras, I, Frise, E, Kaynig, V, Longair, M, Pietzsch, T, Preibisch, S, Rueden, C, Saalfeld, S, Schmid, B, *et al.* (2012). Fiji: an open-source platform for biological-image analysis. Nat Methods 9, 676–682.

Sebé-Pedrós, A, Degnan, BM, and Ruiz-Trillo, I (2017). The origin of Metazoa: a unicellular perspective. Nat Rev Genet 18, 498–512.

Sebé-Pedrós, A, Irimia, M, del Campo, J, Parra-Acero, H, Russ, C, Nusbaum, C, Blencowe, BJ, and Ruiz-Trillo, I (2013). Regulated aggregative multicellularity in a close unicellular relative of metazoa. eLife 2, e01287.

Sebé-Pedrós, A, Roger, AJ, Lang, FB, King, N, and Ruiz-Trillo, I (2010). Ancient origin of the integrin-mediated adhesion and signaling machinery. Proc National Acad Sci 107, 10142–10147.

Shapiro, L, and Weis, WI (2009). Structure and Biochemistry of Cadherins and Catenins. Csh Perspect Biol 1, a003053.

Sharma, K, and Menon, MB (2023). Decoding post-translational modifications of mammalian septins. Cytoskeleton (Hoboken) 80, 169–181.

Shuman, B, and Momany, M (2022). Septins From Protists to People. Frontiers Cell Dev Biology 9, 824850.

Sirajuddin, M, Farkasovsky, M, Hauer, F, Kühlmann, D, Macara, IG, Weyand, M, Stark, H, and Wittinghofer, A (2007). Structural insight into filament formation by mammalian septins. Nature 449, 311–315.

Skelton, HM, Burkholder, JM, and Parrow, MW (2009). Axenic Culture of the Heterotrophic Dinoflagellate Pfiesteria shumwayae in a Semi-Defined Medium. Journal of Eukaryotic Microbiology 56, 73–82.

Soares, EV (2011). Flocculation in Saccharomyces cerevisiae: a review. J Appl Microbiol 110, 1–18.

Somerville, C, Bauer, S, Brininstool, G, Facette, M, Hamann, T, Milne, J, Osborne, E, Paredez, A, Persson, S, Raab, T, *et al.* (2004). Toward a systems approach to understanding plant cell walls. Science 306, 2206–2211.

Sorkin, J, Tilton, K, Lawlor, MA, Sarathy, SN, Liang, S, Albanese, A, Rabbani, M, Hammoud, SS, Ellison, CE, Pratto, F, *et al.* (2025). Intercellular bridges are essential for transposon repression and meiosis in the male germline. Nat Commun 16, 1488.

Spiliotis, ET, Hunt, SJ, Hu, Q, Kinoshita, M, and Nelson, WJ (2008). Epithelial polarity requires septin coupling of vesicle transport to polyglutamylated microtubules. J Cell Biology 180, 295–303.

Spiliotis, ET, and McMurray, MA (2020). Masters of asymmetry – lessons and perspectives from 50 years of septins. Mol Biol Cell 31, 2289–2297.

Steenwyk, JL, Loucks, JT, and Buida, TJ (2025). ClipKIT in the browser: fast online trimming of multiple sequence alignments for phylogenetics. Nucleic Acids Res 53, W169–W171.

Sturgess, W, Packirisamy, S, Geneidy, R, Nordenfelt, P, and Swaminathan, V (2024). ECM-dependent regulation of septin 7 in focal adhesions promotes mechanosensing and functional response in fibroblasts. iScience 27, 111355.

Surka, MC, Tsang, CW, and Trimble, WS (2002). The mammalian septin MSF localizes with microtubules and is required for completion of cytokinesis. Mol Biol Cell 13, 3532–3545.

Suzuki, K, Kawazu, T, Mita, T, Takahashi, H, Itoh, R, Toda, K, and Kuroiwa, T (1995). Cytokinesis by a contractile ring in the primitive red alga Cyanidium caldarium RK-1. Eur J Cell Biol 67, 170–178.

Szuba, A, Bano, F, Castro-Linares, G, Iv, F, Mavrakis, M, Richter, RP, Bertin, A, and Koenderink, GH (2021). Membrane binding controls ordered self-assembly of animal septins. eLife 10, e63349.

Taneja, N, Fenix, AM, Rathbun, L, Millis, BA, Tyska, MJ, Hehnly, H, and Burnette, DT (2016). Focal adhesions control cleavage furrow shape and spindle tilt during mitosis. Sci Rep 6, 29846.

Taubenberger, AV, Baum, B, and Matthews, HK (2020). The Mechanics of Mitotic Cell Rounding. Front Cell Dev Biol 8, 687.

Terauchi, M, Nagasato, C, and Motomura, T (2015). Plasmodesmata of brown algae. J Plant Res 128, 7–15.

Van Leeuwenhoek, A (1695). Arcana Naturae Detecta, Delft, the Netherlands: Apud Henricum a Krooneveld.

Varadi, M, Anyango, S, Deshpande, M, Nair, S, Natassia, C, Yordanova, G, Yuan, D, Stroe, O, Wood, G, Laydon, A, *et al.* (2022). AlphaFold Protein Structure Database: massively expanding the structural coverage of protein-sequence space with high-accuracy models. Nucleic Acids Res 50, D439–D444.

Waksman, G, Kumaran, S, and Lubman, O (2004). SH2 domains: role, structure and implications for molecular medicine. Expert Rev Mol Med 6, 1–18.

Walczak, CE, Cai, S, and Khodjakov, A (2010). Mechanisms of chromosome behaviour during mitosis. Nat Rev Mol Cell Biol 11, 91–102.

Wetzel, LA, Levin, TC, Hulett, RE, Chan, D, King, GA, Aldayafleh, R, Booth, DS, Sigg, MA, and King, N (2018). Predicted glycosyltransferases promote development and prevent spurious cell clumping in the choanoflagellate S. rosetta. Elife 7, e41482.

White, EA, and Glotzer, M (2012). Centralspindlin: at the heart of cytokinesis. Cytoskeleton (Hoboken) 69, 882–892.

Williams, SE, Beronja, S, Pasolli, HA, and Fuchs, E (2011). Asymmetric cell divisions promote Notch-dependent epidermal differentiation. Nature 470, 353–358.

Williams, SE, and Fuchs, E (2013). Oriented divisions, fate decisions. Current Opinion in Cell Biology 25, 749–758.

Wilson, EB (1925). The cell in development and heredity, New York: Macmillan.

Włoga, D, Strzyżewska-Jówko, I, Gaertig, J, and Jerka-Dziadosz, M (2008). Septins Stabilize Mitochondria in Tetrahymena thermophila. Eukaryot Cell 7, 1373–1386.

Wong, TKF, Ly-Trong, N, Ren, H, Baños, H, Roger, AJ, Susko, E, Bielow, C, Maio, ND, Goldman, N, Hahn, MW, *et al.* (2025). IQ-TREE 3: Phylogenomic Inference Software using Complex Evolutionary Models. EcoEvoRxiv. https://doi.org/10.32942/X2P62N.

Woznica, A, Cantley, AM, Beemelmanns, C, Freinkman, E, Clardy, J, and King, N (2016). Bacterial lipids activate, synergize, and inhibit a developmental switch in choanoflagellates. Proc National Acad Sci 113, 7894–7899.

Woznica, A, Gerdt, JP, Hulett, RE, Clardy, J, and King, N (2017). Mating in the Closest Living Relatives of Animals Is Induced by a Bacterial Chondroitinase. Cell 170, 1175-1183.e11.

Xu, J, Ericson, CF, Lien, Y-W, Rutaganira, FUN, Eisenstein, F, Feldmüller, M, King, N, and Pilhofer, M (2022). Identification and structure of an extracellular contractile injection system from the marine bacterium Algoriphagus machipongonensis. Nat Microbiol 7, 397–410.

Yamazaki, T, Owari, S, Ota, S, Sumiya, N, Yamamoto, M, Watanabe, K, Nagumo, T, Miyamura, S, and Kawano, S (2013). Localization and evolution of septins in algae. The Plant Journal 74, 605–614.

Yurchenco, PD (2011). Basement membranes: cell scaffoldings and signaling platforms. Cold Spring Harb Perspect Biol 3, a004911.